

# **CFD Analysis for Advanced Accumulator**

**Non-Proprietary Version**

**June 2013**

**© 2013 Mitsubishi Heavy Industries, Ltd.  
All Rights Reserved**

## **Revision History**

Revision	Page	Description
0	All	Original issued
1	-	<b>Remarks</b> All of calculations are updated by using Fluent Ver.12.0, where rev.0 of this technical report was reported by based on the calculation due to ver.6.3. Additional calculations are added to evaluate numerical uncertainty. Some sensitivity analyses are added to justify calculation method The followings items are revised in accordance with the revision of the proprietary scopes;
	iii	The title of Appendix-A is changed. Appendix B to K are added.
	iv	Table C-1 is added.
	v, vi	The figure of Appendix-A and Appendix B to K is changed and added, respectively.
	vii to ix	Many symbols and acronyms are added.
	2-1	The objective to evaluate CFD-evaluated Scale Effect is added.
	3-2	To use BPG (Best Practice Guideline) is described. The condition of tank water level is changed and the way is described for large flow
	3-3	The condition of tank water level is changed and the way is described for small flow. The title and content of Sec. 3.2.1(3) are changed.
	3-6	Description of Y+ and GCI regarding mesh is added.
	3-7,8	Mesh configuration shown in Figure 3.2-3 and 3.2-4 are revised.
	3-9	Version of Fluent is changed from 6.3.26 to 12.0. Time dependence is changed from Steady-State to Unsteady-State Calculation for small flow. Description of multiphase model is separated from one of Cavitation model. Description of note regarding RSM model is updated. Description of note regarding near-wall treatment is updated.
	3-10	Description regarding Singhal model is added to note 8.
	3-11	Total number of calculation points is increased. Description of calculation condition to obtain the GCI is added.
	3-12	Test cased for GCI is added.
	3-13	New calculation points are added in Figure 3.3-1.
	3-14	It is added that details of boundary conditions for small flow is described Appendix-D.

## **Revision History (Cont.)**

Revision	Page	Description
1	3-14	Description of note 1 is revised
	3-15	Description of note 2 is revised
	3-17, 18	Description of flow structure is revised
	3-19	Sec. 3.5.1(3) is added.
	3-20	Calculation results regarding flow structure shown in Figure 3.5-1 is updated.
	3-21 to 24	Figures 3.5-2 to 3.5-5 are added.
	3-25	Calculation results regarding the relationship between flow rate coefficient and cavitation factor shown in Figure 3.5-6 is updated.
	3-26	Description of flow structure is revised.
	3-34 to 38	Bias error and uncertainty of scale effect is introduced as CFD-evaluated Scale Effect.
	4-1	Result of CFD-evaluated Scale Effect is added.
	5-1	References from 1) to 3) are revised. References from 4) to 16) are added.
	A-1 to end of K	The title of Appendix-A is changed. Appendix-B to -K are added.
2	x	Description of acronyms are revised.
	1-1	Section 1.1 is added.
	2-1	Descriptions are revised.
	3-1 to 3	Descriptions are revised.
	3-4	Table 3.2-1 is added.
	3-6, 7 3-9 to 14	Descriptions are revised.
	3-15	Figure 3.3-1 is revised.
	3-16 to 18	Descriptions are revised.
	3-19 to 21	Description of 3.5 is revised.
	3-23	Figure 3.5-2 is revised.
	3-26	Figure 3.5-5 is revised.
	3-27	Figure 3.5-6 is revised.
	3-28	Table 3.5-1(a) and 3.5-1(b) are added.
	3-29, 30	Description of 3.5.2 is revised.
	3-35	Figure 3.5-9 is revised.
	3-36	Figure 3.5-10(a) and 3.5-10(b) are revised.
	3-36 to 40, 3-42	Description of 3.5.3 is revised.
	4-1	Description of 4.0 is revised.
	5-1, 2	References 3) and 9) are revised. References from 17) to 19) are added.

## Revision History (Cont.)

Revision	Page	Description
2	A-1	Description of Appendix-A is revised.
	-	Figure B1-1 of MUAP-09025-P (R1) is deleted.
	B-1 to B-18	Appendix-B is revised.
	B-11	Figure B3-3 is revised.
	B-13	Table B3-5 and B3-6 are added.
	B-14	Description of B-3(3) is revised. Explanation of additional 3 GCI calculations are added.
	B-14	Table B3-7 is added.
	B-15, 16	Figure B3-5 and B3-6 are added.
	B-17	Table B3-8 is added.
	B-18	Description of B-4 is revised.
	-	Figure C-1 to C-3 of MUAP-09025-P (R1) is deleted.
	C-4 to 6	Description of Appendix-C is revised.
	C-8	Figure C-2 is added.
	C-9, 11, 12	Description of Appendix-C is revised.
	D-1	Table D-1 is revised.
	E-1	Description of Appendix-E is added.
	E-10	Figure E-5(b) is revised.
	F-1	Description of Appendix-F is added.
	F-12 to F-15	Figure F-6(a) to (d) are added
	F-16, 17	Figure F-7(a) and (b) are added
	H-1	Description of Appendix-H is revised.
	I-1 to 10	Appendix-I is revised add an evaluation of the impact of cavitation occurrence on flow coefficient..
	-	Appendix-J of MUAP-09025-P (R1) is deleted.
3	-	<p><b>Remarks</b></p> <p>An evaluation for numerical uncertainty is conservatively revised and its supporting information is provided in appendix-A, K and L. The following section and appendices are revised or newly added in accordance with the revision of the proprietary scopes;</p> <p>Section 3.5.3 is revised to provide the properly conservative numerical uncertainties. Appendix-A is revised to provide the supporting information used in Section 3.5.3. Appendix-K is added to provide more detailed supporting information for the discussion in Appendix-A. Appendix-M is added also to provide more detailed supporting information for the discussion in Appendix-A. Appendix-L is added for further comparison of the numerical uncertainty evaluation.</p>

## **Revision History (Cont.)**

Revision	Page	Description
3	i	Year is revised.
	iii	Appendix-K is added.
	iii	Appendix-L is added.
	iii	Appendix-M is added.
	iv	Notation of tables in Appendix-A is revised.
	iv	Table A5-1, A6-1 are added.
	v	Table K1-1, K2-1, K2-2, K3-1 to K3-3 are added.
	v	Table L-1 to L-3 are added.
	v, vi	Table M-1 to M-8 are added.
	vii, viii	Notation of figures in Appendix-A is revised.
	vii	Figure A2-1 is added.
	vii	Figure A2-5 is added.
	viii	Figure A3-1, A3-2, A5-1 to A5-5 are added.
	x	Figure K1-1, K1-2, K3-1 to K3-4 are added.
	xi to xiii	Description of acronyms are revised.
	1-3	Description is revised.
	3-2	Description is revised.
	3-7	Description is revised.
	3-40	Description is revised.
	3-41	Table 3.5-3 and Table 3.5-4 are revised.
	3-42	Description is revised.
	5-1	References are updated.
	5-2	Reference 20) and 21) are added.
	A-1 and A-3 to A-24	Description of Appendix-A is revised.
	A-5	Figure A2-1 is added.
	A-6, A-7	Notations of Figure A2-2 to A2-4 are revised.
	A-8	Figure A2-5 is added.
	A-10, A-11	Notations of Table A3-1 to A3-4 are revised.
	A-12, A-13	Notations of Figure A3-1 and A3-2 are revised.
	A-16, A-17 A-19 to A-21	Figure A5-1 to A5-5 are added.
	A-18	Table A5-1 is added.
	A-23	Table A6-1 is added.
	K-1 to K-8	Appendix-K is added.
	L-1 to L-3	Appendix-L is added.
	M-1 to M-17	Appendix-M is added.

© 2013  
**mitsubishi Heavy Industries, LTD.**  
All Rights Reserved

This document has been prepared by Mitsubishi Heavy Industries, Ltd. ("MHI") in connection with the U.S. Nuclear Regulatory Commission's ("NRC") licensing review of MHI's US-APWR nuclear power plant design. No right to disclose, use or copy any of the information in this document, other than by the NRC and its contractors in support of the licensing review of the US-APWR, is authorized without the express written permission of MHI.

This document contains technology information and intellectual property relating to the US-APWR and it is delivered to the NRC on the express condition that it not be disclosed, copied or reproduced in whole or in part, or used for the benefit of anyone other than MHI without the express written permission of MHI, except as set forth in the previous paragraph.

This document is protected by the laws of Japan, U.S. copyright law, international treaties and conventions, and the applicable laws of any country where it is being used.

Mitsubishi Heavy Industries, Ltd.  
16-5, Konan 2-chome, Minato-ku  
Tokyo 108-8215 Japan

## **Abstract**

The Advanced Accumulator (ACC) developed by MHI functions to switch flow rates automatically from a large flow rate to small flow rate as a requirement for the Loss of Coolant Accident (LOCA) event. This function is achieved by the flow damper inside the accumulator tank. For the purpose of understanding the flow characteristics and verifying the performance of the ACC, the “Full-Height 1/2 Scale Confirmation Test”, which uses the full height of the test tank and the standpipe, has been conducted (Ref.1). For flow with large Reynolds numbers, minimal influence from viscous effects is anticipated. Therefore, the 1/1 scale ACC prototype with even larger Reynolds numbers, will also have similar hydraulic performance as the 1/2 scale model. MHI proposes to apply the measured 1/2 scale hydraulic performance to the 1/1 scale ACC.

However, since there is little detailed information measured in the vortex chamber of the flow damper and near the throat section in existing experiments, there may not be enough evidence to validate extrapolation to the 1/1 scale. To provide an adequate explanation, sufficient understanding about the flow dynamics of the ACC is important, especially for flow inside the vortex chamber and the connecting piping (such as the throat, diffuser and injection piping), which may include cavitation phenomena.

Regarding the background mentioned above, a Computational Fluid Dynamics (CFD) analysis was applied to better understand the flow structure and the cavitation phenomena in the ACC, and to investigate the validity of extrapolating from 1/2 to 1/1 scale flow dampers.

In this investigation, CFD analyses with cavitation modeling options were conducted by using a 1/2 scale model and a 1/1 scale analytical model to show the similarity between the flow structure and flow characteristic performance (i.e., the flow rate coefficient) for the 1/2 and 1/1 scale sizes.

Below is the summary and conclusions about this report regarding the CFD analysis.

- The CFD prediction is feasible for large and small characteristic evaluations. In the 1/2 scale model analysis, the correlation between the flow rate coefficient ( $C_v$ ) and the cavitation factor ( $\sigma_v$ ) reasonably matched the measured data.
- The validity of the current evaluation approach (Refs.1 and 2) for the ACC performance (i.e., the extrapolation from scale model experiment and the characteristic equations) is supported by the scale effect obtained from the CFD models. The CFD-Evaluated Scale Effect between the calculated data in the 1/2 scale model and the 1/1 scale model was shown to consist mainly of CFD uncertainty. The CFD-Evaluated Scale Effect can be accounted for in the evaluation of the 1/1 scale ACC hydraulic performance (Refs. 1 and 2).

## **Table of Contents**

List of Tables .....	iv
List of Figures .....	vii
List of Acronyms and Symbols .....	xi
 1.0 INTRODUCTION .....	 1-1
1.1 Report Outline .....	1-1
2.0 OBJECTIVE .....	2-1
2.1 Background .....	2-1
2.2 Objective .....	2-1
3.0 CFD ANALYSIS .....	3-1
3.1 System Descriptions .....	3-1
3.2 Analysis Models .....	3-2
3.3 Test Case for Analysis .....	3-13
3.4 Boundary Conditions .....	3-16
3.5 Analysis Results .....	3-19
4.0 CONCLUSIONS .....	4-1
5.0 REFERENCES .....	5-1
 Appendix-A    Calculation of GCI .....	 A-1
Appendix-B    Scale-up Capability of Turbulence Model .....	B-1
Appendix-C    Selection of Cavitation Model .....	C-1
Appendix-D    Consideration for Boundary Condition in Small Flow Injection .....	D-1
Appendix-E    Flow structure for Large Flow .....	E-1
Appendix-F    Flow structure for Small Flow .....	F-1
Appendix-G    Y+ Profile .....	G-1
Appendix-H    Validity Evaluation of Tolerance Interval .....	H-1
Appendix-I    Effect of Cavitation on Small Flow Hydraulic Performance .....	I-1
Appendix-J    Details of Comparison Error for Large Flow .....	J-1
Appendix-K    Asymptotic Behavior of Solution Results .....	K-1
Appendix-L    More Conservative CFD-evaluated Scale Effect .....	L-1
Appendix-M    Mesh Refinement Ratio for Each Different Direction .....	M-1



## **List of Tables**

Table 3.2-1	Comparison of Main Dimensions.....	3-4
Table 3.3-1	Test Cases and Time Points for Calculation .....	3-14
Table 3.3-2	Test Cases for GCI Calculation .....	3-14
Table 3.4-1	Boundary Condition Data for Calculation .....	3-18
Table 3.5-1(a)	Characteristic Equation and Calculation Results for Flow Rate Coefficient (Large Flow) .....	3-28
Table 3.5-1(b)	Characteristic Equation and Calculation Results for Flow Rate Coefficient (Small Flow) .....	3-28
Table 3.5-2	Factors for Calculating the Two-Sided 95% Probability Intervals for A Normal Distribution (Ref. 16)) .....	3-39
Table 3.5-3	Uncertainties in ACC Flow Model (Large Flow).....	3-41
Table 3.5-4	Uncertainties in ACC Flow Model (Small Flow).....	3-41
Table A3-1	Calculation Procedure of GCI for 1/2 Scale Model CFD ( $\phi$ = Flow Rate Coefficient Cv) .....	A-10
Table A3-2	Calculation Procedure of GCI for 1/1 Scale Model CFD ( $\phi$ = Flow Rate Coefficient Cv) .....	A-10
Table A3-3	Calculation Procedure of GCI for 1/2 Scale Model CFD ( $\phi$ = Tank Inlet Pressure Pg) .....	A-11
Table A3-4	Calculation Procedure of GCI for 1/1 Scale Model CFD ( $\phi$ = Tank Inlet Pressure Pg) .....	A-11
Table A5-1	Re-Evaluated Observed p-values Using the Additional Solution.....	A-18
Table A6-1	Re-Evaluated GCIs by Modified Methodology Using p=1.5 and Fs=3.0 ...	A-23
Table B2-1	Examples of Tuning the $\epsilon$ Equation .....	B-4
Table B3-1	Calculation Condition and Calculation Results Before and After Tuning for 1/2 Scale Model Calculation .....	B-9
Table B3-2	Effect of Tuning on Mean Cv Comparison Error (Small Flow) .....	B-10
Table B3-3	Comparison of Flow Structure by Tuning for Small Flow Injection .....	B-11
Table B3-4	Calculation Condition and Calculation Results Before and After Tuning for Scale Effect .....	B-12
Table B3-5	Calculation Conditions of Tuned CFD .....	B-13
Table B3-6	Calculation Results of Tuned CFD .....	B-13
Table B3-7	GCI Change Due to Tuning of Turbulence Model .....	B-14

Table B3-8	Calculation Procedure of GCI ( $\phi$ = Flow Rate Coefficient Cv).....	B-17
Table C-1	Capabilities and Limitations of Three Cavitation Models in FLUENT 12.0.....	C-3
Table C-2	Calculation Conditions for Singhal and ZGB Models.....	C-6
Table C-3	Scale Effects in Singhal and ZGB Models for Large Flow.....	C-6
Table D-1	Calculation Conditions of CFD .....	D-1
Table D-2	Calculation Results of CFD .....	D-1
Table H-1	Factors for Calculating the Two-Sided 90% and 95% Probability Intervals for a Normal Distribution (Ref.15)) .....	H-1
Table I-1	CFD Boundary Conditions for Sensitivity Analysis Regarding Cavitation Occurrence .....	I-2
Table I-2	Calculation Results (1/2 Scale) .....	I-9
Table I-3	Calculation Results (1/1 Scale) .....	I-9
Table K1-1	Corrected C(ratio) ( $p_{\text{assumed}} = 1.5$ ) .....	K-3
Table K2-1	The Solution value and Relative errors .....	K-4
Table K2-2	Calculations of C(ratio) .....	K-4
Table K3-1	Corrected C(ratio) ( $p_{\text{assumed}} = 1.5$ ) .....	K-6
Table K3-2	Corrected C(ratio) ( $p_{\text{assumed}} = 1.0$ ) .....	K-8
Table K3-3	Corrected C(ratio) ( $p_{\text{assumed}} = 2.58$ ) .....	K-8
Table L-1	Bounding GCIs for Further Comparison ( $p=1$ and $Fs=3.0$ ).....	L-2
Table L-2	Uncertainties using Bounding GCIs (Large Flow) .....	L-3
Table L-3	Uncertainties using Bounding GCIs (Small Flow).....	L-3
Table M-1	(a) Mesh Refinement Ratio for Each Different Direction (Large Flow, CASE03-005sec, 1/1 Scale ACC) .....	M-2
Table M-1	(b) Mesh Refinement Ratio for Each Different Direction (Large Flow, CASE03-005sec, 1/2 Scale ACC) .....	M-3
Table M-2	(a) Mesh Refinement Ratio for Each Different Direction (Large Flow, CASE03-034sec, 1/1 Scale ACC) .....	M-4
Table M-2	(b) Mesh Refinement Ratio for Each Different Direction (Large Flow, CASE03-034sec, 1/2 Scale ACC) .....	M-5
Table M-3	(a) Mesh Refinement Ratio for Each Different Direction (Large Flow, CASE06-005sec, 1/1 Scale ACC) .....	M-6
Table M-3	(b) Mesh Refinement Ratio for Each Different Direction	

	(Large Flow, CASE06-005sec, 1/2 Scale ACC) .....	M-7
Table M-4	(a) Mesh Refinement Ratio for Each Different Direction	
	(Large Flow, CASE06-050sec, 1/1 Scale ACC) .....	M-8
Table M-4	(b) Mesh Refinement Ratio for Each Different Direction	
	(Large Flow, CASE06-050sec, 1/2 Scale ACC) .....	M-9
Table M-5	(a) Mesh Refinement Ratio for Each Different Direction	
	(Small Flow, CASE03-043sec, 1/1 Scale ACC) .....	M-10
Table M-5	(b) Mesh Refinement Ratio for Each Different Direction	
	(Small Flow, CASE03-043sec, 1/2 Scale ACC) .....	M-11
Table M-6	(a) Mesh Refinement Ratio for Each Different Direction	
	(Small Flow, CASE03-125sec, 1/1 Scale ACC) .....	M-12
Table M-6	(b) Mesh Refinement Ratio for Each Different Direction	
	(Small Flow, CASE03-125sec, 1/2 Scale ACC) .....	M-13
Table M-7	(a) Mesh Refinement Ratio for Each Different Direction	
	(Small Flow, CASE06-082sec, 1/1 Scale ACC) .....	M-14
Table M-7	(b) Mesh Refinement Ratio for Each Different Direction	
	(Small Flow, CASE06-082sec, 1/2 Scale ACC) .....	M-15
Table M-8	(a) Mesh Refinement Ratio for Each Different Direction	
	(Small Flow, CASE06-290sec, 1/1 Scale ACC) .....	M-16
Table M-8	(b) Mesh Refinement Ratio for Each Different Direction	
	(Small Flow, CASE06-290sec, 1/2 Scale ACC) .....	M-17

## **List of Figures**

Figure 3.2-1	Analysis Models for 1/1 Scale .....	3-5
Figure 3.2-2	Analysis Models for 1/2 Scale .....	3-6
Figure 3.2-3	Mesh Configurations of Vortex Chamber for 1/2 and 1/1 Scale Model for Large Flow .....	3-9
Figure 3.2-4	Mesh Configurations of Vortex Chamber for 1/2 and 1/1 Scale Model for Small Flow .....	3-10
Figure 3.3-1	Calculation Points on Flow Characteristics of Flow Damper .....	3-15
Figure 3.5-1(a)	Flow Structure in Vortex Chamber (Large Flow).....	3-22
Figure 3.5-1(b)	Flow Structure in Vortex Chamber (Small Flow).....	3-22
Figure 3.5-2	General Flow Structure .....	3-23
Figure 3.5-3	Static Pressure Distribution (Small Flow, Fine Mesh, Case 3, 43 sec).....	3-24
Figure 3.5-4	Void Fraction Distribution (Small Flow, Fine Mesh, Case 3, 43 sec).....	3-25
Figure 3.5-5	Reverse Flow Confirmation.....	3-26
Figure 3.5-6(a)	Comparison between Test Results and Calculation Results for Flow Rate Coefficient in Large Flow Condition .....	3-27
Figure 3.5-6(b)	Comparison between Test Results and Calculation Results for Flow Rate Coefficient in Small Flow Condition .....	3-27
Figure 3.5-7(a)	Flow Structure in Vortex Chamber (Case 3 Large Flow 5 sec).....	3-31
Figure 3.5-7(b)	Flow Structure in Outlet Nozzle (Case 3 Large Flow 5 sec) .....	3-32
Figure 3.5-8(a)	Flow Structure in Vortex Chamber (Case 3 Small Flow 43 sec).....	3-33
Figure 3.5-8(b)	Flow Structure in Outlet Nozzle (Case 3 Small Flow 43 sec) .....	3-34
Figure 3.5-9	Comparison between 1/2 and 1/1 Scale of CFD Result .....	3-35
Figure 3.5-10(a)	Relationship between Flow Rate Coefficient and Scale (Large Flow).....	3-36
Figure 3.5-10(b)	Relationship between Flow Rate Coefficient and Scale (Small Flow) .....	3-36
Figure A2-1	Schematic of Division for ACC CFD Meshing .....	A-5
Figure A2-2	CFD Mesh Configurations (Fine Mesh) .....	A-6
Figure A2-3	CFD Mesh Configurations (Normal Mesh) .....	A-6
Figure A2-4	CFD Mesh Configurations (Coarse Mesh).....	A-7
Figure A2-5	Grid Convergence Trend (Large Flow, Case03-05sec) .....	A-8

Figure A3-1	Representative Grid Convergence Trend Curve for Cv (Flow Rate Coefficient) and Pg (Tank Pressure) with 1/2 Scale Model .....	A-12
Figure A3-2	Representative Grid Convergence Trend Curve for Cv (Flow Rate Coefficient) and Pg (Tank Pressure) with 1/1 Scale Model .....	A-13
Figure A5-1	Re-evaluated ACC CFD Cases (bold face) .....	A-16
Figure A5-2	Confirmation of Grid Convergence with Additional Intermediate Mesh .....	A-17
Figure A5-3	Grid Convergence Trend for Large Flow (Re-Evaluated) for Large Observed p-value Cases .....	A-19
Figure A5-4	Grid Convergence Trend for Small Flow (Re-Evaluated) for Approximately Grid Converged p-value Cases .....	A-20
Figure A5-5	Grid Convergence Trend for Small Flow (Re-Evaluated) for Large Observed p-value Case .....	A-21
Figure B2-1	Axial Velocity Distribution of the Swirling Flow in the Rotating Pipe around the Pipe Axis .....	B-5
Figure B3-1	Test Results and Calculation Results for Flow Rate Coefficient (Large Flow Condition) .....	B-7
Figure B3-2	Test Results and Calculation Results for Flow Rate Coefficient (Small Flow Condition) .....	B-7
Figure B3-3	Effect of Tuning to Cv- $\sigma_v$ Map (Small Flow Condition) .....	B-11
Figure B3-4	Scale Effect for Cv by Tuning .....	B-12
Figure B3-5	Grid Convergence Trend Curve for "Cv" for case3-43 sec .....	B-15
Figure B3-6	Grid Convergence Trend Curve for "Cv" for case6-82 sec .....	B-16
Figure C-1	Void Fraction Distribution at the Throat (Case 3 Large Flow 5 sec, Fine Mesh) .....	C-7
Figure C-2	Total Pressure Loss of Vortex Chamber, Reducer and Diffuser .....	C-8
Figure D-1	Comparison of Inlet Boundary Conditions for Small Flow Injection (a) Void Fraction, (b) Velocity Contour, (c) Static Pressure .....	D-2
Figure E-1(a)	Flow Structure in Vortex Chamber (Case 3 Large Flow 20 sec) .....	E-2
Figure E-1(b)	Flow Structure in Flow Damper (Case 3 Large Flow 20 sec) .....	E-3
Figure E-2(a)	Flow Structure in Vortex Chamber (Case 3 Large Flow 34 sec) .....	E-4
Figure E-2(b)	Flow Structure in Flow Damper (Case 3 Large Flow 34 sec) .....	E-5
Figure E-3(a)	Flow Structure in Vortex Chamber (Case 6 Large Flow 5 sec) .....	E-6
Figure E-3(b)	Flow Structure in Flow Damper (Case 6 Large Flow 5 sec) .....	E-7
Figure E-4(a)	Flow Structure in Vortex Chamber (Case 6 Large Flow 11 sec) .....	E-8

Figure E-4(b)	Flow Structure in Flow Damper (Case 6 Large Flow 11 sec) .....	E-9
Figure E-5(a)	Flow Structure in Vortex Chamber (Case 6 Large Flow 20 sec).....	E-10
Figure E-5(b)	Flow Structure in Flow Damper (Case 6 Large Flow 20 sec) .....	E-11
Figure E-6(a)	Flow Structure in Vortex Chamber (Case 6 Large Flow 50 sec).....	E-12
Figure E-6(b)	Flow Structure in Flow Damper (Case 6 Large Flow 50 sec) .....	E-13
Figure F-1(a)	Flow Structure in Vortex Chamber (Case 3 Small Flow 100 sec).....	F-2
Figure F-1(b)	Flow Structure in Flow Damper (Case 3 Small Flow 100 sec).....	F-3
Figure F-2(a)	Flow Structure in Vortex Chamber (Case 3 Small Flow 125 sec).....	F-4
Figure F-2(b)	Flow Structure in Flow Damper (Case 3 Small Flow 125 sec).....	F-5
Figure F-3(a)	Flow Structure in Vortex Chamber (Case 6 Small Flow 82 sec).....	F-6
Figure F-3(b)	Flow Structure in Flow Damper (Case 6 Small Flow 82 sec).....	F-7
Figure F-4(a)	Flow Structure in Vortex Chamber (Case 6 Small Flow 200 sec).....	F-8
Figure F-4(b)	Flow Structure in Flow Damper (Case 6 Small Flow 200 sec).....	F-9
Figure F-5(a)	Flow Structure in Vortex Chamber (Case 6 Small Flow 290 sec).....	F-10
Figure F-5(b)	Flow Structure in Flow Damper (Case 6 Small Flow 290 sec).....	F-11
Figure F-6(a)	Reverse Flow Region (1/2 Scale, Case 3 Small Flow) .....	F-12
Figure F-6(b)	Reverse Flow Region (1/2 Scale, Case 6 Small Flow) .....	F-13
Figure F-6(c)	Reverse Flow Region (1/1 Scale, Case 3 Small Flow) .....	F-14
Figure F-6(d)	Reverse Flow Region (1/1 Scale, Case 6 Small Flow) .....	F-15
Figure F-7(a)	Location of Max. value of Deference between Absolute Pressure and Critical Pressure of Cavitation (1/2 scale, Small Flow) .....	F-16
Figure F-7(b)	Location of Max. value of Deference between Absolute Pressure and Critical Pressure of Cavitation (1/1 scale, Small Flow) .....	F-17
Figure G-1	Y+ Distribution of Large Flow.....	G-1
Figure G-2	Y+ Distribution of Small Flow .....	G-2
Figure G-3	Shear Stress Distribution of Small Flow.....	G-2
Figure I-1(a)	Flow Structure in Vortex Chamber (at mid-height) .....	I-4
Figure I-1(b)	Flow Structure in Vortex Chamber and Outlet Nozzle .....	I-5
Figure I-1(c)	Critical Pressure of Cavitation and Void Fraction in vortex Chamber and Outlet Nozzle .....	I-6
Figure I-2	Velocity Distributions and Cavitation Pressure Margin at Throat .....	I-7
Figure I-3	Relative Average Total Pressure of Forward Flow Area .....	I-8
Figure J-1	Overlapping between Test Results and Calculation Results for Flow Rate Coefficient (Large Flow Condition) .....	J-2

---

Figure K1-1	C(ratio) <sub>r=const</sub> vs. R(ratio) .....	K-2
Figure K1-2	Calculation Results for C(ratio) <sub>r=const</sub> vs. R(ratio) .....	K-3
Figure K3-1	C(ratio) <sub>r=const</sub> vs. R(ratio) .....	K-5
Figure K3-2	Calculation Results for C(ratio) <sub>r=const</sub> vs. R(ratio) ( $p_{\text{assumed}} = 1.5$ ).....	K-7
Figure K3-3	Calculation Results for C(ratio) <sub>r=const</sub> vs. R(ratio) ( $p_{\text{assumed}} = 1.0$ ).....	K-8
Figure K3-4	Calculation Results for C(ratio) <sub>r=const</sub> vs. R(ratio) ( $p_{\text{assumed}} = 2.58$ ).....	K-8

---

## List of Acronyms and Symbols

ACC	Advanced Accumulator
APWR	Advanced Pressurized-Water Reactor
BPG	Best Practice Guideline: Ref.5)
CFD	Computational Fluid Dynamics
$C_{T,95}(n)$	Factors for tolerance interval to contain at Least 95% of the population
COL	Combined License
$C_v$	Flow rate coefficient, (-)
$C_{v_{1/1},i}$	Flow rate coefficient in case i obtained by CFD for 1/1 scale ACC
$C_{v_{1/2},i}$	Flow rate coefficient in case i obtained by CFD for 1/2 scale ACC
$e_a^{21}$	Approximate relative error, (-)
$e_{ext}^{21}$	Extrapolated relative error, (-)
ECCS	Emergency Core Cooling System
$e_m$	Manufacturing error as relative standard deviation
$f_v$	Vapor mass fraction, (-)
$f_g$	Non-condensable gas mass fraction, (-)
Fs	Factor of safety, (-)
$F_{cond\_SH}$	Vapor condensation coefficient in Singhal model, = 0.01 (m/s)
$F_{vap\_SH}$	Vapor generation coefficient in Singhal model, = 0.02 (m/s)
$F_{cond\_ZGB}$	Vapor condensation coefficient in Zwart-Gerber-Belamri model, = 0.01(-)
$F_{vap\_ZGB}$	Vapor generation coefficient in Zwart-Gerber-Belamri model, = 50 (-)
g	Gravitational acceleration, (m/s <sup>2</sup> )
GCI	Grid Convergence Index, (-)
$GCI_{fine}^{21}$	Grid Convergence Index for fine mesh model, (-)
$h$	Representative cell size, (m)
$h_{coarse}$	Representative cell size of coarse mesh model, (m)
$h_{fine}$	Representative cell size of fine mesh model, (m)
$h_i$	Representative cell size of <i>i</i> -th number mesh model, (m)
LOCA	Loss of Coolant Accident
MHI	Mitsubishi Heavy Industries, Ltd
M.V.	Mean value of differences between 1/2 and 1/1 scale CFD
$n_B$	Number of bubbles per unit volume, (1/m <sup>3</sup> )



$N$	Total number of cells used for the computation, (-)
$N_{\text{coarse}}$	Total number of cells of coarse mesh model used for the computation, (-)
$N_{\text{fine}}$	Total number of cells of fine mesh model used for the computation, (-)
$\rho$	Observed order of accuracy, (-)
$P$	Local far-field pressure, (Pa)
$P_B$	Vapor bubble surface pressure, (Pa)
$P_g$	Tank pressure, (Pa)
$P_{\text{sat}}$	Vapor saturation pressure, (Pa)
$P_V$	Critical pressure of cavitation, (Pa)
$r$	Grid refinement ratio, (-)
$r_{\text{effective}}$	Effective grid refinement ratio for unstructured mesh, (-)
$r_{21}$	Grid refinement ratio from 2 <sup>nd</sup> mesh model to 1 <sup>st</sup> mesh model, (-)
$r_{32}$	Grid refinement ratio from 3 <sup>rd</sup> mesh model to 2 <sup>nd</sup> mesh model, (-)
$R$	Vapor mass source term, (kg/(m <sup>3</sup> .s))
RANS	Reynolds-averaged Navier-Stokes
$R_B$	Vapor bubble radius, (m)
$R_{B\_ZGB}$	Vapor bubble radius in Zwart-Gerber-Belamri model, = 10 <sup>-6</sup> (m)
$R_c$	Mass transfer sink term due to vapor bubble collapse during the cavitation process, (kg/(m <sup>3</sup> .s))
$R_e$	Mass transfer source term due to vapor bubble growth during the cavitation process, (kg/(m <sup>3</sup> .s))
RCS	Reactor Coolant System
RSM	Reynolds Stress Model
$s$	Indicator of Oscillatory Convergence
S.D	Standard deviation of differences between 1/2 and 1/1scale CFD
$u_{\text{scale}}$	Standard uncertainty of the scale effect bias estimated from CFD results
$u_{SD}$	Standard uncertainty due to deviation from bias
$u_{\text{mesh}}$	Standard uncertainty due to spatial discretization approximation for CFD calculations
US	United States of America
$V_{\text{rel}}$	Relative velocity between vapor bubble and liquid, (m/s)
$V_v$	Vapor velocity, (m/s)
We	Weber number, (-)

### Greek Letters

$\alpha$	Vapor volume fraction, (-)
$\alpha_{nuc}$	Vapor bubble nucleation site volume fraction in Zwart-Gerber-Belamri model, = $5 \times 10^{-4}$ (-)
$\Gamma$	Diffusion coefficient, (kg/(m.s))
$\kappa$	Turbulent kinetic energy, ( $m^2/s^2$ )
$\rho$	Mixture density, ( $kg/m^3$ )
$\rho_l$	Liquid density, ( $kg/m^3$ )
$\rho_v$	Vapor density, ( $kg/m^3$ )
$\Delta\rho$	Density difference between liquid and vapor, ( $kg/m^3$ )
$\Delta V_i$	Volume of $i$ -th number cell used for the computation, ( $m^3$ )
$\delta C_{v_{scale}}$	Scaling effects (bias) estimated from CFD results
$\sigma$	Surface tension, (N/m) or Standard deviation
$\sigma_v$	Cavitation Factor
$\phi$	Key variable important to the objective of the simulation study for GCI
$\phi_k$	Solution on the $k^{th}$ mesh model

## 1.0 INTRODUCTION

This report describes the Computational Fluid Dynamics (CFD) analysis results for the Advanced Accumulator (ACC) performed by Mitsubishi Heavy Industries, Ltd. (MHI). The purpose of this document is to show that the same ACC flow phenomena would occur in the test facility and the 1/1 scale prototype in the plant. Review of this Technical Report should facilitate review of the US-APWR Design Certification process and any subsequent Combined License (COL) which references the US-APWR Design.

The ACC is an accumulator tank with a flow damper that is partially filled with borated water and is pressurized with nitrogen. It is attached to the primary system with a series of check valves and an isolation valve and is aligned during operation to allow flow into the primary coolant system if pressure in the primary system drops below the pressure of the accumulator. The ACC design combines the known advantages and extensive operating experience of a conventional accumulator used for Loss of Coolant Accident (LOCA) mitigation in pressurized water reactors with the inherent reliability of a passive fluidic device to achieve a desired injection flow profile of reactor coolant without the need of any moving parts. Incorporation of the ACC into the US-APWR design and LOCA mitigation strategy simplifies a critically important safety system by integrating an inherently reliable passive safety component into the conventional Emergency Core Cooling System (ECCS). This design improvement will allow the elimination of low head safety injection pumps, and increase the amount of time available for the installed backup emergency power system to actuate. It is expected that the use of ACCs rather than low head safety injection pumps in the US-APWR design will reduce the net maintenance and testing workload at nuclear facilities while maintaining a very high level of safety.

Topical Report "The Advanced Accumulator", MUAP-07001 Revision 5 (Ref.1)), has been submitted to describe the principles of operation of the ACC, the important design features, and the extensive analysis and confirmatory testing program conducted. This Technical Report describes CFD analysis results to support discussion of scalability in the Topical Report.

### 1.1 Report Outline

This section provides an overview of the content and conclusions of the major sections in this report. Sections 1.0 and 2.0 provide an introduction and background to the ACC and outline the main objectives for the present CFD study. Section 3.0 describes the CFD analysis in detail. Section 4.0 provides the final results and conclusions of the CFD study, and Section 5.0 lists supporting references. The appendices contain detailed results supporting calculations and sensitivity analyses.

Details of the CFD analysis are contained in Section 3.0, which includes the following subsections:

- Section 3.1 provides a brief description of ACC operation and its safety function in the US-APWR plant.
- Section 3.2 describes the CFD model configuration including the ACC geometry modeled, the mesh configuration, and the chosen physical models and settings for the CFD analysis.

- Section 3.3 lists the test conditions chosen from the scaled testing described in Reference 1 which were chosen for further CFD analysis
- Section 3.4 outlines the boundary conditions for the CFD analysis and describes how these boundary conditions were derived from measurements taken during the scaled testing (Ref. 1).
- Section 3.5 provides the results of the CFD analysis and consists of the following three subsections:
  - Section 3.5.1, with the support of the appendices subsequently discussed, verifies that the results are appropriate for quantifying a scaling effect. The general flow structures and flow coefficient behavior are similar between scales and consistent with the test observations and theoretical expectations described in Reference 1. Comparison to the measured test data and additional sensitivity analyses show that the CFD model configuration is sufficient for quantifying the scaling effect.
  - Section 3.5.2 provides the CFD results with explanations and comparisons to the measured test data.
  - Section 3.5.3 describes the methodology for evaluating the scale effect from the CFD results, including estimating the numerical and statistical uncertainty, to quantify a final CFD-Evaluated Scale Effect.

The appendices to this report provide additional supporting information for the ACC CFD analyses. The appendices listed below contain sensitivity analyses and/or alternate calculations to justify and validate the results of the CFD analyses in Section 3.0:

- Appendix-B discusses the physical model for turbulence utilized in the analyses to evaluate the impact of modeling error in the CFD results for small flow, compared to the observed test values. The appendix performs additional CFD analyses with a modified version of the turbulence model and concludes that the CFD-Evaluated Scale Effect calculated using the generalized turbulent model is bounding.
- Appendix-C discusses the physical model for cavitation utilized in the analyses and includes sensitivity analyses using alternate cavitation models. The appendix concludes that alternate cavitation models do not significantly impact the CFD flow coefficients.
- Appendix-D performs sensitivity analyses for the small flow boundary conditions, and concludes that the type of boundary conditions employed do not significantly impact the CFD flow coefficients.
- Appendix-I analyzes the impact of potential cavitation during small flow. The appendix performs modified and bounding outlet pressure analyses to induce cavitation during small flow and demonstrates that cavitation occurrence does not impede flow or significantly affect the ACC flow coefficient.

The following appendices provide additional detailed results for the CFD analyses described in Section 3.0:

- Appendix-A provides details for the methodology and results for calculating the GCI to quantify the numerical uncertainty from the CFD results.
- Appendix-E provides detailed plots of flow structure for all analyzed CFD cases and conditions for large flow.
- Appendix-F provides similar plots of flow structures for all analyzed CFD cases for small flow.
- Appendix-G provides details of the CFD mesh for ensuring sufficient refinement to adequately model velocity gradients at the model walls.
- Appendix-H provides details for ensuring that the dispersion error in the CFD-Evaluated Scale Effect is adequately represented by the CFD results.
- Appendix-J provides details for ensuring that the large flow CFD results are adequately within the expected range of the measured test results.
- Appendix-K provides details for ensuring that the CFD results to evaluate are adequately grid converged.
- Appendix-L provides the referential evaluation results for CFD-evaluated Scale Effect.
- Appendix-M provides details for ensuring that the grid refinement scheme employed in the CFD modeling conforms to the standards and guidelines. This Appendix is supplemental to Appendix-A.

## **2.0 OBJECTIVE**

### **2.1 Background**

Currently, for the purpose of understanding flow characteristics and verifying the performance of the ACC, the “Full-Height 1/2 Scale Confirmation Test” has been conducted (Ref.1). In flow with large Reynolds numbers, little influence of viscous effects is anticipated. Therefore, the 1/1 scale ACC prototype with even larger Reynolds numbers, will also have similar hydraulic performance as the 1/2 scale model. MHI proposes to apply the measured 1/2 scale hydraulic performance to the 1/1 scale ACC.

However, since there is little detailed information measured in the vortex chamber of the flow damper and near the throat section in existing experiments, there may not be enough evidence to validate the extrapolation to a 1/1 scale. To provide an adequate explanation, a sufficient understanding about the flow dynamics of the subject is important, especially flow inside the vortex chamber and the connecting piping (such as throat, diffuser and injection piping), which may include cavitation phenomena.

### **2.2 Objective**

With regards to the background mentioned above, a CFD analysis was done to better understand the flow structure and the cavitation phenomena in the ACC, and to better validate the extrapolation from the 1/2 to the 1/1 scale model.

In this investigation, the CFD analysis with cavitation model option is conducted, for the 1/2 and 1/1 scale model. The calculated data is evaluated as follows.

- To evaluate the flow behavior at quasi-steady-states for both small and large flow rate conditions.
- To evaluate the correlation between relevant parameters in the calculations of the 1/2 scale model and its corresponding measured data.
- To evaluate the significance of the CFD-evaluated Scale Effect by comparing the uncertainty in the CFD calculations with the difference in flow coefficient results from the 1/2 and 1/1 scale CFD (i.e. CFD-evaluated bias)
- To quantify the CFD-Evaluated Scale Effect, including the uncertainty in CFD calculations for application to the 1/1 scale ACC hydraulic performance.

### 3.0 CFD ANALYSIS

#### 3.1 System Descriptions

The accumulator system is one of the subsystems of the ECCS. There are four accumulators, one for each reactor coolant cold leg. The accumulators are vertically mounted cylindrical tanks located outside each steam generator and reactor coolant pump housing. The accumulators are passive devices that are filled with boric acid water and pressurized with nitrogen. The accumulators discharge water into the reactor cold leg when the cold leg pressure falls below the accumulator charge pressure.

The Advanced Accumulators of the US-APWR have internal passive flow dampers that inject at a large flow rate to refill the reactor vessel at the first stage of injection, and then reduce the flow as the accumulator water level drops. When the water level is above the top of the standpipe, water enters the flow damper through inlets at both the top of the standpipe and at the small flow pipe on the side of the vortex chamber, and injects water at a large flow rate. When the water level drops below the top of the standpipe, the water enters the flow damper only through the small flow pipe, and injects water at a small flow rate.

The two check valves in series on the injection line to the reactor cold leg are held closed by the pressure differential between the Reactor Coolant System (RCS) and the accumulator charge pressure (approximately 1,600 pounds per square inch differential (psid)). The water level in the accumulator, boron concentration, and nitrogen charge pressure can all be remotely adjusted during power operations. The accumulators are non-insulated and assume thermal equilibrium at the containment normal atmospheric operating temperature (approximately 70 to 120°F).

The accumulators are pressurized with nitrogen gas by a flow control valve in a common nitrogen supply line. The failure of the flow control valve is accommodated by a safety valve set at 700 psig with a (nitrogen) flow capacity of 90,000 ft<sup>3</sup> per hour. Likewise, each accumulator is equipped with a safety valve set at 700 psig and (nitrogen) flow capacity of 90,000 ft<sup>3</sup> per hour, which provides a margin from the normal operating pressure (640 psig), yet precludes overcharging by the associated safety injection pump.

### 3.2 Analysis Models

Analyses were conducted using the general-purpose Computational Fluid Dynamics simulation software package, ANSYS Fluent. Characteristics of the flow in this simulation are strong swirl flow in the small flow condition and nozzle flow with cavitation in the large flow condition. Fluent Version 12.0 was used, which includes a two-phase model, cavitation model (Ref.9) to evaluate cavitation, and can also analyze strong swirl flow fields.

Two separate analysis models were employed for the two different flow injection modes (i.e. large flow injection and small flow injection), in order to increase computational efficiency. It would be possible to calculate the two different flow injections with the same model. However, the flow phenomena and regions of interest differ between the two flow conditions (i.e. cavitation at the nozzle throat for large flow injection and swirling flow in the vortex chamber for small flow injection). Therefore, use of the same model would result in unnecessary regions being modeled at higher mesh resolutions and increased calculation time and computational costs. The development of two different models suitable for large or small flow injection modes is intended to reduce the overall number of mesh elements and computation cost by focusing on the areas of interest for each flow condition.

These CFD analysis models were developed mainly based on the methodology of “ASME V&V20 (Ref.8)”. The following materials were used as an aid: “NEA/SCNI/R(2007)5 (Ref.5)”, “Journal of Fluid Engineering Editorial Policy Statement on the Control of Numerical Discretization in CFD Applications (Ref.7)”, “Procedure for Estimation and Reporting of Uncertainty Due to Discretization in CFD Applications (Ref.6)”, and “Verification and Validation in Computational Science and Engineering (Ref.20)”. These guidance documents recommend verification of the following analysis modeling items, which are discussed in the corresponding sections:

- “Proper Geometrical Modeling” (Sec. 3.2.1 and Appendix-G)
- “Discretization and its uncertainty error estimation” (Sec. 3.2.2 and Appendix-A)
- “Selection of Appropriate Physics Modeling for the purpose”  
(Sec. 3.2.3, Appendices B and C)



### 3.2.1 Geometrical Modeling

Figures 3.2-1 and 3.2-2 show the analysis models for each flow injection case.

#### (1) For Large Flow Injection

1. The model for large flow injection consists of the ACC tank, the height of which extends to the water surface level, the standpipe with the anti-vortex cap, the small flow pipe with the anti-vortex plate, the vortex chamber, the outlet nozzle and the injection pipe up to the point of pressure measurement during testing. (See Note 1)
2. The inner configuration of the flow damper is precisely modeled.
3. The casing thicknesses of the vortex chamber, ducting etc. are neglected.
4. The tank water level is changed for each analysis condition because the tank water level changes as a function of time throughout the injection.

**(Note 1)** Water surface level is set at a stationary level for steady state analysis.

#### (2) For Small Flow Injection

1. The model for small flow injection consists of the ACC tank, the height of which is extended to the water surface level, the lower part of the standpipe (up to the water surface level), the small flow pipe with the anti-vortex plate, the vortex chamber, the outlet nozzle, and the injection pipe up to the point of pressure measurement during testing. (See Note 2)
2. The inner configuration of the flow damper is precisely modeled.
3. The casing thicknesses of the vortex chamber, ducting etc. are neglected.
4. The water levels in the tank and the standpipe are changed for each analysis condition because the water levels change as a function of time throughout the injection.

**(Note 2)** The boundary conditions used are flow-rate at the inlet of the small flow pipe and standpipe and pressure at the exit of the injection pipe.

#### (3) Modeling of 1/2 and 1/1 Scale Model

1. CFD-evaluated Scaling Effects are estimated by comparing the predicted results of the flow rate coefficients of the 1/2 scale and 1/1 scale models, as well as including the numerical uncertainty of the CFD calculations.
2. The dimensions of the 1/1 model were precisely doubled from those of the 1/2 scale model except for the standpipe height as shown in Table 3.2-1.
3. For both the 1/2 and 1/1 CFD models, the water levels in the tank and the standpipe are set at the same level for each analysis case as shown in Table 3.2-1. This is done because the experimental testing was performed for a 1/2 scale full-height model in which the height of the test tank and the height of water level were not scaled (see Ref. 1).

**Table 3.2-1 Comparison of Main Dimensions**

--	--



(a) Analysis Model for Large Flow



(b) Analysis Model for Small Flow

**Figure 3.2-1 Analysis Models for 1/1 Scale**



(a) Analysis Model for Large Flow



(b) Analysis Model for Small Flow

**Figure 3.2-2 Analysis Models for 1/2 Scale**

### 3.2.2 Mesh Configuration

Figure 3.2-3 and 3.2-4 show mesh configurations in the vortex chamber and the outlet nozzle. The number of mesh elements for each model are also shown in Figures 3.2-3 and 3.2-4.

For small flow injection, the velocity of vortex flow in the vortex chamber must be larger than that for the large flow injection. So a finer mesh configuration is employed in the regions near the chamber wall for small flow to properly resolve the boundary layer. For large flow, the critical wall regions are the areas in the outlet pipe downstream of the throat where cavitation may occur.

For scaling, the mesh configuration is as follows:

Step1) The mesh configuration of the 1/2 scale model is set as the baseline.

Step2) [

Step3) [

To make the  $Y^+$  value less than 300, the mesh thicknesses at the near-wall region are set as follows:

- (1) For the large flow condition, the mesh thickness is set so that  $Y^+$  becomes approximately 300 on the wall at the throat where the maximum velocity occurs (See Appendix-G).
- (2) For the small flow condition, the mesh thickness is set so that  $Y^+$  becomes approximately 70 on the inside walls of the vortex chamber (See Appendix-G).

Additionally, the meshes around the center of the vortex chamber are set to be much [

To estimate the numerical uncertainty due to discretization, the Grid Convergence Index (GCI) is introduced and performed in accordance with "ASME V&V20 (Ref.8)". The GCI is a semi-empirical uncertainty estimation method based on solution results for successively refined grids at three levels (i.e. coarse, normal, and fine). However in the ACC CFD analyses, due to computational resource limitations, the mesh size for 'coarse mesh' may not be completely refined to fulfill the requirement of the standard. As such, MHI enhanced the GCI method conservatively based on this standard, and evaluated the uncertainty about the 'fine mesh' solutions. A detailed discussions of the calculation of the GCIs are given in Appendix-A. 'Fine mesh' solutions are used to calculate the CFD-Evaluated Scale Effects. The typical mesh models are shown in Figure 3.2-3, 3.2-4.

As a result of using the GCI method in Appendix A, the following objectives are achieved:

- 1) The mesh configuration and its refinement are confirmed to be sufficient to address the dominant flow phenomena of interest.
- 2) The numerical uncertainties of the model are quantitatively estimated through the estimation of the discretization error by the GCI method.

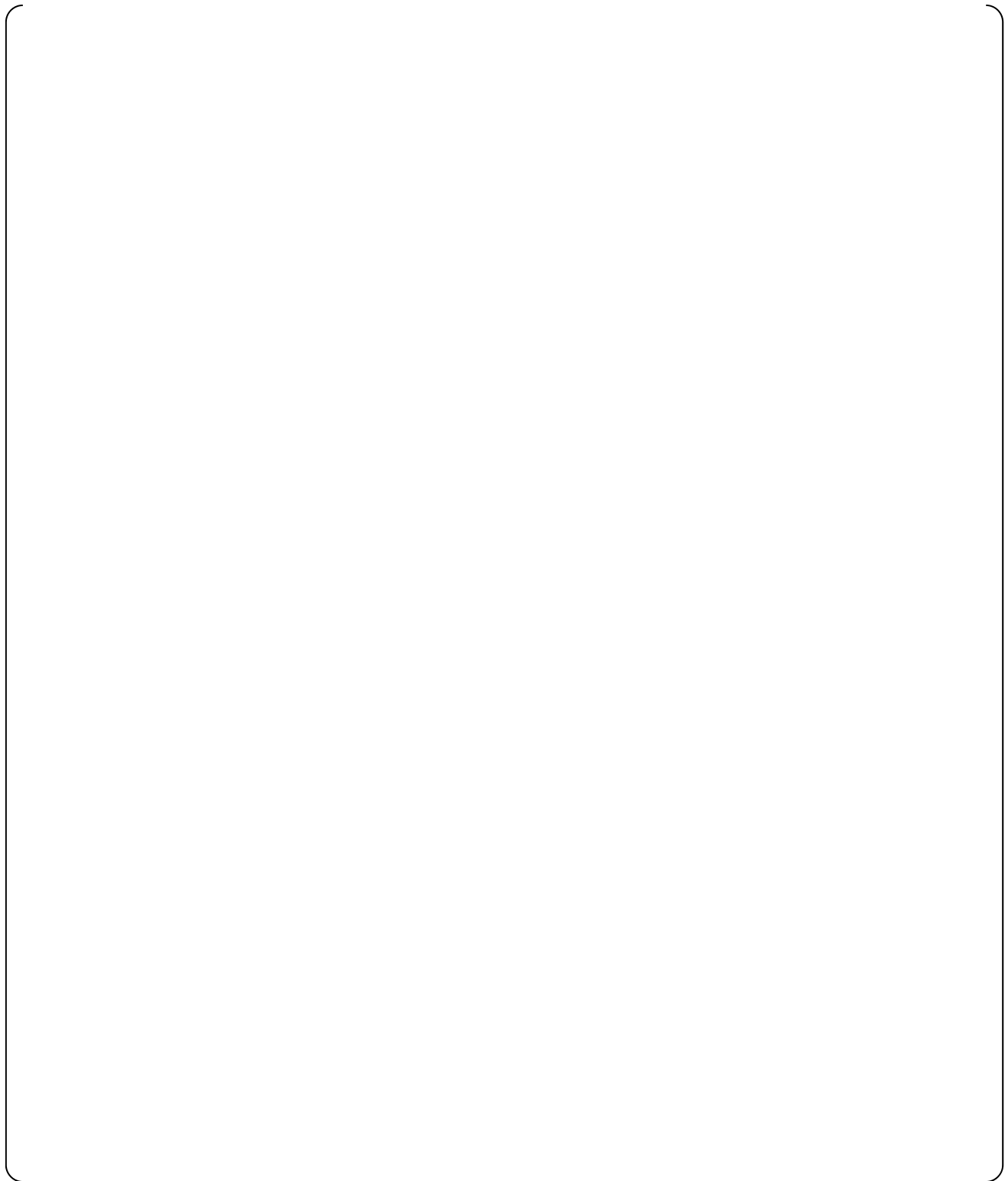


**Figure 3.2-3 Mesh Configurations of Vortex Chamber for 1/2 and 1/1 Scale Model for Large Flow**

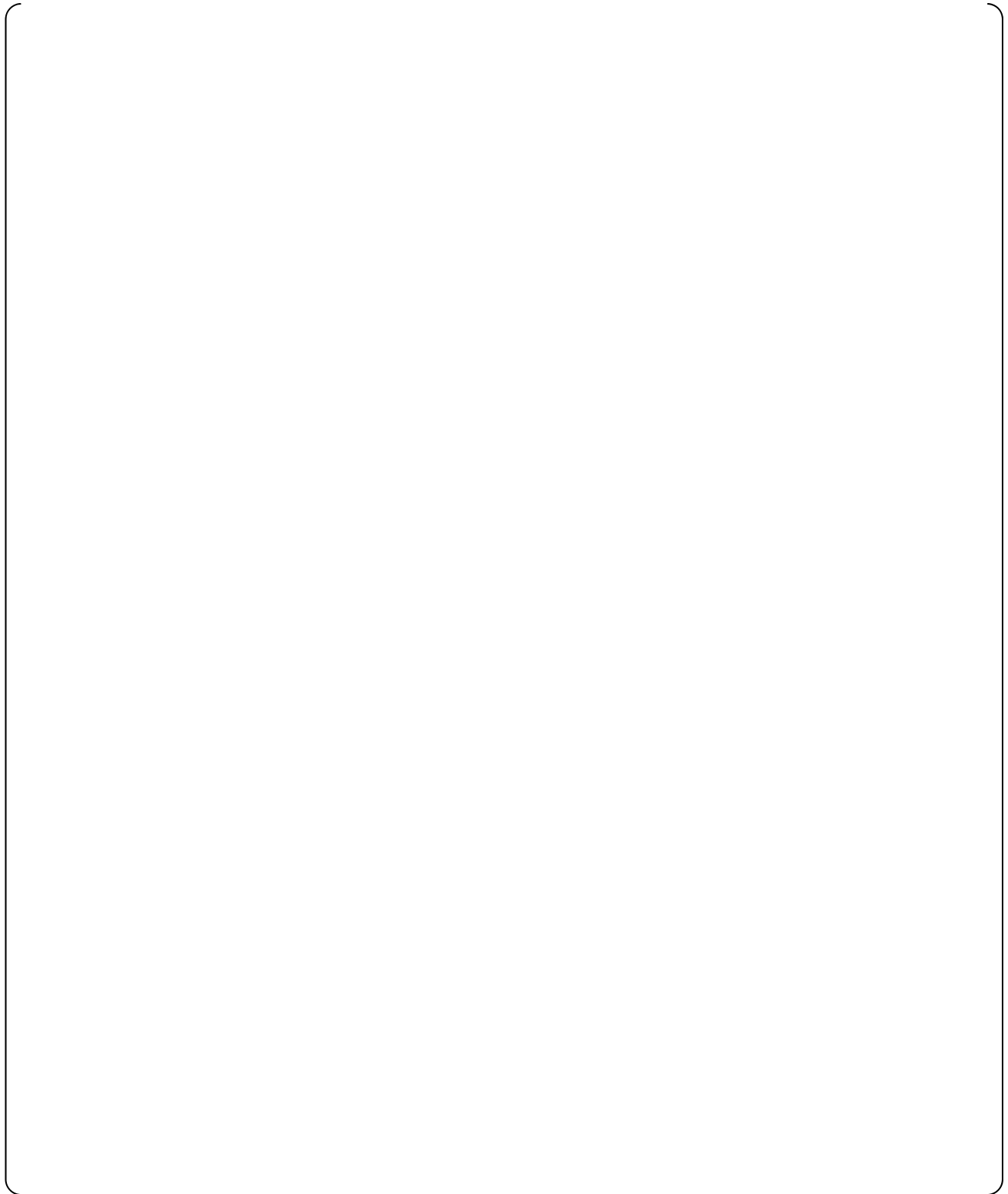


**Figure 3.2-4 Mesh Configurations of Vortex Chamber for 1/2 and 1/1 Scale Model for Small Flow**



### 3.2.3 Specification of the CFD Analyses

The CFD analyses were conducted and summarized on the following specification.

- **CFD Software:** Fluent Version 12.0 (See 3.2.3(1))  
(Commercial CFD software developed by ANSYS, Inc.)
- **Time Dependence:** Steady-State Calculation for large flow  
Unsteady-State Calculation for small flow (See 3.2.3(2))
- **Type of Fluid:** Incompressible Viscous Fluid
- **Turbulence Model:** RSM (See 3.2.3(3))
- **Near-Wall Treatment:** [ ] (See 3.2.3(4))
- **Multiphase Model:** [ ] (See 3.2.3(5))
- **Cavitation Model:** [ ] (See 3.2.3(8))
- **Spatial Discretization:**
  - a) Momentum Equation: [ ] (See 3.2.3(6))
  - b) Pressure Term: [ ] (See 3.2.3(7))
  - c) Turbulence Source Terms: [ ] (See 3.2.3(6))
- **Gravity:** Gravity is considered and Operating Density is zero to evaluate occurrence of cavitation and ensure that body forces and density are evaluated separately for the fluid and vapor phases.
- **Other:** No Modeling for evolution of Dissolved Nitrogen Gas

Details of the selection of specification are described as follows.

#### (1) CFD Software

Fluent Version 12.0, which includes three cavitation models, is used instead of Version 6.3 reported in Rev. 0 of this technical report so that cavitation models can be compared.

#### (2) Time Dependence

[ ]

#### (3) Turbulence Model

The Reynolds Stress Model (RSM) is a turbulence model which has greater potential to give accurate predictions for complex flows where swirl, rotation, and rapid directional

changes are dominating compared with other models such as one-equation and two-equation models. The RSM solves transport equations for the Reynolds stresses and the dissipation rate, abandoning the isotropic eddy-viscosity hypothesis (Ref. 3). [

]

#### **(4) Near-Wall Treatment**

[

]

#### **(5) Multiphase Model**

[

]

#### **(6) Spatial Discretization of Momentum Equation and Turbulence Source Terms**

[

]

#### **(7) Spatial Discretization of Pressure Term**

[

]

## (8) Cavitation Model

[

]

### 3.3 Test Case for Analysis

Among seven experimental test cases using the full-height, 1/2 scale test tank, Test Cases 3 and 6 were selected for CFD analysis conditions to cover the cavitation factor over a wide range (Ref.1).

Test Case 3 is the case in which the test tank has the highest initial pressure among all of the test cases in order to acquire the data for high pressure design. This case covers the range of smaller cavitation factors. The exhaust tank pressure was [ ] psig ([ ] MPa (gauge)) to simulate containment atmosphere pressure following the blowdown phase during a Large Break LOCA.

Test Case 6 has the smallest pressure difference between the test tank and exhaust tank in order to collect the data at larger cavitation factors. This case covers the range of large cavitation factors.

Three or four time points are selected for each test case in order to cover the initial stage, middle stage(s), and the end stage of ACC injection.

Consequently, a total of 26 calculation points are analyzed for 1/2 scale and 1/1 scale. Test conditions and analysis time periods for Test Cases 3 and 6 are shown in Table 3.3-1. Figure 3.3-1 shows these calculation points plotted on the 1/2 scale experimental test results.

The test cases shown in Table 3.3-2 were used as the typical conditions in the GCI evaluation described in Section 3.5.3. The earliest time point and the latest time point for each flow condition were used from each test case.

**Table 3.3-1 Test Cases and Time Points for Calculation**

--

**Table 3.3-2 Test Cases for GCI Calculation**

--

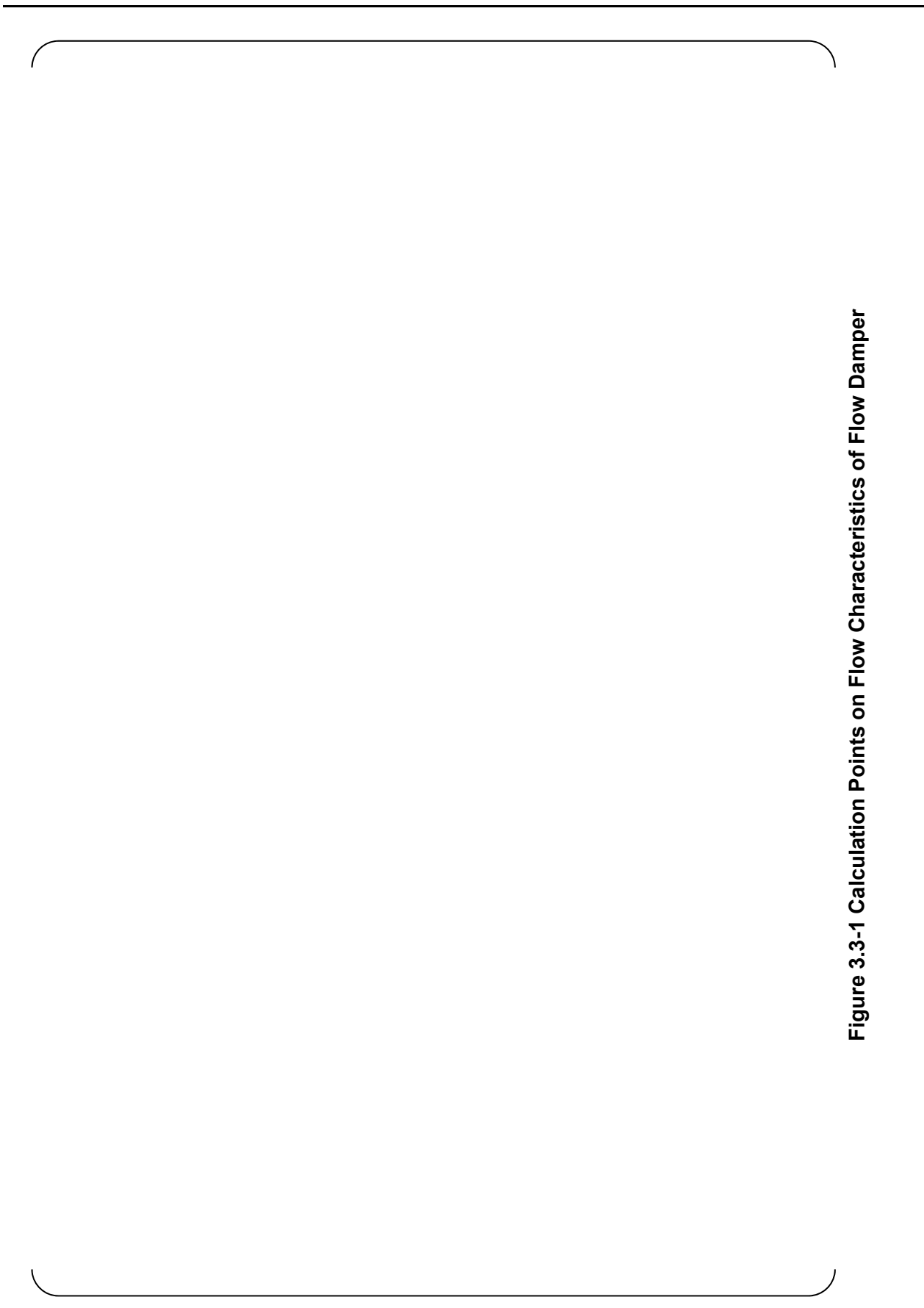


**Figure 3.3-1 Calculation Points on Flow Characteristics of Flow Damper**

### 3.4 Boundary Conditions

Table 3.4-1 lists the boundary conditions used for this CFD investigation.

The measured data obtained from the 1/2 scale test were applied to the analysis models (i.e. tank pressure, tank outlet pressure, tank water level, standpipe water level). Total flow rate was calculated from the time series variation of tank water-level. Only some corrections and modifications are considered as needed for each model. For physical reasons, the pressure boundaries were corrected to adjust for the pressure difference between 1/2 scale and 1/1 scale models (See Note 1 and Note 2). In the small flow injection case, due to the numerical instability, the flow rate was used for the inlet boundary condition instead of a pressure boundary because of the mass balance instability in the pressure boundary condition cases (See Note 2). In contrast, flow rate boundary cases gave numerically stable results. These adjustments on boundary conditions contribute toward obtaining reasonable results for the evaluation of scale effects. (See Appendix-D)

#### For Large Flow Injection Case:

- Inlet Boundary Condition: Tank Pressure (See Note 1)
- Outlet Boundary Condition: Outlet Pressure (See Note 2)

#### For Small Flow Injection Case:

- Inlet Boundary Condition:
  - > Standpipe: Inlet Flow Rate (Obtained by the time series variation of standpipe water-level. See Appendix-D)
  - > Small Flow Pipe: Inlet Flow Rate (See Appendix-D)
- Outlet Boundary Condition: Outlet Pressure (See Note 2)

#### **(Note 1)**

The analysis models consider the time series variation of tank water-level and gravitational effects.

For the large flow 1/2 scale model analysis, pressure boundaries are applied at the inlet and outlet boundaries and are set to the same pressure as the measured results. For the large flow 1/1 scale model analysis, the injection pipe elevation is 2 times higher than that of the 1/2 scale model due to scaling of the chamber outlet piping length while the tank water-level is at the same elevation as that of 1/2 scale model. Therefore, the difference between the tank water-level and the height at the exit of the injection pipe of 1/1 scale model is smaller than that of 1/2 scale model, which affects the gravitational head.

To account for this effect, inlet pressure is corrected as follows to provide the same driving force conditions while maintaining the same cavitation factor (See Eq. (5-4) in Ref.1):

$$P_{in1/1} = P_{in1/2} + \rho g (H_{out1/1} - H_{out1/2})$$

Where,

- $P_{in1/1}$  : Inlet pressure of 1/1 scale model  
 $P_{in1/2}$  : Inlet pressure of 1/2 scale model (Measured pressure)  
 $H_{out1/1}$  : The height at the exit of injection pipe of 1/1 scale model  
 $H_{out1/2}$  : The height at the exit of injection pipe of 1/2 scale model  
 $\rho$  : Density of water  
 $g$  : Acceleration of gravity

**(Note 2)**

The measured data obtained from 1/2 scale test were applied for the pressure condition at the exit of injection pipe.

Reference Pressure and Temperature for the Fluid Properties Calculations (Such as viscosity, density, and saturated pressure etc.)

- Temperature : The measured data shown in Table 3.4-1 (Constant value)
- Pressure : Sum of the following pressure values
  - 1) Corrected pressure (Gauge pressure)
  - 2) Atmospheric pressure (Reference pressure)

**Table 3.4-1 Boundary Condition Data for Calculation**



### 3.5 Analysis Results

First, the applicability of the CFD model to the ACC is evaluated. Then the CFD model is used to evaluate the scale effect between the 1/2 scale and 1/1 scale model.

#### 3.5.1 Applicability of CFD to ACC

The applicability of CFD to the ACC is assessed by comparison of the results of the 1/2 scale test to the results of its CFD analysis such as flow structure and  $C_v$  value. The appendices to this report include additional results and sensitivity analyses for critical model parameters to further justify and validate CFD applicability, as discussed in the proceeding sections.

##### (1) Flow Structure of 1/2 Scale Model

Flow structures of stream lines and flow vectors obtained by CFD are compared with the 1/5 scale visualized test which shows expected conceptual flow structures and has similar behaviors to the 1/2 scale model for the vortex chamber and the governing flow phenomena discussed in Reference 1. The CFD flow structure results are shown in Figures 3.5-1 and 3.5-3. Additional results are given in Appendices E and F. The chosen CFD case is comparatively similar to the test case shown in the figure. Additional details of the CFD flow structure are discussed below.

Figure 3.5-2 illustrates the flow in the vortex chamber on a simplified conceptual basis. As shown in Figure 3.5-2, a) in the large flow condition, the CFD results show that the flow from the standpipe and small flow pipe join together and the conflux flows out to the outlet nozzle without a strong vortex, which is similar to the flow structure of the test. Therefore, the main flow flows to the nozzle forming a U-shaped flow from the standpipe to the nozzle. This induces some flow separation at the inlet of the nozzle from the vortex chamber, but the separation does not continue to the throat due to the throttling effect of the reducer as shown in Figure E-1(b)-6(b) in Appendix-E. The pressure loss in this region is not significant because the throttling effect prevents significant flow separation. There are two permanent vortices in the vortex chamber as the flow reaches the far side of the chamber and returns to the nozzle outlet, shown in Figure 3.5-1. However, these vortices act as “rollers” to guide the main flow to the nozzle and do not develop large pressure losses. These permanent vortices differ from the strong vortex during the small flow phase described below. The flow velocity is accelerated from the outlet port of the vortex chamber to the throat in the reducer due to the reduction of the flow area, and reaches a maximum at the throat. The static pressure decreases due to the high velocity at the near-wall of the diffuser downstream of the throat and may cause cavitation. Thus, the majority of the pressure loss occurs at the diffuser downstream of the throat.

As shown in Figure 3.5-2 b), in the small flow condition, the CFD results show that the flow from the small flow pipe flows out to the outlet nozzle through a strong vortex in the vortex chamber, which is also similar to the flow structure of the experimental tests. In this vortex, a forced vortex with the same diameter as the throat is formed, and a large pressure loss is developed in this region due to the fluid viscosity. However, as shown in Figure 3.5-3 and the additional results in Appendix-E, the pressure distribution at the center of the

vortex shows that the static pressure is still much higher than the vapor pressure, and that cavitation does not occur. This can be observed in the void fraction distribution shown in Figure 3.5-4. In addition, centrifugal force increases pressure at the outer diameter of the vortex chamber and decreases pressure at the center of the vortex chamber. Viscosity reduces flow circulation in the boundary layers at the top and bottom faces of the chamber. These effects do not prevent radial flow at the boundary layers. Pressure recovers in the diffuser as the flow expands and allows reverse flow along the axis of the diffuser. This reverse flow exists in the vortex chamber, the outlet nozzle and the injection pipe. However as shown in Figure 3.5-5, the starting point of the reverse flow is approximately [ ] downstream from the outlet of the bend and back-flow does not initiate at the exit boundary.

Therefore, since it is confirmed that the 1/2 scale ACC CFD analysis shows similar flow structure to the expected conceptual flow and visualized data of 1/5 scale test, the CFD model can be applied to evaluate the scale effect.

## **(2) Relationship between Flow Rate Coefficient and Cavitation Factor**

The relationship between the flow rate coefficient ( $C_v$ ) and the cavitation factor ( $\sigma_v$ ) of the CFD model and test result is shown in Figure 3.5-6. The figure also shows the characteristic flow equations obtained from the test results with its corresponding 95% (2 standard deviation) uncertainty range based on the instrument uncertainty and dispersion deviation (Ref.2). The uncertainty range is shown by the broken line in Figure 3.5-6.

The general trend of the flow rate coefficient vs. cavitation factor is consistent between the test and CFD results. For the large flow condition, the flow rate coefficient decreases as the cavitation factor decreases. For the small flow condition, the flow rate coefficient is almost constant over the range of cavitation factors. Note that the very fine flow coefficient scale in Figure 3.5-6(b) magnifies the appearance of the minor differences in flow coefficient.

As shown in Figures 3.5-6(a) and 3.5-6(b) and Tables 3.5-1(a) and 3.5-1(b), for the large flow condition, the flow rate coefficients from the CFD results are within the range of instrument uncertainty and dispersion deviation of the test data, except for Case 3-5 sec. For the small flow condition, the flow rate coefficients from the CFD results are within the range of instrument uncertainty and dispersion deviation of the test data, except for Cases 3-125 sec and 6-82 sec. However, as shown in Tables 3.5-1(a)1 and 3.5-1(b)2, these points are very close to the lower  $2\sigma$  uncertainty limit of the characteristic equation, but these results are not significant outliers. Therefore, it is determined that the CFD results adequately model the general behavior and overall tendency of the characteristic equation.

In summary, the CFD model is acceptable to evaluate the scale effect between the ACC 1/2 scale and 1/1 scale models using the flow structure and  $C_v$  value of the 1/2 scale model.

### **(3) CFD Validation**

As described above, the occurrence of cavitation for the large flow and fluid pattern such as vortex formation for small flow in this simulation can be predicted by the CFD model. In addition, the relation of the flow rate coefficient to the cavitation coefficient can also be predicted by the CFD model. The CFD result is generally consistent with the experimental model test result although some differences can be observed. The CFD model solves the governing equations numerically and can evaluate the scale effects in principle. In addition, the physical models are developed from various experimental data and direct simulation data, and can also evaluate the scale effects. Detailed discussion with additional calculations to show the applicability of the adopted turbulence model, cavitation model, and boundary conditions are described in the following appendices.

Appendix-B discusses the development and scaling capability of the turbulence model. The turbulence model was developed empirically as a best-fit model for many flow applications and not specifically for the ACC flow application. However, the CFD-Evaluated scale effect is a differential evaluation between scales, and not an absolute evaluation between CFD and experimental test data. Appendix-B addresses the difference between the CFD result and the scaled model test results for small flow. These appendices demonstrate that the turbulence model can be applied to the ACC phenomena by adjusting the empirical constants to reduce the (absolute) error due to the turbulence model generalizations with minimal effect on the calculated (differential) scale effects.

Appendix-C includes a discussion and sensitivity analysis of the available cavitation models. This appendix demonstrates that the chosen cavitation model is appropriate for use in the ACC CFD models and selection of cavitation model has a minimal impact on results of the CFD analyses.

Appendix-D demonstrates that the chosen boundary conditions for small flow also have minimal impact on the CFD results. Appendix-I evaluates the impact of the turbulence model generalizations and chosen boundary conditions to demonstrate that cavitation occurrence during small flow has a minimal impact on the hydraulic performance of the flow damper.

Appendix-J validates the large flow CFD results by demonstrating that the results are within the instrument uncertainty of the measured test results.

Based on the discussions given in these appendices, the scale effects evaluated in this report using the generalized turbulence model, chosen cavitation model, and specified boundary conditions are determined to be valid.

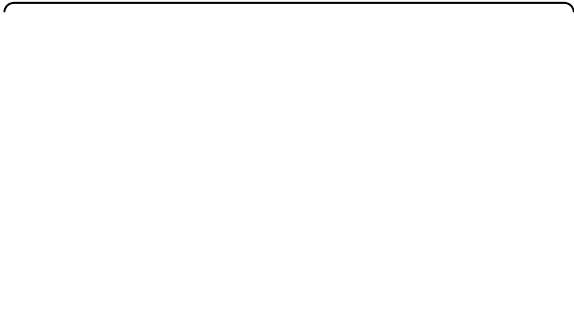


Figure 3.5-1(a) Flow Structure in Vortex Chamber (Large Flow)

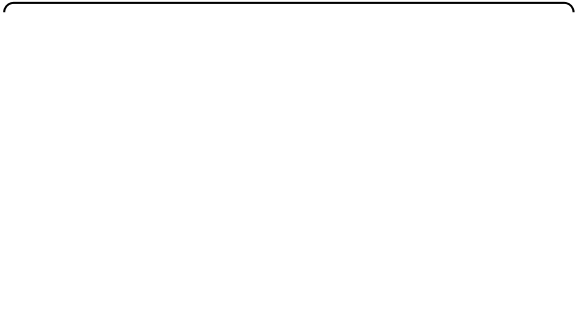


Figure 3.5-1(b) Flow Structure in Vortex Chamber (Small Flow)





**Figure 3.5-2 General Flow Structure**



**Figure 3.5-3 Static Pressure distribution (Small Flow Fine Mesh, Case 3, 43 sec)**



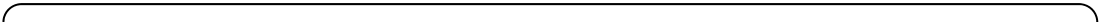
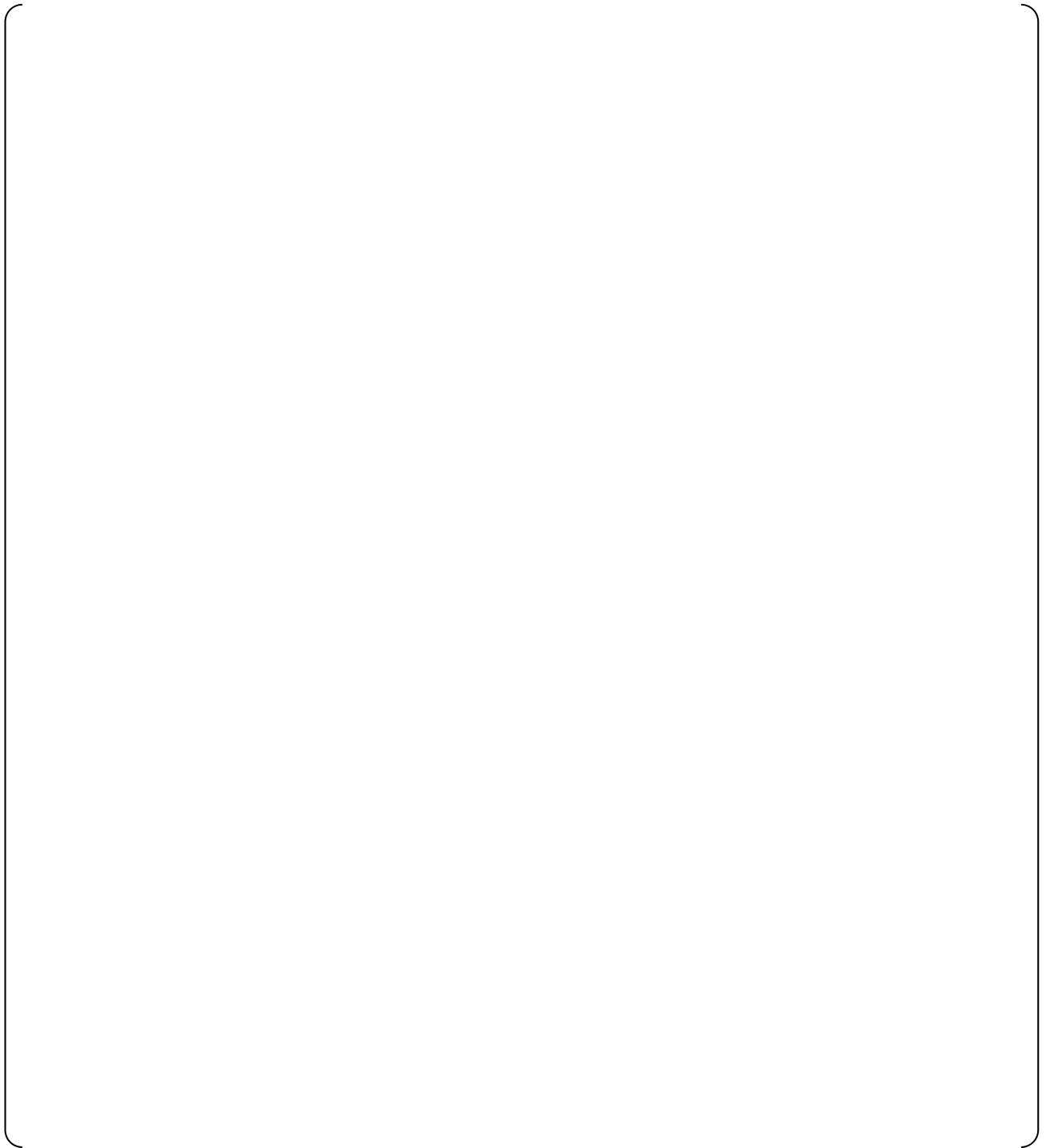


Figure 3.5-4 Void fraction distribution (Small Flow Fine Mesh, Case 3, 43 sec)





**Figure 3.5-5 Reverse Flow Confirmation**



**Figure 3.5-6(a) Comparison between Test Results and Calculation Results for Flow Rate Coefficient in Large Flow Condition**

**Figure 3.5-6(b) Comparison between Test Results and Calculation Results for Flow Rate Coefficient in Small Flow Condition**

**Table 3.5-1(a) Characteristic Equation and Calculation Results for Flow Rate Coefficient (Large Flow)**

**Table 3.5-1(b) Characteristic Equation and Calculation Results for Flow Rate Coefficient (Small Flow)**

### 3.5.2 Evaluation of Scale Effect Due to CFD

The scale effect is evaluated by comparing the CFD results such as flow structure and  $C_v$  value between the 1/2 scale and 1/1 scale models.

#### (1) Comparison of flow structure

The flow structure results comparing the 1/2 scale and 1/1 scale CFD models are shown in Figure 3.5-7 (Large Flow Case 3-5 sec) and Figure 3.5-8 (Small Flow Case 3-43 sec). The flow structures of the other cases are summarized in Appendices E and F.

The flow structure CFD results in both large and small flow conditions for the 1/1 scale model are similar to that of the 1/2 scale model with regard to static pressure, flow vector, and void fraction. The effect of these differences on hydraulic performance (i.e. flow coefficient) is quantified through the CFD-Evaluated Scale Effect calculated in Section 3.5.3.

#### Large Flow Injection

CFD results of both scale models show that the void fraction becomes large as the cavitation factor becomes small (See Figure 3.5-7 and Appendix-E). The flow behavior from the CFD model results for the large flow condition show a similar tendency between the 1/2 scale and 1/1 scale model with regard to void generation.

The CFD results also show that the two flows from the stand pipe and small flow pipe flow together in the vortex chamber without forming a strong vortex within the vortex chamber (See Fig 3.5-7(a)). This conflux separates into a portion that directly exits the outlet nozzle and a portion that exits the nozzle after reaching the far wall of the chamber and forming a small recirculation vortex in the vortex chamber. This recirculation vortex differs from the strong vortex which causes the large pressure drop during small flow. Some differences in the flow structures within the vortex chamber are observed between scales in confluence and separation. These will cause differences in the velocity profiles at the exit of the vortex chamber, which in turn will cause differences in the velocity, pressure, and void distribution at the outlet nozzle as shown in Fig 3.5-7(b).

Since the flow resistance for large flow is dominated by the throat of the outlet nozzle, differences in flow structure within the vortex chamber would have limited effect on the overall flow resistance. However, the quantitative CFD results shown in Section 3.5.3(2) demonstrate that the effect is very small. In other words, the overall flow resistance for large flow is insensitive to the differences in flow structure within the vortex chamber between scales. This discussion also applies to the results shown in Appendix-E

#### Small Flow Injection

A strong vortex in the vortex chamber is confirmed for both the 1/2 scale and 1/1 scale models as shown in Fig. 3.5-8. In addition, both scale models do not show void generation at the center of the vortex or the outlet nozzle (See Appendix-I for additional discussion of cavitation occurrence during small flow). Similar reverse flows from the

outlet nozzle to the vortex chamber and velocity distributions are observed between the 1/2 scale and 1/1 scale models (See Fig. 3.5-8). However, there are slight differences in static pressure in the vortex chambers and the outlet nozzles. The effect of these differences on the flow rate coefficient is evaluated in Section 3.5.3(2). This discussion also applies to the results shown in Appendix-F.

## **(2) Comparison of relationship between flow rate coefficient and cavitation factor**

In both large and small flow conditions, the flow rate coefficients agree well between 1/1 scale model and 1/2 scale model, as shown in Figure 3.5-9.

For the small flow phase, some differences in cavitation factors between scales are apparent in Figure 3.5-9 at large cavitation factors (Case 6). The small flow CFD model employs a flow inlet boundary condition for solution stability and calculates an inlet pressure. Differences in the cavitation factors for small flow are caused by differences in the calculated inlet pressure. These larger differences are caused by a larger numerical mesh uncertainty in Case 6 at larger cavitation factors for small flow injection which is represented using the Grid Convergence Index (GCI) as described later. The uncertainty due to the large GCI is appropriately taken into account in the LOCA safety calculations.

The scale effect is illustrated by Figure 3.5-10 with the abscissa representing scale and the ordinate representing the  $C_v$  value. The figure shows that relative differences of  $C_v$  for small flow are larger than that of large flow. However, the scale effects of  $C_v$  appear to be small. The scale effect quantified by CFD (i.e. CFD-Evaluated Scale Effect), between 1/2 scale and 1/1 scale is described in section 3.5.3 in detail.

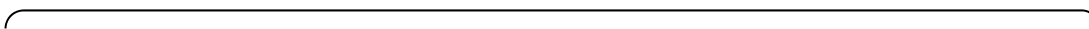


**Figure 3.5-7(a) Flow Structure in Vortex Chamber (Case 3 Large Flow 5 sec)**



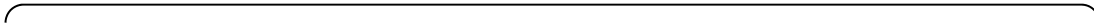


**Figure 3.5-7(b) Flow Structure in Outlet Nozzle (Case 3 Large Flow 5 sec)**



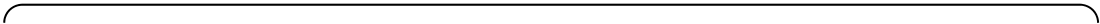


Figure 3.5-8(a) Flow Structure in Vortex Chamber (Case 3 Small Flow 43 sec)

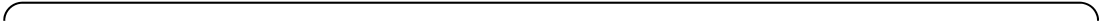


Figure 3.5-8(b) Flow Structure in Outlet Nozzle (Case 3 Small Flow 43 sec)







**Figure 3.5-9 Comparison between 1/2 and 1/1 Scale of CFD Result**



**Figure 3.5-10(a) Relationship between Flow Rate Coefficient and Scale (Large Flow)**



**Figure 3.5-10(b) Relationship between Flow Rate Coefficient and Scale (Small Flow)**

### 3.5.3 Evaluation of Scale Effect between 1/2 Scale and 1/1 scale

#### (1) Outline

The scale effect and its uncertainties obtained from the difference of CFD results between the 1/2 scale and 1/1 scale models are referred to as the “CFD-Evaluated Scale Effect” and are shown in this section.

#### (2) Scale Effect and Uncertainty

Possible scale effects between the 1/2 scale and 1/1 scale models are quantified from the CFD results for the 1/2 scale and 1/1 scale ACCs.

CFD-Evaluated Scale Effects between the 1/2 scale and 1/1 scale models are considered to be represented by an average of the calculated values and an uncertainty (i.e., dispersion) related to the calculated values. The average value is considered to be a bias error. The uncertainty in the mean value (bias error) may arise from two sources:

- Dispersion of the mean ( $u_{SD}$ ) from the calculated values of the scale effect at each analyzed test case / time point.
- Propagation of uncertainty ( $u_{mesh}$ ) in each calculated value of the scale effect from the numerical uncertainty in every 1/2 scale and 1/1 scale CFD result.

Therefore, the CFD-Evaluated Scale Effects are defined by the following expressions.

$$\begin{aligned} \text{CFD-Evaluated Scale Effects} &\approx (Cv_{1/1} - Cv_{1/2}) / Cv_{1/2} && \text{Eq. 3.5.3-1} \\ &\rightarrow \delta Cv_{scale} \pm u_{scale} \\ &(\text{statistical representation}) \end{aligned}$$

$\delta Cv_{scale}$  : Scale effect bias estimated from CFD results

(Scale effect bias is evaluated from the average, because  $Cv_{1/1}$  and  $Cv_{1/2}$  have a numeric error margin respectively.)

$u_{scale}$  : Standard ( $1\sigma$ ) uncertainty of the scale effect bias estimated from CFD results

$$[ \quad \quad \quad ] \quad \quad \quad \text{Eq. 3.5.3-2}$$

Each of the uncertainty components is considered to be normally (Gaussian) distributed, such that  $u_{scale}$  is calculated by the square root sum of squares as defined by the following expressions.

$$u_{\text{scale}}^2 = u_{\text{SD}}^2 + u_{\text{mesh}}^2 \quad \text{Eq. 3.5.3-3}$$

$$u_{\text{SD}} = C_{T,95}(n) / 1.96 \times \text{S.D.} \quad \text{Eq. 3.5.3-4}$$

(1 $\sigma$  standard uncertainty calculated from a two-sided 95% probability, based on limited number of results)

$$u_{\text{mesh}} = \text{Evaluated by GCI (Grid Convergence Index)} \\ \text{(The expression is described below in Section 3.5.3(3).)}$$

$u_{\text{SD}}$  : Standard (1 $\sigma$ ) uncertainty due to deviation from bias

$u_{\text{mesh}}$  : Standard (1 $\sigma$ ) uncertainty due to spatial discretization approximation for CFD calculations (GCI)

M.V. : Mean value of differences between 1/2 and 1/1 scale CFD

S.D. : Standard deviation of differences between 1/2 and 1/1 scale CFD

N : Number of data pairs (1/2 and 1/1 scale CFD cases)

$C_{T,95}(n)$  : Factors for tolerance interval to contain at least 95% of population (Table 3.5-2) (According to the "Test Uncertainty" (Ref.16))  
The validity of using  $C_{T,95}(n)$  is described in Appendix-H.

$Cv_{1/1,i}$  : Flow rate coefficient in case i obtained by CFD for 1/1 scale ACC

$Cv_{1/2,i}$  : Flow rate coefficient in case i obtained by CFD for 1/2 scale ACC

**Table 3.5-2 Factors for Calculating the Two-Sided 95% Probability Intervals for a Normal Distribution (Ref.16)**

Number of Given Observations	Factors for Tolerance Interval to Contain at Least 95% of the Population
n	$C_{T,95}(n)$
4	6.37
5	5.08
6	4.41
7	4.01
8	3.73
9	3.53
10	3.38
11	3.26
12	3.16
15	2.95
20	2.75
25	2.63
30	2.55
40	2.45
60	2.33
$\infty$	1.96

### (3) GCI Uncertainty

According to the “ASME V&V 20-2009” (Ref.8), GCI can be understood as,

- Uncertainty of the solutions derived from discretized equations by a numerical and analytical approach.
- Its uncertainty is at 95% confidence level and that is consistent with the 1.96 sigma range for a Gaussian distribution.

On page 11 of ASME V&V 20-2009, it states,

*“uncertainty estimate  $U_{x\%}$  is intended to provide a statement that the interval  $f \pm U_{x\%}$  ( $f$  is numerical solution) characterizes a range within which the true (mathematical) value of  $f_t$  falls, with probability of  $x\%$ .”*

Also on page 12 of ASME V&V 20-2009, it states,

*“The GCI is an estimated 95% uncertainty obtained by multiplying the absolute value of the (generalized) RE error estimate (or any other ordered error estimator) by an*

*empirically determined factor of safety,  $F_s$ . The  $F_s$  is intended to convert an ordered error estimate into a 95% uncertainty estimate.”*

- Numerical uncertainty ( $u_{\text{mesh}}$ ) is evaluated using GCI, which is defined as a ~95% confidence interval for the numerical error.
- For the purpose of combining with other uncertainties (i.e. coverage factors for converting expanded uncertainty to standard uncertainty), the GCI is assumed to be a normal Gaussian distribution (i.e. 95% coverage =  $1.96\sigma$ ).
- Numerical uncertainty ( $u_{\text{mesh}}$ ) in the calculation of the CFD-Evaluated Scale Effect is a standard uncertainty ( $1\sigma$ ) estimated by dividing the GCI (95% coverage) by 1.96.
- For simplicity, the maximum value of the combined GCI at each evaluated point is used.

$u_{\text{mesh}}$  is defined by the following expressions.

$$\left[ \begin{array}{c} \text{Eq. 3.5.3-5} \\ \text{Eq. 3.5.3-5} \end{array} \right]$$

#### **(4) Results**

The uncertainties in the ACC flow model are shown in Table 3.5-3 and 3.5-4. The CFD-Evaluated Scale Effects with one standard deviation ( $1\sigma$ ) are evaluated [ ] % for small flow conditions, and [ ] % for large flow conditions respectively.

[illegible][illegible]

$u_{scale}$  of the small flow condition model is larger than that of the large flow model, due to the relatively large GCIs of the small flow cases. The larger GCIs can be attributed to the complicated flow field due to the vortex behavior in small flow conditions, where the velocity gradient is steeper than that during large flow conditions as shown in Figures 3.5-7 and 3.5-8. This complicated flow during small flow conditions requires more grid resolution to capture the flow behavior accurately. However, the current CFD results and grid resolutions can be considered to be sufficient to address the scale effect, since averaged scale effect is smaller compared to the experimental uncertainties.

As is discussed in Appendices B and C, the primary models in the CFD analyses are valid to address the scale effect of the hydraulic behaviors dominating the accumulator flow rate behavior. Since the numerical uncertainty is the major component of the CFD-Evaluated Scale Effect, in particular for small flow conditions, the present CFD analyses can be considered adequate to demonstrate that the scale effect is small.



## 4.0 CONCLUSIONS

The ACC topical report (Ref. 1) discussed the scaled model testing and development of the characteristic equation for the hydraulic performance of the 1/2 scale, full-height, ACC model. Reference 1 also discussed the governing flow phenomena and scalability concerns to conclude that the scale effect from applying the 1/2 scale ACC hydraulic performance to the 1/1 scale ACC is expected to be small.

This technical report evaluates the steady-state flow of CFD analyses using Fluent for the 1/2 scale and 1/1 scale analytical models. Conditions for the CFD calculation include both large and small flow injections for a wide range of cavitation factors. The results demonstrate the similarity of the flow characteristics, support the validity of the conclusion described in the topical report, and also provide quantitative evaluations of the scale effect using CFD for application to the characteristic equations for the 1/1 scale ACC hydraulic performance.

Conclusions of the CFD results and the evaluations are shown below:

- The 1/2 scale ACC CFD analysis shows similar flow structure to the expected conceptual flow in the flow damper.
- The CFD analyses are applicable for evaluations of large and small flow injections. In the 1/2 scale ACC analysis, the correlation between  $C_v$  and  $\sigma_v$  was reasonably consistent with the experimentally measured data, showing that CFD is applicable to estimate the scale effects in the ACC.
- CFD calculations indicated good similarity for the flow structure in the flow damper and in the injection piping between the 1/2 scale and 1/1 scale ACCs.
- The scale effect bias for the characteristic equations is quantified by comparing the CFD calculation results for both the 1/2 scale and 1/1 scale ACCs, which showed that the average scale effect bias is small compared to the experimental uncertainties.
- The CFD-Evaluated Scale Effect, which includes the uncertainty in the scale effect bias calculated through CFD analyses, is quantified for application to the characteristic equations for 1/1 scale ACC hydraulic performance.

## 5.0 REFERENCES

- 1) Topical Report "The Advanced Accumulator", MUAP-07001 Revision 5
- 2) Large Break LOCA Code Applicability Report for US-APWR, MUAP-07011
- 3) ANSYS FLUENT, FLUENT 12.0 Documentation, User's Guide and Validation Guide
- 4) Roache, P.J. (1994), Perspective : A Method for Uniform Reporting of Grid Refinement Studies, Journal of Fluids Engineering, Vol.116, pp.405-413
- 5) Best Practice Guidelines for the Use of CFD in Nuclear Reactor Safety Applications, NEA/CSNI/R(2007)5
- 6) Celik, I.B., Ghia, U., Roache, P.J. and Freitas, C.J., Procedure for Estimation and Reporting of Uncertainty Due to Discretization in CFD Applications
- 7) Statement on the Control of Numerical Accuracy, Journal of Fluids Engineering Editorial Policy
- 8) Standard for Verification and Validation in Computational Fluid Dynamics and Heat Transfer, ASME V&V 20-2009
- 9) T. Watanabe, T. Kawamura, Y. Takekoshi, M. Maeda, S.H. Rhee, Simulation of steady and unsteady cavitation on a marine propeller using a RANS CFD code, Fifth International Symposium on Cavitation, Osaka, Japan, November 2003
- 10) CFD Simulation of Flow in Vortex Diodes, AIChE Journal, Vol.54, No.5, P1139-1152, May 2008
- 11) A.K. Singhal, M.M Athavale, H. Li, Y. Jiang, Mathematical Basis and Validation of the Full Cavitation Model, Journal of Fluids Engineering, Vol. 124, PP 617 – 624, September 2002
- 12) P.J. Zwart, A.G. Gerber, T. Belamri, A Two-phase Flow Model for Predicting Cavitation Dynamics, ICMF 2004 International Conference on Multiphase Flow, Yokohama, Japan, May 2004
- 13) G.H. Schnerr, J. Sauer, Physical and Numerical Modeling of Unsteady Cavitation Dynamics, 4th International Conference on Multiphase Flow, New Orleans, USA, May 2001
- 14) TRAC-M/FORTTRAN 90(version 3.0) theory manual, LA-UR-00-910, J.W. Spore, pp F- 13, July 2000
- 15) Best Practice Guideline for the CFD Simulation of Flows in the Urban Environment APPENDIX A, COST Action 732, 1 May 2007,
- 16) Test Uncertainty, ASME PTC 19.1-2005(Revision of ASME PTC 19.1-1998)
- 17) S. Huang, M. He, C. Wang and X. Chang, Simulation of Cavitating Flow Around a 2-D Hydrofoil, Journal of Marine Science and Application, Vol. 9, No. 1, pp 63-68, 2010

- 18) M. Dular, R. Bachert, B. Stoffel, B. Sirok, Experimental Evaluation of Numerical Simulation of Cavitating Flow Around Hydrofoil, European Journal of Mechanics B/Fluids, Vol. 24, pp 522-538, 2005
- 19) Andreas P. Keller, Hubert K. Rott, The Effect of Flow Turbulence on Cavitation inception, ASME Fluids Engineering Division Summer Meeting FEDSM 97 June 22-26, 1997.
- 20) Roache, P.J., "Verification and Validation in Computational Science and Engineering", Hermosa Publishers, New Mexico, 1998.
- 21) Salas, M.D., "Some Observations on Grid Convergence" Computers and Fluids, Vol.75, No.7, Aug.2006, pp.688-692.

## Appendix-A

### Calculation of GCI

To estimate the spatial discretization errors in the CFD models, the Grid Convergence Index (GCI) is employed. This appendix describes the GCI calculation procedure and the results provided in the body text section 3.5.3. A modification with an additional conservatism is applied to the original GCI calculation procedure in the course of the examination.

#### (1) Procedure for Uncertainty Estimation and its requirements

This section describes the procedure of GCI calculation and its requirements. There are several published references about GCI calculation procedure (Ref.5, 6, 7 8, 15, and 20). The common procedure is as follows:

##### Step 1.

Define a representative cell, mesh or grid size,  $h$ . For three dimensional calculations,

$$h = \left( \frac{1}{N} \sum_{i=1}^N (\Delta V_i) \right)^{1/3} \quad \text{Eq. A1}$$

where

$\Delta V_i$  is the volume and  $N$  is the total number of cells used for the computations.

For the ACC evaluation, the total number of cells is based on the mesh of the Standpipe, Vortex Chamber, Outlet Nozzle and Injection Pipe.

##### Step 2.

Select three significantly different sets of grids and run simulations to determine the values of key variables important to the objective of the simulation study ( $\phi$ ).

It is recommended that the grid refinement factor,  $r = h_{coarse} / h_{fine}$ , be greater than 1.1 (Ref.4). This value of 1.1 is based on experience and not on formal derivation.

##### Step 3.

Let  $h_1 < h_2 < h_3$  and  $r_{21} = h_2 / h_1$ ,  $r_{32} = h_3 / h_2$ , and calculate the apparent order,  $p$ , of the method using the expression,

$$p = \frac{1}{\ln(r_{21})} \left| \ln \left( \varepsilon_{32} / \varepsilon_{21} \right) + q(p) \right|, \quad \text{Eq. A2}$$

$$q(p) = \ln \left( \frac{r_{21}^p - s}{r_{32}^p - s} \right), \quad \text{Eq. A3}$$

$$s = 1 \cdot \text{sign}(\varepsilon_{32} / \varepsilon_{21}) \quad \text{Eq. A4}$$

where

$$\varepsilon_{32} = \phi_3 - \phi_2, \quad \varepsilon_{21} = \phi_2 - \phi_1, \quad \phi_k \text{ denoting the solution on the } k^{\text{th}} \text{ grid.}$$

Here, parameter “s” (Eq. A4) is the indicator of “Oscillatory Convergence”. If “s = 1”, that means the grid convergence under consideration is monotonic. On the other hand, if “s = -1”, that means the grid convergence is oscillatory. By considering “s” in Eq. A3, this calculation procedure provides GCI even if the grid convergence under consideration has oscillatory convergence characteristics.

#### Step 4.

Calculate the extrapolated values from

$$\phi_{ext}^{21} = (r_{21}^p \phi_1 - \phi_2) / (r_{21}^p - 1). \quad \text{Eq. A5}$$

#### Step 5.

Calculate and report the following error estimates, along with the apparent order of  $p$  :  
Approximate relative error:

$$e_a^{21} = \left| \frac{\phi_1 - \phi_2}{\phi_1} \right|$$

Extrapolated relative error:

$$e_{ext}^{21} = \left| \frac{\phi_{ext}^{21} - \phi_1}{\phi_{ext}^{21}} \right| \quad \text{Eq. A7}$$

The fine-grid convergence index:

$$\text{GCI}_{\text{fine}}^{21} = \frac{\text{Fs} \cdot e_a^{21}}{r_{21}^p - 1} \quad \text{Eq. A8}$$

The empirical factor of safety,  $F_s$ , is introduced to ensure a GCI with a 95% confidence interval. Originally  $F_s$  was assigned a value of 3 for two-grid studies (Ref.4), but Roache has subsequently recommended a less conservative value for  $F_s$  ( $F_s=1.25$ ), but only when using at least three grid solutions and the observed  $p$  (Ref.20). ASME V&V20 (Ref.8) recommends that a value of  $F_s=1.25$  be used with three-grid studies involving structured grid refinement. The standard also states that “a base grid may be unstructured, but the grid sequence may be generated by structured refinement of an unstructured grid”. For unstructured grid refinement, the standard states “Until a sufficient data set is collected and studies are completed for unstructured refinement, it is generally recommended that the more conservative value of  $F_s=3$  be used”.

To evaluate the GCIs properly, ASME V&V20 describes the following 2 requirements during the procedure. One is ‘systematic grid refinement’ in Step 2, and the other is ‘the observed order  $p$  is constant for a simulation series’ in Step 3. As for ‘systematic grid refinement’ also called ‘structured grid refinement’, ASME V&V20 indicates “It is highly recommended not to use different grid refinement factors in different directions”. As for “the observed order  $p$  is constant for a simulation series”, the standard implies “the three-grid solutions for the observed order  $p$  are in the asymptotic region for the simulation series”.

## **(2) Grid refinement scheme for ACC CFD**

This section discusses the mesh refinement methodology to show that the convergence behavior of the results is asymptotic to support an estimation of numerical accuracy.

The current CFD model generally employs a structured grid meshing scheme, although an unstructured meshing scheme is used for some regions to provide sufficient spatial resolution to precisely evaluate the fluid turbulence behavior. Specifically, a finer mesh structure is used in the region near the wall surface to satisfy the required  $Y^+$  number to account for the fluidic interaction effect near the wall. For the other interior regions, the mesh sizes are appropriately optimized to simulate the fluid behavior occurring in each region of the ACC.

In estimating the spatial discretization errors/uncertainties (GCI), which are included in the LOCA scaling bias (Ref.1), the following grid refinement scheme (mesh size sensitivity) is taken into account:

- 1) The reference mesh structure described above was treated as the ‘fine’ mesh case.
- 2) The mesh sizes were made coarser in two steps; the first step was referred to as the ‘normal’ mesh case and the second as the ‘coarse’ mesh case.
- 3) The mesh size near the wall surface satisfies the required  $Y^+$  in the radial direction in the ‘fine mesh’ and was sequentially coarsened corresponding to the ‘normal mesh’ and ‘coarse mesh’.

ASME V&V20 recommends that the grid refinement should be made systematically. In addition, the mesh size ratio between the 'coarse' and 'normal' cases and/or the 'normal' and 'fine' cases should be more than 1.3 based on experience (Ref.4).

Since the advanced accumulator CFD model employs both structured and unstructured mesh schemes, the spatial volume (except the region near the wall) was divided into the following five sections (see Figure A2-1):

- Section 1: Outer annular region of flow damper
- Section 2: Middle annular region of flow damper
- Section 3: Inner core region of flow damper
- Section 4: Reducer region of outlet nozzle
- Section 5: Diffuser region of outlet nozzle

Within each section, a systematic grid refinement was made with approximately the same grid refinement ratio, defined by  $r = h_{coarse} / h_{fine}$ , in each different direction (i.e.  $r$ ,  $\theta$ , and  $z$  for structured mesh regions and  $r$ - $\theta$  and  $z$  for unstructured mesh regions). Here,  $h_{fine}$  and  $h_{coarse}$  are the representative grid size of the 'fine' and the 'coarse' mesh models, respectively. For the unstructured mesh, the effective refinement ratio  $r_{effective}$  was calculated using  $r_{effective} = (N_{fine} / N_{coarse})^{1/D}$  in accordance with section (1) of this Appendix. Here,  $D$  is the dimension number of the CFD model, and  $N_{fine}$  and  $N_{coarse}$  are the grid counts of the 'fine' and 'coarse' mesh models, respectively. Note that the mesh size in the region near the wall surface is refined separately with a grid refinement ratio similar to that used in the interior regions. This overall grid refinement scheme conforms to the ASME V&V20 requirement that the grid refinement should be made systematically even if the grid is unstructured. Typical Mesh Appearance are shown in Figure A2-2 to A2-4. The detailed grid refinement data for all cases used to evaluate the GCI are shown in Appendix-M.

The meshes are sufficiently refined in a systematic manner overall. In some portions of the unstructured mesh, the effective grid refinement ratio varies in different directions due to additional refinements needed to provide sufficient mesh quality, in accordance with the Best Practice Guideline (Ref.5, Section 6.2.3, Grid Quality). As is commonly observed in automatic mesh generation, the auto-mesh generation function of CFD codes may not initially provide sufficient mesh quality or appropriate meshes for unstructured meshes, and manual optimization and adjustment should be made to provide an appropriate mesh structure to model the physical phenomena observed/expected in the CFD simulation and meet mesh quality criteria in the Guidelines (Ref.5). If the applied mesh sizes are small enough however, the difference in mesh lengths does not significantly affect the converged (i.e. theoretical) solution. Reference 21 provides an example in which the applied mesh sizes are small enough and an equivalent observed p-value is obtained with different mesh structures (different cell aspect ratios). In other words, the net effect of the difference in the cell aspect ratio on the converged solution and the resultant GCI is negligible if the mesh resolution is fine enough to be within the asymptotic region.

This explanation is supported by the fact that the mesh convergence trend for the 'normal' to 'fine' meshes is almost the same between the 1/1 scale and 1/2 scale cases for the large flow Case 03-005sec (Figure A2-5). Here, the grid refinement is systematic for all three directions only in the 1/2 scale case, while the 1/1 scale case has a non-systematic deviation in the z-direction grid refinement of the outlet nozzle diffuser (Tables A2-1 (a) and A2-1 (b)). Similar convergence within the asymptotic region is observed in both grid refinement cases. Similar deviations in grid refinement can be found in other cases. No unexplainable mesh convergence trends are observed for any of the cases, indicating that the 'normal' and 'fine' mesh results are within the asymptotic region. Therefore, the applied refinement scheme is sufficient to evaluate the GCI.



**Figure A2-1 Schematic of Division for ACC CFD Meshing**





**Figure A2-2 CFD Mesh Configurations (Fine Mesh)**



**Figure A2-3 CFD Mesh Configurations (Normal Mesh)**



**Figure A2-4 CFD Mesh Configurations (Coarse Mesh)**



**Figure A2-5 Grid Convergence Trend (Large Flow, Case03-05sec)**

### (3) Application to ACC CFD

By following the procedure shown in section (1), GCIs are calculated. Here, the variable to be evaluated( $\phi$ ) is flow rate coefficient CV, and tank pressure, Pg.

Tables A3-1 and A3-2 show the GCI calculation procedure for Cv and its evaluation results for 1/2 scale and 1/1 scale, respectively. Similarly, Tables A3-3 and A3-4 are for Pg, however on only some of small flow condition cases (Case 3-43 sec, and Case 6-82 sec). Figures A3-1 and A3-2 show the representative grid convergence trend curves (Cv and Pg) for 1/2 scale and 1/1 scale, respectively.

In regard to the observed p-values, the calculation results show larger order than the theoretical value, which is expected to be within between 1 to 2 corresponding to the numerical scheme employed in this calculations as shown in the body text section 3.2.3 'Specification of the CFD Analysis'. As shown in Equation A8 of this Appendix, p-value affects GCI estimation. In this case, greater a p-value makes the GCI lower. This may be an indication of not conforming to the standard's requirement that "the three-grid solutions for the observed order p are in the asymptotic region for the simulation series". In other words, indicating that grid convergence may be not sufficient. In order to avoid uncertainty due to this insufficiency, a larger [ ] was used to evaluate the GCI, in accordance with the Guideline (Ref.5).

Consideration and treatment of this issue is explained in the proceeding sections of this appendix.


**Table A3-1 Calculation Procedure of GCI for 1/2 Scale Model CFD**  
**( $\phi$  = Flow Rate Coefficient Cv)**

**Table A3-2 Calculation Procedure of GCI for 1/1 Scale Model CFD**  
**( $\phi$  = Flow Rate Coefficient Cv)**





**Figure A3-1 Representative Grid Convergence Trend Curve  
for  $C_v$  (Flow Rate Coefficient) and  $P_g$  (Tank Pressure)  
with 1/2 Scale Model**



**Figure A3-2 Representative Grid Convergence Trend Curve  
for  $C_v$  (Flow Rate Coefficient) and  $P_g$  (Tank Pressure)  
with 1/1 Scale Model**



#### **(4) Explanation of the observed p-values**

This section discusses the observed convergence trends in the CFD results and the impact on the calculated GCI through the observed order of convergence.

The current CFD model employs a mixed order numerical scheme, such as a first order scheme for the pressure term and turbulence source terms and a second order scheme for the other terms in the momentum conservation equation. As a result, the converged p-value is expected to be approximately [ 1.5 ]. Roache recommends that the observed p-value be evaluated and compared with the expected p-value to provide an indication of whether the grids are in the asymptotic region (Ref.6). Note that Roache states at the same time that disagreement of the observed p-value and the expected p-value should not necessarily be taken as a sign of unsatisfactory calculations. However, due to computational resource limitations, the mesh size for the 'coarse mesh' may not be completely refined to ensure that all three mesh structures are within the asymptotic region.

In section (3) of this appendix, the observed p-values from the grid (mesh) sensitivity calculations for each case used in evaluating the GCI and LOCA scaling bias are provided, which are larger than the expected p-value. In particular for the large flow injection, the observed p-values are significantly larger than the expected p-value. This results in a smaller GCI and corresponding LOCA bias since the grid sensitivity appears to converge more rapidly than the expected p-value. The large observed p-value is caused by the fact that the 'coarse mesh' is outside of the asymptotic region. Only the 'coarse mesh' significantly deviates from the asymptotic curve of [ 1.5 ], while the 'normal' and 'fine' meshes provide an approximately linear grid convergence. This indicates that the spatial resolution in the 'coarse mesh' is too coarse to represent higher-order turbulence behaviors, while 'normal mesh' and 'fine mesh' are sufficiently refined to resolve the flow field under consideration.

#### **(5) Confirmation of the grid convergence for the 'normal mesh model' and 'fine mesh model'**

This section discusses additional CFD calculations performed to demonstrate mesh resolution adequacy for the 'normal' and 'fine' mesh and demonstrate that these cases are within the asymptotic region for grid convergence.

Eight cases out of 16 total cases were re-evaluated. ASME V&V20 Section 2-5 suggests an effective and efficient solution verification exercise approach, where once a detailed grid convergence study is executed, this base grid resolution is then used in all subsequent simulations for the particular problem. The eight chosen cases are representative of both flow conditions. For the large flow phase, Case 003-005 sec and Case 006-005 sec are evaluated for both the 1/1 scale model and 1/2 scale model (total of four cases). Case 003-043 sec and Case 006-082 sec are similarly evaluated for both scales (total of four cases) for the small flow phase (See Figure A5-1).

For this evaluation, a new 'intermediate mesh' between the 'coarse mesh' and 'normal mesh' cases was constructed. The grid convergence status for this additional 'intermediate' mesh result is depicted in Figure A5-2. As shown in this figure, the grid

convergence trend curve is monotonic and approaching the expected asymptotic curve calculated using an assumed [ ], demonstrating the validity of the grid refinement scheme developed to evaluate the ACC flow rate characteristics.

The re-evaluated observed p-values are shown in Table A5-1. The revised grid convergence trend for each case is shown in Figure A5-3 for large flow and Figures A5-4 and A5-5 for small flow.

For the large flow condition cases in which the existing observed p-value calculated in section (3) of this appendix is significantly larger than the expected p-value, the re-calculated observed p-values are within the range of 1.7 to 3.9 based on the additional 'intermediate', 'normal', and 'fine' meshes. These values are approaching the expected value of '1.5'. This demonstrates that the examined grid set (i.e. intermediate, normal, fine) is within or at least very close to the asymptotic region. This indicates that smooth convergence is attained in terms of the grid refinement, and the spatial resolution for at least the 'normal mesh' and 'fine mesh' is adequate for the physical evaluation of the numerical solution.

As for the small flow condition cases, the existing grid set (i.e. coarse, normal, fine) was confirmed to be within the asymptotic region by comparison with an additional grid similar to the large flow cases. However, the existing observed p-values are very close to the expected values for small flow and the small flow cases tend to reach the asymptotic region at cell counts of about 0.8 million (i.e. the coarse meshes are already close to the asymptotic region). Therefore, a different set of grids was used to re-calculate the observed p-value for the small flow cases as follows:

- 1/2 Scale Case 003-043 sec and 1/2 Scale Case 006-082 sec – The new observed p-value was calculated from the (coarse, intermediate, fine) meshes.
- 1/1 Scale Case 006-082 sec – The new observed p-value was calculated from the additional (coarse, normal, fine) meshes. The 'additional coarse' mesh has a cell size equivalent to the 'coarse meshes' for 1/2 Scale Case 003-043 sec and 1/2 Scale Case 006-092 sec.
- 1/1 Scale Case 003-043 sec – Unlike the other small flow cases, this case had a large observed p-value which was significantly higher than expected. The p-value was re-evaluated similar to the large flow cases from the (intermediate, normal, fine) meshes (Figure A5-5, Table A5-1 (b)-2).

The re-calculated observed p-values are approximately equivalent to the existing p-values (Table A5-1 (b)-1), which proves that the existing grid set is within or very close to the asymptotic region.

Additionally, this asymptotic behavior is illustrated quantitatively in Appendix K.

Consequently, the adequacy of grid convergence of the existing 'normal mesh' and 'fine mesh' is confirmed to be within or very close to the asymptotic region.

Note that all observed p-values are more than [ ], so assuming [ ] should be considered a conservative evaluation.

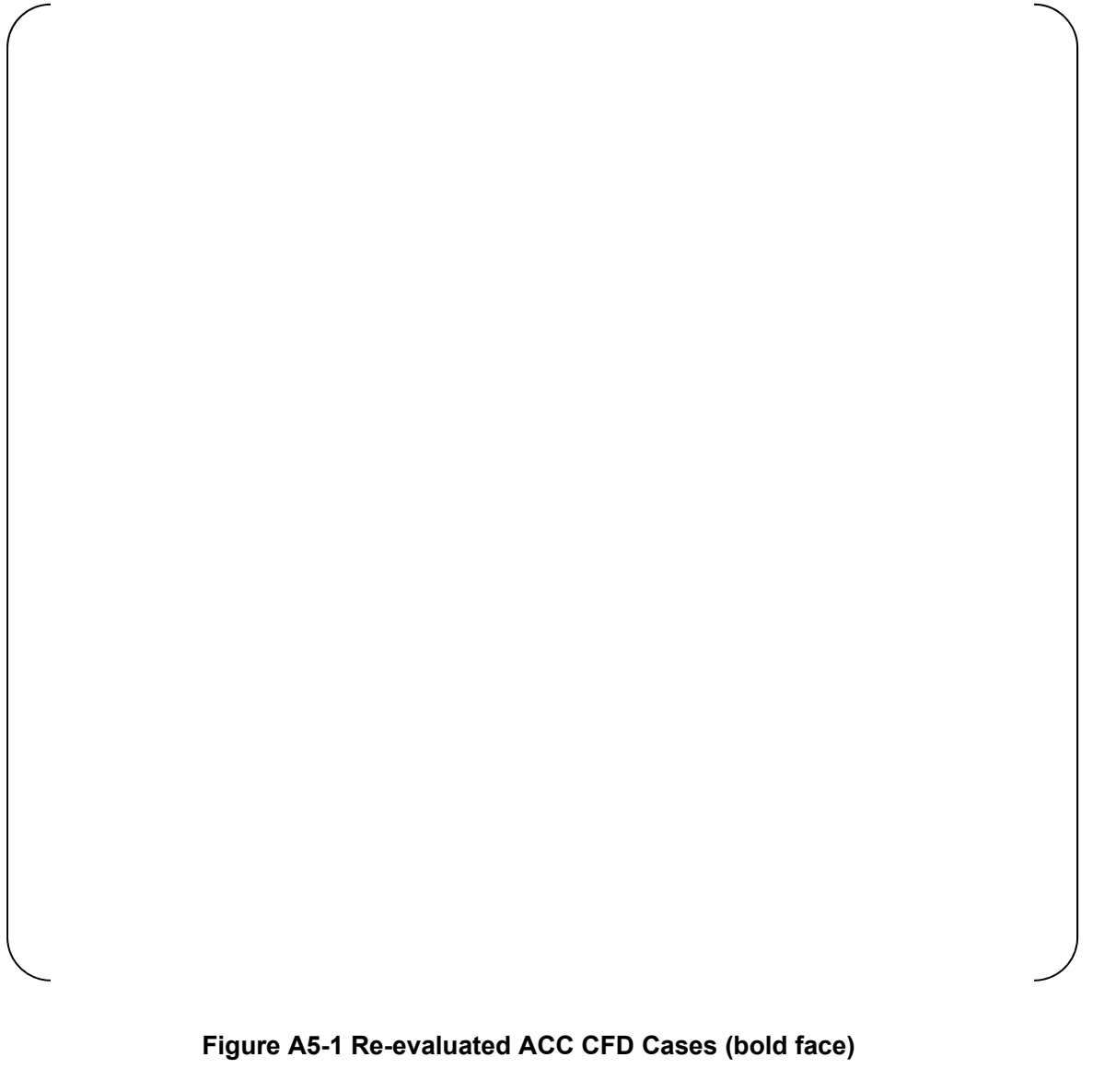


**Figure A5-1 Re-evaluated ACC CFD Cases (bold face)**



**Figure A5-2 Confirmation of Grid Convergence  
with Additional Intermediate Mesh**

**(a) Large Flow Condition Cases**  
For large observed p-values

**(b) Small Flow Condition Cases**  
**(b)-1. For approximately grid converged p-values**

**(b)-2. For large observed p-value\***

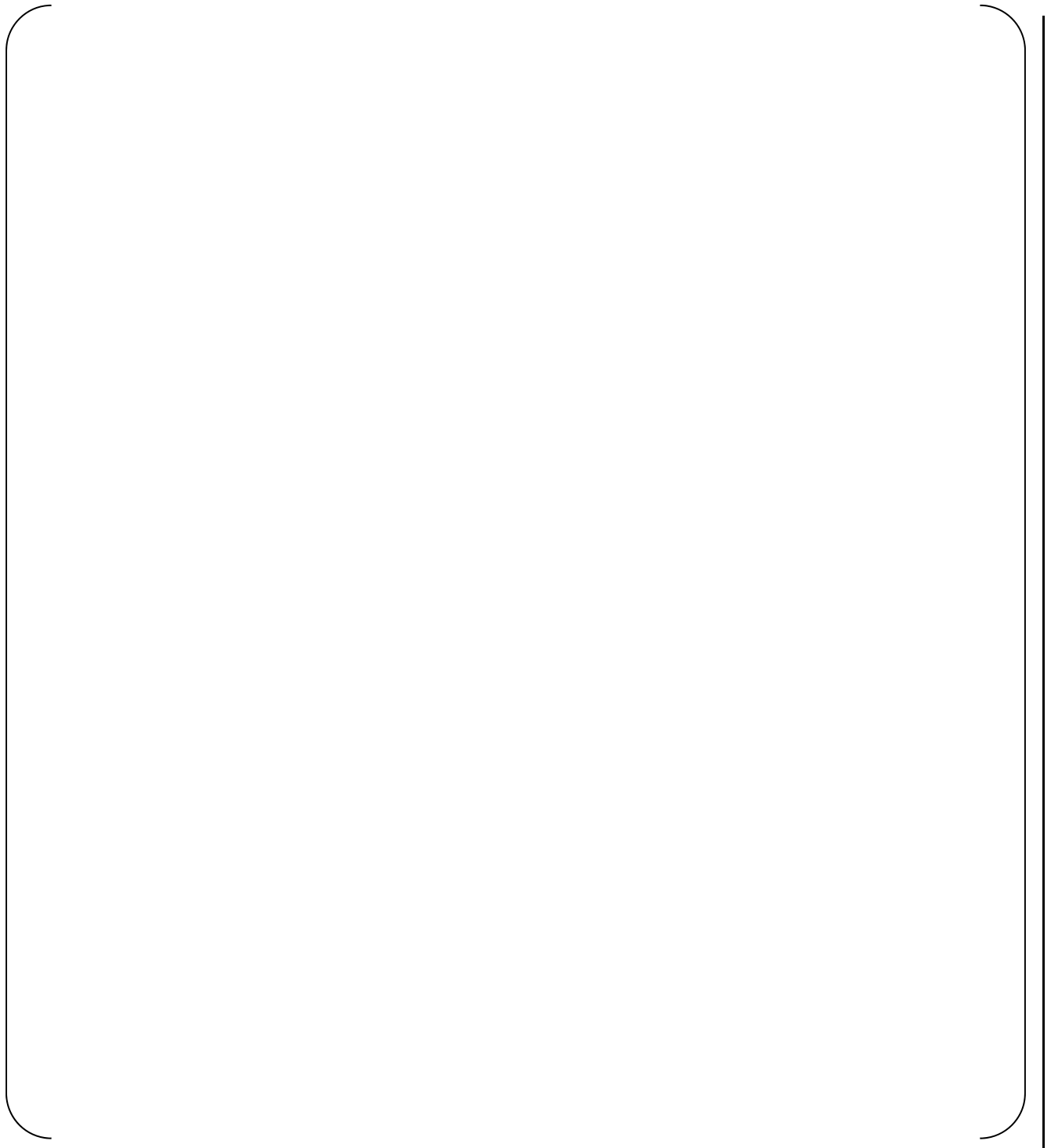


**Figure A5-3 Grid Convergence Trend for Large Flow (Re-Evaluated)  
for Large Observed p-value Cases**

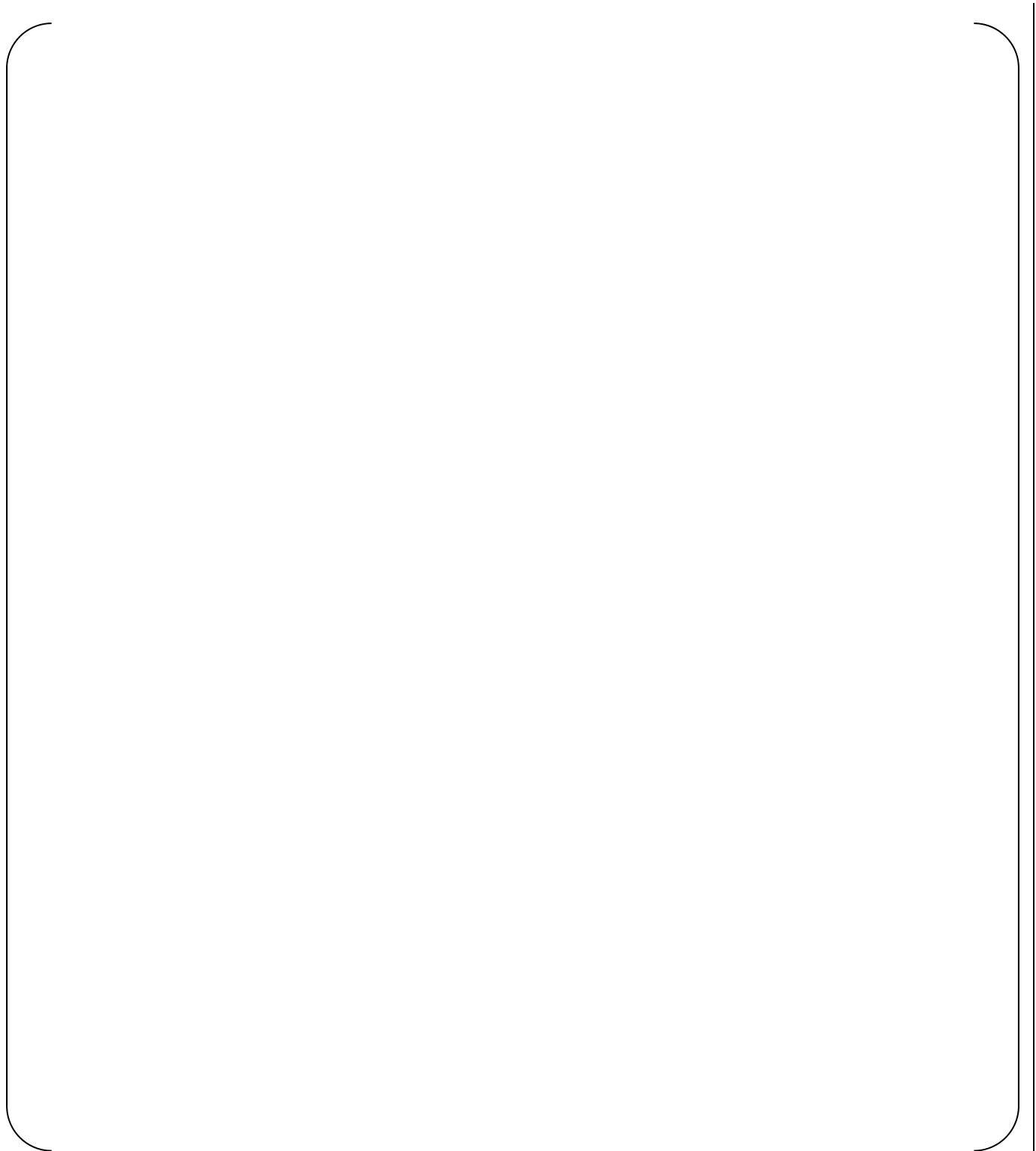


**Figure A5-4 Grid Convergence Trend for Small Flow (Re-Evaluated)  
for Approximately Grid Converged p-value Cases**

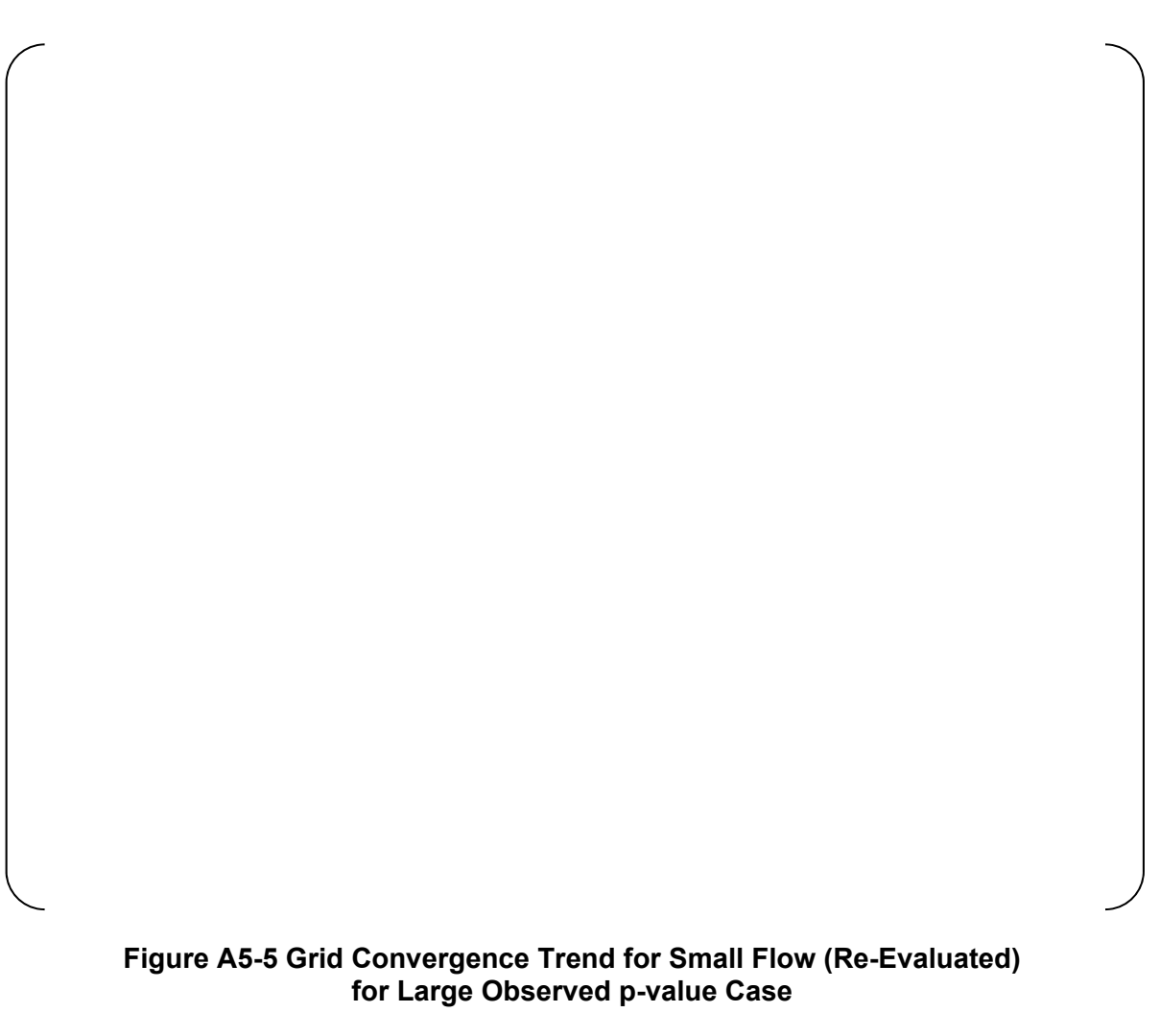


**Figure A5-5 Grid Convergence Trend for Small Flow (Re-Evaluated)  
for Large Observed p-value Case**



## (6) Modification of the GCI calculation

The uncertainty in the observed p-value affects the resultant GCI and the LOCA scaling bias. In order to exclude the uncertainty or error caused by the 'coarse mesh' result, MHI employed the following modified but more conservative methodology to calculate GCI.

### **Modified Methodology:**

Roache describes GCI with two grid solutions in Reference 20 on the basis that the solutions are within the asymptotic region and p-value is assumed '2.0' which is an expected order of accuracy, and  $F_s$  is set to '3.0'. MHI proposes to use the expected p value of '1.5' and  $F_s$  of '3.0' in calculating the GCI with the 'normal' and 'fine' meshes. The 'normal' and 'fine' meshes were confirmed to be approximately within the asymptotic region and the p-value of '1.5' was verified to be conservative as shown in section (5) of this appendix. This method results in a larger GCI and can exclude the uncertainty due to the 'coarse' and 'intermediate' meshes, which increases the observed p-value from the grid refinement.

Re-evaluated GCIs using the 'Modified Methodology' are shown in Table A6-1.

For further comparison, an evaluation using bounding GCI values is calculated where the most conservative values from ASME V&V 20 are employed (i.e. p-value of [ ] and [ ], without a consideration of grid convergence characteristics). The results of this calculation are shown in Appendix L.

**Table A6-1 Re-Evaluated GCIs by Modified Methodology**  
**U sing p=1.5 and Fs=3.0**

**(a) Calculation Procedure of GCI for 1/1 Scale Model CFD**  
**(  $\phi$  = Flow Rate Coefficient Cv)**

**(b) Calculation Procedure of GCI for 1/2 Scale Model CFD**  
**(  $\phi$  = Flow Rate Coefficient Cv)**

## (7) Conclusion

This appendix describes the validity of the current grid refinement scheme for the evaluation of the scaling effect on the advanced accumulator flow rate characteristics. It also assesses the adequacy of the grid refinement scheme based on the requirements specified in ASME V&V20 (Ref. 8), and also describes a more conservative approach to evaluate the GCIs.

The grid refinement scheme generally conforms to the systematic approach required in the standard, although some deviations can be found in the current grid refinement scheme. Nevertheless, the spatial mesh resolution of the current 'fine mesh' is fine enough to have numerically well converged solutions and no significant influence on grid convergence trends can be found due to the procedural deviations which were made.

The main reason for the large observed p-values is the fact that the current 'coarse mesh' is outside the asymptotic region of mesh convergence. This inadequately-converged solution makes the observed p-value unrealistically large even if the spatial mesh resolution of the 'normal mesh' and 'fine mesh' are sufficiently refined to resolve the flow field under consideration.

Calculations with additional meshes were performed for eight representative cases to confirm that the 'normal' and 'fine' mesh results are within or very close to the asymptotic region. The results indicated that the solutions with an additional mesh were very close to the grid convergence curve derived from 'normal mesh' and 'fine mesh' and an assumed p-value of [ ]. This indicates that the solutions of 'normal mesh' and 'fine mesh' are within or very close to the asymptotic region. From a quantitative standpoint, the new observed p-values using the additional mesh are very close to the expected p-value of [ ].

This calculation result means that GCI increases from lowering the observed p-value. In order to exclude the uncertainty or error caused by the 'coarse mesh' result, MHI employed a modified but more conservative methodology of determining the GCI. That is GCI is re-calculated using the existing 'normal' and 'fine' mesh results using a conservative p-value of [ ], and [ ]. This modified approach is reasonable and conservative for estimating the overall scale uncertainties for ACC performance.

The CFD-evaluated scale effect is calculated by applying these re-evaluated GCIs as shown in the Section 3.5.3 'Evaluation of Scale Effect between 1/2 and 1/1 scale'.

## Appendix-B

### Scale-up Capability of Turbulence Model

The purpose of Appendix-B is to show that the generalized turbulence model applied to this CFD analysis can be used to evaluate the scaling effect. First, the general Reynold's Stress Model (RSM) and its ability to scale-up is discussed. Next, the methodology and basis for tuning the RSM model to better predict the specific flow fields for the ACC are described. Finally, the results of sensitivity calculations performed with the tuned RSM model are presented to demonstrate that the CFD-Evaluated Scale Effect calculated with the generalized RSM model is suitable.

#### B-1. Introduction

The small flow results described in the body of this report demonstrate a larger amount of deviation from the observed test results than that of the large flow results. Although the CFD-Evaluated Scale Effect is a differential calculation, this appendix evaluates the impact of the (absolute) deviation from the observed test results.

The important physical process models applied in this CFD simulation are the cavitation model and the turbulence model. The present calculation simulates high speed U-shaped flow and flow through an outlet nozzle under large flow conditions, and simulates strong swirling flow under small flow conditions. The difference in  $C_v$  between the CFD result and test data is about [ ] under large flow conditions which is within the test instrument error and considered acceptable as discussed in Appendix-J.

For small flow, the comparison error is about [ ]. Cavitation does not occur under small flow conditions analyzed in the body of this report. Thus, the cavitation model is not the source of this comparison error. The  $C_v$  approaches an asymptotic numerical value as the grid is refined. The current mesh structure is fine enough to provide numerically accurate simulation results (See Appendix-A).  $Y^+$  in the current calculation grid is less than 300 as shown in Appendix-G, as the grid point near the wall should be located within the log-law layer. Thus it is believed that the effect of the boundary layer can be adequately evaluated under the current grid configuration.

These relatively large distortions under the small flow conditions are mainly caused by the RSM turbulence model (discussed in Item 3 below), which has been applied to predict the strong swirling flow inside the vortex chamber. The CFD simulation predicts smaller  $C_v$  under the small flow conditions. The current CFD model tends to predict stronger swirling/vortex in the Vortex Chamber than in the experimental test result.

The Navier-Stokes equation is the governing equation that represents fluid behavior. Reynolds stress can be obtained by applying “Reynolds averaging” to the Navier-Stokes equation (RANS). However, these simplified methods are typically not recommended for three-dimensional or swirling flows with large directional changes. The ACC CFD analysis uses the Reynolds Stress Model (RSM) turbulence model which describes the Reynolds stress with the transport equation. RSM consists of a pressure-strain correlation term, diffusion term, and viscous dissipation term in the transport equation for Reynolds stress. Constants in these models and correlations have been optimized by using a wide variety of experimental data for fundamental turbulent flow and DNS (direct numerical simulation) databases. For this reason, RSM error should be independent of scale.

The RSM model error is independent of scale for the same type of flow. The model error is due to the type of flow (specific ACC application of swirling flow versus a generalized “one-size-fits-all” RSM model) and not the scale of the flow. Therefore, the model error from the RSM model should be the same for 1/2 scale and 1/1 scale. For these complex phenomena, especially for strong swirling flow under the small flow mode, the absolute accuracy of the CFD is reduced. However, the RSM applied here is based on the governing equation of fluid flow and its applicability has been verified for a wide range of flow conditions. The model is sufficiently applicable to evaluate degrees of sensitivity between two cases as is done for the evaluation of the scale effect.

The difference between the experimental test results and CFD results in the current CFD model (in the body of this report) for small flow are expected to be due to the application of the generalized RSM model to the specific strong swirling flow in the ACC. This error is not expected to significantly affect the CFD-Evaluated Scale Effect calculated between scales.

## B-2 Turbulent Model Tuning to Lessen Model Error

Compared to the test data, CFD simulation predicts an approximately [ ] smaller flow rate coefficient  $C_v$  under the small flow conditions. This model error is larger than the uncertainty of the test data. The characteristic of small flow is the strong swirl flow in the vortex chamber and it is well-known that the standard turbulent model cannot predict the flow characteristics, especially the velocity distribution. This section describes the methodology for tuning the turbulent model to reduce the absolute model error for the ACC flow field.

### B-2-1 General Methodology

Under small flow conditions, the  $C_v$  value obtained from the CFD calculation was [ ] smaller than the  $C_v$  value obtained from the experiment. Therefore, CFD overestimates the flow resistance. Flow resistance under the small flow condition is dominated by the strong swirl flow in the vortex chamber. This suggests that the CFD overestimates the strength of the swirl flow in the vortex chamber. The model error of CFD is causally-related to this overestimation.

The characteristics of the turbulence in the swirling flow are anisotropic in nature. For this reason, the Reynolds Stress Model (RSM), which can independently solve for and evaluate the anisotropic flows, is most suitable for simulating the swirl flow. Therefore, RSM is applied to this calculation.

In the RSM, the rigorous Reynolds stress equations generated by applying the Reynolds decomposition ( $u = \bar{u} + u'$ ,  $\bar{u}$ : time average velocity component,  $u'$ : fluctuating velocity component) to the velocity in the Navier-Stokes equations and applying the ensemble average to this equation are solved. In the default RSM model, coefficients in the modeled Reynolds stress equations have been tuned based on experimental data. The RSM has a dissipation rate,  $\varepsilon$  which is the unknown variable, and an equation relating to  $\varepsilon$  is required for solving the equation system. Therefore in the turbulent model, the transport equation for  $\varepsilon$ , which is derived from the transport equation of turbulent kinetic energy,  $k$ , by multiplying both sides of the  $k$ -equation by  $(\varepsilon/k)$ , is used for closing the equation system as shown below.

$$\frac{\partial(\rho\varepsilon)}{\partial t} + \frac{\partial}{\partial x_i}(\rho\varepsilon u_i) = \frac{\partial}{\partial x_i} \left[ \left( \mu + \frac{\mu_t}{\sigma_\varepsilon} \right) \frac{\partial \varepsilon}{\partial x_i} \right] + C_{\varepsilon 1} \frac{1}{2} [P_{ii} + C_{\varepsilon 3} G_{ii}] \frac{\varepsilon}{k} - C_{\varepsilon 2} \rho \frac{\varepsilon^2}{k} + S_\varepsilon$$

The RSM uses this  $\varepsilon$  transport equation. But as previously explained, the  $\varepsilon$  equation is not derived from the physical model. For this reason, the coefficients included in this equation ( $C_{\varepsilon 1}, C_{\varepsilon 2}$ ) are the parameters which could be tuned to optimize the equation system for a specific type of flow. It is recommended that these coefficients should be set for predicting the intended experiment datum. In Reference B-1) and B-2), a similar definition can be

shown. It is clear that tuning for a specific flow field has been applied widely and many researchers have performed tuning of the  $\varepsilon$  equation as shown in Table B2-1.

**Table B2-1 Examples of Tuning the  $\varepsilon$  Equation** (Ref. B-3))

Model	$C_\varepsilon$	$C_{\varepsilon 1}$	$C_{\varepsilon 2} f_2$	Additional term	$C_{\varepsilon 3}$
Hanjalić & Launder (1976)	**1 0.15	$C_{\varepsilon 2} - 3.5C_\varepsilon$	$1.8[1 - \frac{0.4}{1.8} \exp\{-(R_t/6)^2\}]$	$4.0C_{\varepsilon 3} \nu \frac{(\overline{uv})^2}{\varepsilon} (\overline{U}_{xy})^2$	2.0
Prud'homme & Elghobashi (1983)	**2 $0.15f_\mu$	1.45	$1.9[1 - 0.263 \exp(-R_t^2/36)]$	$2\nu \frac{k}{\varepsilon} f_\mu \overline{v^2} (\overline{U}_{xy})^2$	
Kebede et al. (1985)	0.18	**3 $1.45(1 - f_s) + 2.0f_s$	1.9	$C_{\varepsilon 3} \nu \frac{k}{\varepsilon} \overline{v^2} (\overline{U}_{xy})^2$	0.3
Shima (1988)	0.15	**4 $1.35(1 + f_w)$	1.8	**5 $\xi$	
Launder & Shima (1989)	0.18	**6 $1.45 + \psi_1 + \psi_2$	1.9	No additional term	
Lai & So (1990)	0.15	**7 $1.35(1 + \sigma f'_w)$	$1.8[1 - \frac{2}{9} \exp\{-(R_t/6)^2\}]$	**8 $\xi'$	
Shih (1990)	0.07	$1.05 \frac{\xi}{\varepsilon}$	**9 $\psi_0/2$	$C_{\varepsilon 3} \nu \frac{k}{\varepsilon} \overline{v^2} (\overline{U}_{xy})^2$	$0.3(1 - F)$
Launder & Tselepidakis (1992)	0.18	1.0	$\frac{1.92}{1 + 0.63[F(-8II)]^{0.5}}$	$2C_{\varepsilon 3} \nu (k/\varepsilon) \overline{v^2} (\overline{U}_{xy})^2 + (0.92 \times 2\nu \frac{\xi}{k} k_{xy})_{xy}$	0.43

An example of tuning the normal RSM in Fluent performed by Laundar, Reece, and Rodi<sup>(Ref B-4)</sup> is shown in Figure B2-1. This example shows the calculation result of the swirl flow in the rotating pipe around the pipe axis and a comparison between the calculated results and the experimental data. N represents the ratio between the axial velocity and the rotating velocity and increasing N implies a stronger swirl. The flow distribution shape changes as the swirl flow becomes stronger. The RSM can represent the overall behavior (i.e., general shape) of the change in velocity distribution. However, the deviation between the measured results and the calculation results becomes larger as the swirling becomes stronger. That is, RSM accurately predicts general trends for swirling turbulent flow and would be suitable for a differential analysis. However, the (absolute) deviation between the experimental data and calculation results becomes larger for stronger swirling flow.

There is a study by Prof. Shima<sup>(B-6))</sup> for developing the RSM which can be applied to flow with a strong anisotropic nature. In this study,  $C_{\varepsilon 2}$  was kept constant because the tuning of  $C_{\varepsilon 2}$  performed by Lumley did not generate good results. However, by tuning the  $C_{\varepsilon 1}$  coefficient, the velocity distribution of the swirling flow could be predicted adequately.

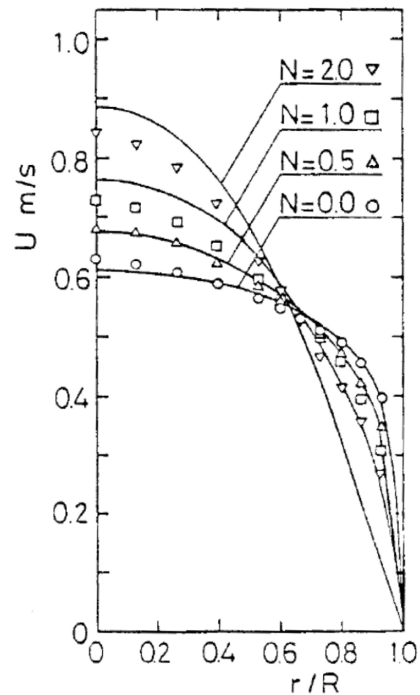


**Figure B2-1 Axial Velocity Distribution of the Swirling Flow**  
in the Rotating Pipe around the Pipe Axis (Ref. B-5))

By tuning  $C_{\varepsilon 1}$ , which can be adjusted in Fluent, the velocity distribution of the swirling flow can be adjusted to better match the observed Cv value from 1/2 scale testing. MHI determined that changing the default value of  $C_{\varepsilon 1} = 1.44$  to [ ] sufficiently reduced the deviation from the test values over the range of cases analyzed. Although the coefficient of the equation can be tuned for this target flow field (swirling flow in vortex chamber), the tuned value of the coefficient should not be applied to the general-purpose turbulent model for other types of flow since this tuning is a limited adjustment for the specific ACC small flow conditions.

To validate the tuned  $C_{\varepsilon 1}$  value, additional calculations were performed for comparison to the 1/2 scale small flow experimental test data.

- a) To address any dependency on velocity, two calculation cases each were performed with the tuned  $C_{\varepsilon 1}$  value for both high velocity conditions and low velocity conditions (four total). Comparing the Cv value between the calculation and the experiment, the difference between the calculation and experiment decreases and falls within the experimental uncertainty.
- b) Qualitatively, the velocity and pressure distribution patterns were reviewed for general consistency with the results expected from the general RSM model.



As discussed above, the model error between the CFD result and the experimental result falls within the experimental uncertainty range by applying this tuning.

### **B-3 RSM Model Tuning for ACC**

The overlap between test results and calculation results for flow rate coefficient are plotted in Figures B3-1 and B3-2. For large flow CFD results, the calculated  $C_v$  values are plotted within the measurement error bar. Detailed comparisons are shown in Appendix-J.

With the current empirical constants in the RSM model, the magnitude of the comparison error (i.e. the difference between the test value and the calculated value) in the  $C_v$  value is large and outside the range of instrument uncertainty for the small flow condition. To reduce the comparison error in the small flow condition to within instrument uncertainty, the RSM model coefficients are adjusted.

This section discusses the specific methodology for RSM tuning for the ACC, validates the tuning by comparing to the 1/2 scale test data, and estimates the impact on the CFD-Evaluated Scale Effect.

**Figure B3-1 Test Results and Calculation Results for Flow Rate Coefficient  
(Large Flow Condition)**

**Figure B3-2 Test Results and Calculation Results for Flow Rate Coefficient  
(Small Flow Condition)**

### B-3-1 Methodology for ACC RSM Model Tuning

The current turbulence model tends to predict lower dissipation in the strong swirling/vortex field. As a result, increasing the turbulent viscosity is necessary. Turbulent viscosity  $\mu_t$  is given in the formula below. Hence the turbulent kinetic energy  $k$  has to be increased and/or the turbulent energy dissipation rate  $\varepsilon$  has to be decreased.

$$\mu_t = \rho C_\mu \frac{k^2}{\varepsilon} \quad \text{Eq. B3-1}$$

RSM uses two equations:

- Reynolds stress equation: Derived analytically from the Navier-Stokes equation
- Turbulent dissipation equation ( $\varepsilon$ -equation): Assumed to be similar to the general transport equation and fit to empirical data

The turbulent dissipation equation is shown below:

Transport equation for turbulent energy dissipation rate

$$\frac{\partial(\rho\varepsilon)}{\partial t} + \frac{\partial}{\partial x_i}(\rho\varepsilon u_i) = \frac{\partial}{\partial x_i} \left[ \left( \mu + \frac{\mu_t}{\sigma_\varepsilon} \right) \frac{\partial \varepsilon}{\partial x_i} \right] + C_{\varepsilon 1} \frac{1}{2} [P_{ii} + C_{\varepsilon 3} G_{ii}] \frac{\varepsilon}{k} - C_{\varepsilon 2} \rho \frac{\varepsilon^2}{k} + S_\varepsilon \quad \text{Eq. B3-2}$$

$\varepsilon$	: Turbulent energy dissipation rate	$\rho$	: Density
$t$	: Time	$k$	: Turbulent kinetic energy
$x_i$	: Coordinate	$u_i$	: Velocity
$\mu$	: Viscosity coefficient	$\mu_t$	: Turbulent viscosity coefficient
$P_{ii}$	: Stress production term	$G_{ii}$	: Buoyancy production term
$S_\varepsilon$	: User - defined source term		
$\sigma_\varepsilon = 1.0 \quad C_{\varepsilon 1} = 1.44 \quad C_{\varepsilon 2} = 1.92$			

$C_{\varepsilon 3}$  is evaluated as a function of the local flow direction relative to the gravitational vector.

The coefficients in the equation are as follows:

- Coefficient  $C_{\varepsilon 1}$ : derived from the log-law condition of Universal Velocity Profile in turbulent flow. Default value is 1.44.
- Coefficient  $C_{\varepsilon 2}$ : derived from experimental data in homogeneous isotropic turbulent flow. So, hold the value as constant. Default value is 1.92.
- Coefficient  $C_{\varepsilon 3}$ : function of the velocity component to control the gravitational effect.

As discussed in B-2, many researchers have refined the RSM coefficient by tuning  $C_{\varepsilon 1}$ , and so MHI followed the same approach to reduce the difference between the test data and CFD result. The initial and final values are given below:

--

**B-3-2 Tuning Validation (Prediction Accuracy)**

After tuning, the comparison error of the  $C_v$  value becomes smaller than the uncertainty of the test data as shown in Table B3-1 and Figure B3-3. In all cases, model tuning increases the calculated  $C_v$  values, due to the decrease in turbulent energy dissipation in the tuned model. In addition, the tuned CFD model predicts the  $C_v$  values accurately within the measurement error bands of the test data. The mean differences from the measured data, both for the tuned and untuned models, are listed in Tables B3-1 and B3-2. An important observation is that the average bias between the calculation and measured data is largely improved in the tuned model, showing that the tuned model improves accuracy over the range of analyzed test cases. After tuning, the comparison error of the  $C_v$  value becomes smaller than the uncertainty of the test data as shown in Table B3-1 and Figure B3-3.

Table B3-3 shows the flow structure before and after tuning. The velocity and pressure distribution pattern in the vortex chamber is almost the same before and after tuning. No unexpected or unnatural flow appears by tuning.

In conclusion, the tuned CFD model has sufficient capability to reproduce the measured accumulator flow over the range of small flow injection conditions, and increased accuracy compared to the original model is being demonstrated. Thus, this tuning method can be applied.

**Table B3-1 Calculation Condition and Calculation Results Before and After Tuning  
for 1/2 Scale Model Calculation**

--

**Table B3-2 Effect of Tuning on Mean Cv Comparison Error (Small Flow)**

--	--

**Table B3-3 Comparison of Flow Structure by Tuning for Small Flow Injection**

### Figure B3-3 Effect of Tuning to $C_v$ - $\sigma_v$ Map (Small Flow Condition)

**B-3-3 RSM Tuning Results**

**(1) Influence on Scale Effect**

As shown in Figure B3-4, it can be confirmed that the scale effect obtained by the tuned turbulent model is almost the same as the scale effect obtained by the general model (before tuning).

**Table B3-4 Calculation Condition and Calculation Results Before and After Tuning for Scale Effect**



**Figure B3-4 Scale Effect for Cv by Tuning**

The sensitivity calculation cases analyzed include both the high and low velocity conditions over the range of test cases analyzed. Tuning of the RSM model results in a [ ] difference in the absolute value of Cv. However, as previously discussed, the CFD-Evaluated Scale Effect is a differential comparison of Cv values between scales. As Table B3-4 shows, the sensitivity study of the CFD model before and after tuning demonstrates that the impact on scale effect is significantly less.

## (2) Influence on Boundary Condition

In Appendix-D, it has been confirmed that the difference in the results using flow rate boundary versus using pressure boundary at the inlet is not significant in the untuned RSM model. In addition, boundary condition sensitivity calculations using the tuned CFD model are performed. The calculation results are shown in Tables B3-5 and B3-6. These tables show that the difference in the applied boundary condition is negligible, similar to the conclusion using the untuned CFD model. Thus, the applicability of the flow rate boundary condition discussed in Appendix-D is confirmed for both the tuned and untuned RSM model.

However, as shown in Figure B3-3, since the tuned CFD increases the Cv value (i.e. decreases the inlet pressure) compared to the untuned CFD model, the tuned CFD model may lead to reduced the cavitation margin. The possibility of cavitation occurring during small flow for tuned CFD is discussed in Appendix-I.

### Table B3-5 Calculation Conditions of Tuned CFD

### Table B3-6 Calculation Results of Tuned CFD



**(3) Influence on GCI**

The influence of model tuning on the Grid Convergence Index (GCI) is evaluated through confirmatory calculations as follows.

The tuned GCI model is expected to be better than the GCI for the untuned model. The velocity profile in the vortex chamber is expected to become smoother through tuning by optimizing the energy dissipation in the strong swirling flow, thereby improving the grid convergence.

The expected grid convergence behavior with the tuned model is observed through the GCI results using the tuned model for the following small flow cases, which include both high and low velocity conditions:

- Case 3-43 sec, 1/2 Scale Model
- Case 3-43 sec, 1/1 Scale Model
- Case 6-82 sec, 1/2 Scale Model
- Case 6-82 sec, 1/1 Scale Model

GCI results with the tuned model are compared to the results for the untuned model in Table B3-7, and Grid Convergence trends are shown in Figures B3-5 and B3-6 which shows the results of Case 3-43 sec and Case 6-82 sec, respectively. The intermediate values for the GCI calculation for each case are shown in Table B3-8.

All calculation results indicate an improved GCI value by applying the tuned model. These results support the hypothesis about the grid convergence characteristics as discussed above, and it is concluded that the RSM model tuning provides better grid convergence in this case.

**Table B3-7 GCI Change Due to Tuning of Turbulence Model**



**Figure B3-5 Grid Convergence Trend Curve for “C<sub>v</sub>” for Case3-43 sec**

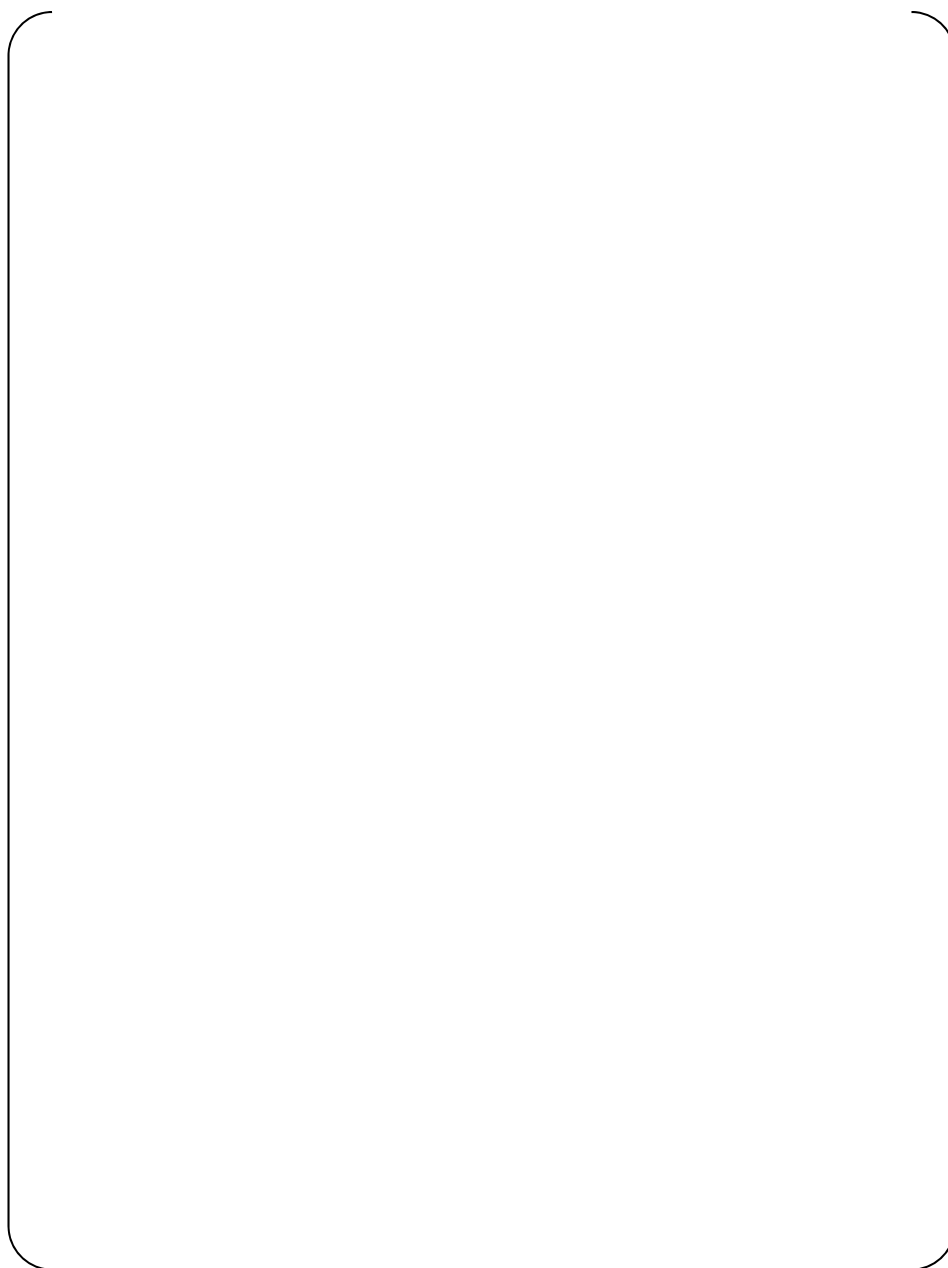


**Figure B3-6 Grid Convergence Trend Curve for “C<sub>v</sub>” for Case6-82 sec**

**Table B3-8 Calculation Procedure of GCI ( $\phi$  = Flow Rate Coefficient Cv)**

(a) High Velocity in Small Flow Condition, Case 3-43 sec



(b) Low Velocity in Small Flow Condition, Case 6-82 sec



## B-4 Conclusions

Tuning of the RSM model to reduce the deviation between the small flow CFD results and the observed 1/2 scale test data was investigated. Tuning of the RSM model for specific flow fields has been performed by many researchers, and MHI followed a similar approach

The tuning method was validated by qualitatively comparing the velocity and pressure distributions and determining that no unexpected or unnatural flow conditions resulted from tuning. Quantitatively, the comparison error was shown to decrease and fall within the uncertainty of the test data for multiple test cases over a range of high and low velocity conditions.

The results of the RSM tuning for the ACC small flow conditions confirm the following:

- The scale effect obtained by the tuned turbulent model is approximately the same as the scale effect obtained by the current model (model before tuning).
- The turbulence tuning either does not have a significant influence on GCI (i.e. Grid Convergence Trend) or decreases the GCI.
- The RSM tuning is insensitive to boundary condition type, similar to general RSM model.

Therefore, re-evaluating with the tuned RSM model would reduce the CFD-Evaluated Scale Effect, mostly through reduced numerical uncertainty due to better grid convergence characteristics. Thus, the CFD-Evaluated Scale Effect calculated from the current turbulence model (model before tuning) is acceptable for use as a conservative bounding estimate of any actual scale effects between the 1/2 scale and full scale ACC.

## B-5 References

- B-1) Durbin, P.A., Pettersson Reif, B. A., "Statistical Theory and Modeling for Turbulent Flows", Wiley, 2001.
- B-2) Pope, S.B., "Turbulent Flows", Cambridge University Press, 2000.
- B-3) Nagano etc., "Assessment of  $\epsilon$  -Equations for Wall Shear flows with DNS Database (2nd Report, The case of Second-Order Closure Modeling)", Trans. Jpn. Soc. Mech. Eng., Ser.B,59-564,(1993-8),2455.
- B-4) Launder, B.E., Reece, G.J., Rodi, W., "Progress in the Development of a Reynolds-Stress Turbulence Closure.", J. Fluid Mech., 68(3):537–566, April 1975.
- B-5) Hirai etc., "Prediction of the Laminarization Phenomena in Turbulent Swirling Flows", Trans. Jpn. Soc. Mech. Eng., Ser.B,52-476(1986-4),1608.
- B-6) Shima, "A Reynolds Stress Model Incorporating the Effect of Anisotropy (1st Report, Modeling and Application to a Flat Plate Boundary Layer", Trans. Jpn. Soc. Mech. Eng., Ser.B, 54-505(1988-9), 2317.

## Appendix-C

### Selection of Cavitation Model

#### C-1 Model Description

Fluent 12.0 provides three models for calculating the cavitation mass transfer rate, i.e., the Singhal model, Zwart-Gerber-Belamri model and Schnerr and Sauer model.

The Singhal model has been derived from the homogenous flow approach. This model solves the vapor mass fraction transport equation,

$$\frac{\partial}{\partial t}(\rho \cdot f_v) + \nabla \cdot (\rho \cdot \vec{V} \cdot f_v) = \nabla \cdot (\Gamma \nabla f_v) + R_e - R_c \quad \text{Eq. C1}$$

This model also assumes that bubble dynamics are described by the generalized Rayleigh-Plesset equation,

$$R_B \frac{D^2 R_B}{Dt^2} + \frac{3}{2} \left( \frac{DR_B}{Dt} \right)^2 = \left( \frac{P_B - P}{\rho_l} \right) - \frac{4v_l}{R_B} \dot{R}_B - \frac{2S}{\rho_l R_B} \quad \text{Eq. C2}$$

The average vapor bubble size is estimated by using

$$R_B = \frac{0.061 \cdot We \cdot \sigma^2}{2\rho_l v_{rel}^2} \quad \text{Eq. C3}$$

Rates of mass exchange are given as a function of bubble diameter and the difference between the bubble pressure and the local far-field pressure,

$$R_e = F_{vap\_SH} \frac{\max(1.0, \sqrt{k})}{\sigma} (1 - f_v - f_g) \rho_l \rho_v \sqrt{\frac{2(P_v - P)}{3\rho_l}} \quad \text{Eq. C4}$$

$$R_c = F_{cond\_SH} \frac{\max(1.0, \sqrt{k})}{\sigma} f_v \rho_l \rho_v \sqrt{\frac{2(P - P_v)}{3\rho_l}}$$

The Singhal model considers the effect of turbulence on phase change threshold pressure by correcting the vapor saturation pressure,

$$P_v = P_{sat} + \frac{1}{2} (0.39 \times \rho k) \quad \text{Eq. C5}$$

The Zwart-Gerber-Belamri model solves the vapor mass conservation equation with additional mass transfer source terms, which are related to the growth or collapse of the vapor bubbles,

$$\frac{\partial}{\partial t}(\alpha \cdot \rho_v) + \nabla \cdot (\alpha \cdot \rho_v \cdot \vec{V}_v) = R_e - R_c \quad \text{Eq. C6}$$

In this model, the mass transfer source term is calculated by using the bubble number density (n) multiplied by the mass change rate of a single bubble. The bubble number density will decrease as the vapor volume fraction increases. The mass transfer source terms in Zwart-Gerber-Belamri model are given as,

$$R_e = F_{vap\_ZGB} \frac{3\alpha_{nuc}(1-\alpha_v)}{R_B} \rho_v \sqrt{\frac{2}{3} \frac{(P_v - P)}{\rho_l}} \quad \text{Eq. C7}$$

$$R_c = F_{cond\_ZGB} \frac{3\alpha_v \rho_v}{R_B} \sqrt{\frac{2}{3} \frac{(P - P_v)}{\rho_l}}$$

The Schnerr and Sauer model follows a similar approach as that of the Singhal model to derive the expression for the net mass transfer from liquid phase to vapor phase. This model solves the vapor mass conservation equation as the following,

$$\frac{\partial}{\partial t}(\alpha \cdot \rho_v) + \nabla \cdot (\alpha \cdot \rho_v \cdot \vec{V}_v) = R = \frac{\rho_v \rho_l}{\rho} \frac{D\alpha}{Dt} \quad \text{Eq. C8}$$

The vapor volume fraction is calculated from the number of bubbles per unit volume of liquid,

$$\alpha = \frac{n_b \frac{4}{3} \pi R_B^3}{1 + n_b \frac{4}{3} \pi R_B^3} \quad \text{Eq. C9}$$

Similar to the Singhal model, the Schnerr and Sauer model also assumes that bubble dynamics are described by the generalized Rayleigh-Plesset equation. Eventually, the mass transfer source terms are given as,

$$R_e = \frac{\rho_v \rho_l}{\rho} \alpha (1 - \alpha) \frac{3}{R_B} \sqrt{\frac{2}{3} \frac{P_v - P}{\rho_l}} \quad \text{Eq. C10}$$

$$R_c = \frac{\rho_v \rho_l}{\rho} \alpha (1 - \alpha) \frac{3}{R_B} \sqrt{\frac{2}{3} \frac{P - P_v}{\rho_l}}$$

The cavitation model capabilities and application limitations in Fluent 12.0 have been summarized in Table C-1 (Ref. 3). It can be concluded from this table that any of the three cavitation models could be applied to the advanced accumulator simulation, with a compatible multiphase model and turbulence model enabled in the simulation case file.

**Table C-1 Capabilities and Limitations of Three Cavitation Models in Fluent 12.0**

	<b>Singhal Model</b>	<b>Z-G-B Model*</b>	<b>S&amp;S Model*</b>
Noncondensable Gas Effect	Considered	Not considered	Not considered
Turbulence Model Compatibility	Not compatible with the LES turbulence model	All available turbulence models in FLUENT	All available turbulence models in FLUENT
Multiphase Model Compatibility	Mixture Model	Mixture Model Eulerian Model	Mixture Model Eulerian Model
Solver Compatibility	Pressure-based solver	Pressure-based solver	Pressure-based solver
Liquid/Vapor Phase Compressibility	Incompressible or Compressible	Incompressible or Compressible	Incompressible or Compressible

\* Z-G-B Model: Zwart-Gerber-Belamri model; S&S Model: Schnerr and Sauer model

## C-2 Sensitivity Study of Cavitation Model

### 1. Selection of Cavitation Model

Table C-1 indicates that five possible combinations of cavitation model with multiphase flow model can be chosen to simulate cavitation flows, i.e.,

- (1) Singhal model with Mixture model
- (2) Zwart-Gerber-Belamri model with Mixture model
- (3) Schnerr-Sauer model with Mixture model
- (4) Zwart-Gerber-Belamri model with Eulerian model
- (5) Schnerr-Sauer model with Eulerian model

All five possible combinations have been tested for simulating the ACC flow under both the small injection rate and the large injection rate conditions. The simulation results show that:

- (i) Simulation cannot reach converged results when Eulerian model is enabled (Options 4 and 5). The Eulerian model is the most sophisticated model among three multiphase models that are provided by Fluent 12.0. The Eulerian model allows for the modeling of multiple separate, yet interacting phases. Conservation equations of mass, momentum and energy for each phase, and several interfacial momentum and thermal energy exchange constitutive equations are solved in the Eulerian



model. Although this more complex model option increases prediction precision, the Eulerian model exhibits more computational sensitivity which can result in numerical instability during the solution process. It has been observed that a coarser mesh or other model simplifications are required in order to achieve converged solutions, which reduces the overall accuracy of the simulation results.

When the Mixture model is applied, the Chimera meshing option was enabled in order to achieve the desired  $Y^+$  value near the wall (refer to 3.2.2). The simulation results show that:

- (ii) Simulations with the Schnerr-Sauer model cannot reach converged results (Option 3). In these calculation processes, the mass flow rates at the inlet and the outlet are imbalanced and the calculation terminates before convergence is achieved.
- (iii) Simulation with the Singhal model does not exhibit the aforementioned problems and results in converged, mass-balanced solutions.

Thus, the Singhal model combined with the Mixture multiphase model has been chosen in this CFD study for the ACC under both the small flow injection and the large flow injection conditions.

Furthermore, it is generally known that cavitation may occur at static pressures larger than saturation pressure due to the effect of turbulence (for example, see Reference 19). Although three cavitation models are available in Fluent 12.0, only the Singhal model can model the effect of turbulence on cavitation inception. Thus, the Singhal model is superior to the other models for modeling cavitation inception in the ACC analyses. To provide additional confirmation of whether it is appropriate to apply the Singhal model, CFD calculations have been performed in order to evaluate the sensitivity for calculating scale effects using an alternate cavitation model in Fluent 12.0.

In Appendix-I, the sensitivity calculations include a sensitivity case where the outlet boundary pressure is reduced to the atmospheric pressure. Even in this case, the flow rate coefficient is not changed although a larger amount of cavitation voiding occurs in the center of the vortex chamber and outlet nozzle, compared with the other cases. The same result was obtained for both the 1/2 scale and 1/1 scale model. Therefore, it is concluded that the small flow rate is insensitive to cavitation voiding without scaling concerns. Therefore the sensitivity analysis of cavitation model is performed for large flow injection.

## **2. Calculation conditions**

For large flow, Case 003-005 sec was analyzed for the sensitivity calculations, since cavitation is most likely to occur for this case. The “Fine” mesh with the Chimera mesh refinement has been utilized in these calculations in order to provide an adequate  $Y^+$  value (approximately 300, as recommended by the Fluent user manual). Therefore, the friction and velocity gradients at the wall are modeled with sufficient accuracy.

In the calculation with fine mesh, the calculations for the ZGB and SS models using RSM and 2<sup>nd</sup>-order upwind do not achieve convergence. In these calculation processes, the

mass flow rates at the inlet and the outlet are imbalanced and the calculation terminates before convergence is achieved. For large flow, the anisotropic turbulence modeling used in the RSM model is considered to be less important than wall modeling and cavitation inception. Therefore, the 1<sup>st</sup>-order k-omega turbulence model is used to obtain stable solutions. However the calculations for the SS model do not converge. So the sensitivity for calculating scale effects models is evaluated in Singhal model and ZGB model. In Fluent 12.0 documentation, it can be confirmed that the solution of SS and ZGB models are in good agreement in the validation calculation of orifice cavitation (Chapter 15. Figure 15.4.1, Page 15-4 in Reference 3). Thus the evaluation of the sensitivity for calculating scale effects without SS models is considered acceptable. The adequacy of using 1<sup>st</sup>-order k-omega instead of 2<sup>nd</sup>-RSM for turbulence model is discussed further below.

### 3. Results of calculations

--

**Table C-2 Calculation Conditions for Singhal and ZGB Models**

--

**Table C-3 Scale Effects using Singhal and ZGB Models for Large Flow**

--



Figure C-1 Void Fraction Distribution at the Throat (Case 3 Large Flow 5 sec, Fine Mesh)

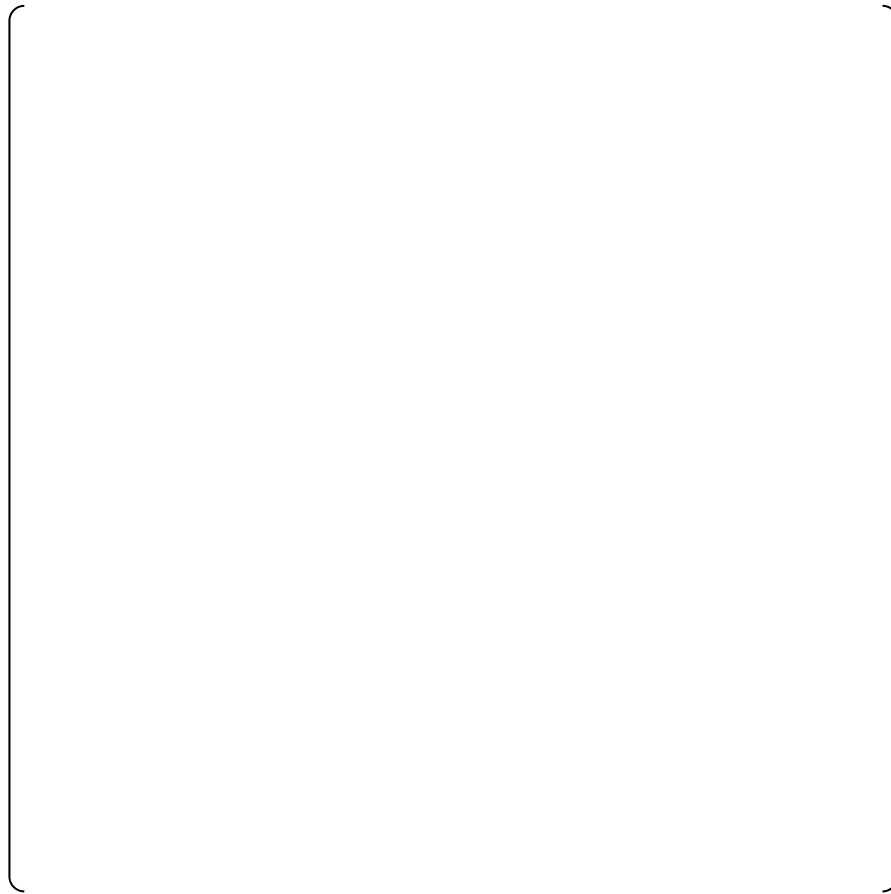


**Figure C-2 Total Pressure Loss of Vortex Chamber, Reducer and Diffuser**

### C-3 Justification of Singhal Model

#### Applicability of Singhal Model

The model author has made the following assumptions when deriving the Singhal model,

- (i). Assuming homogenous two-phase flow (Equal-Velocity-Equal-Temperature)
- (ii). Assuming that flow is isothermal with constant fluid properties
- (iii). Assuming that noncondensable gas mass fraction is constant in the flow field
- (iv). Utilizing the generalized Rayleigh-Plesset equation to describe the bubble growth process, while ignoring the viscous damping term and surface tension term
- (v). Ignoring the second-order derivative of  $R_B$
- (vi). Estimating bubble diameter based on Eq. C3
- (vii). Assuming that the phase change rate is proportional to the slip velocity between the vapor phase and liquid phase, instead of proportional to the square of slip velocity
- (viii). Assuming that characteristic velocity can be expressed as the square root of local turbulent kinetic energy  $\sqrt{k}$
- (ix). Treating the effect of turbulence on cavitation phase-change threshold pressure by using Eq. C5

All of these assumptions are acceptable for the ACC flow field based on the following reasons:

- (i). Cavitation occurs at the downstream of nozzle throat in the outlet injection pipe. At that position, liquid flow velocity is expected to be much larger than the slip velocity between vapor bubbles and liquid.
- (ii). The ACC injection process can be treated as isothermal.

Thus, the Singhal model can be applied to the ACC simulations.

#### Scaling Effect of the Singhal Model

The Singhal model solves the vapor mass conservation equation (Eq. C1), with the mass transfer rate terms as given in Eq. C4. These equations can be converted to dimensionless format if the following parameters are defined,

$$t^* = \frac{t}{t_0}, \quad \rho_v^* = \frac{\rho_v}{\rho_{v,0}}, \quad x^* = \frac{x}{L_0}, \quad u^* = \frac{u}{u_0}, \quad C_e^* = \frac{C_e}{C_{e,0}}, \quad \text{Eq. C11}$$

$$k^* = \frac{k}{k_0}, \quad \sigma^* = \frac{\sigma}{\sigma_0}, \quad \rho_l^* = \frac{\rho_l}{\rho_{l,0}}, \quad P^* = \frac{P}{\rho_{l,0} u_0^2}$$

Here, subscript 0 refers to an appropriate reference value.

Equation C1 can be re-written as,

$$\frac{\rho_{v,0}}{t_0} \frac{\partial}{\partial t^*} (\alpha \cdot \rho_v^*) + \frac{\rho_{v,0} \cdot u_0}{L_0} \nabla^* \cdot (\alpha \cdot \rho_v^* \cdot \vec{V}_v^*) = \frac{C_{e,0} \cdot \sqrt{k_0} \cdot \rho_{l,0} \cdot \rho_{v,0} \cdot u_0}{\sigma_0} (R_e^* - R_c^*) \quad \text{Eq. C12}$$

which can be re-arranged as,

$$\frac{\partial}{\partial t^*} (\alpha \cdot \rho_v^*) + \frac{t_0 \cdot u_0}{L_0} \nabla^* \cdot (\alpha \cdot \rho_v^* \cdot \vec{V}_v^*) = \frac{C_{e,0} \cdot \sqrt{k_0} \cdot \rho_{l,0} \cdot u_0 \cdot t_0}{\sigma_0} (R_e^* - R_c^*) \quad \text{Eq. C13}$$

Two dimensionless numbers appear in (Eq. 13), such as,

$$\begin{aligned} \Pi_1 &= \frac{t_0 \cdot u_0}{L_0} \\ \Pi_2 &= \frac{C_{e,0} \cdot \sqrt{k_0} \cdot \rho_{l,0} \cdot u_0 \cdot t_0}{\sigma_0} = \frac{\rho_{l,0} \cdot u_0^2 \cdot L_0}{\sigma_0} \end{aligned} \quad \text{Eq. C14}$$

$\Pi_1$  represents the ratio of transient time to the flow characteristic time.  $\Pi_2$  is similar to the Weber number, represents the ratio of inertia to surface tension force. Considering the physical meaning of dimensionless group  $\Pi_2$ , an appropriate reference value for length scale,  $L_0$ , is the bubble diameter. Eq. C13 will generate same cavitation solutions for ACC systems with different length scale, under the situation that values of  $\Pi_1$  and  $\Pi_2$  are same, and same initial condition and boundary conditions have been imposed for these ACC systems.

It is expected that typical bubbles generated in the cavitation process will be very small, i.e., their diameters will be less than a few millimeters, and the two-phase flow structure is expected to be bubbly flow. The following equation can be utilized to estimate the average bubble diameter for bubbly flow,

$$D_b = 2 \sqrt{\frac{\sigma}{g \cdot \Delta \rho}} \quad \text{Eq. C15}$$

From the Advanced Accumulator working conditions, the average bubble diameter can be estimated to be [     ] mm from the above equation. This means that the throat size of 1/2 scale ACC is much larger than a typical bubble size. Thus, the Singhal model describes a local phenomenon, which is related to the length scale of a vapor bubble. Therefore, the performance of the Singhal model will be the same for 1/2 scale ACC simulations and for 1/1 scale ACC simulations.

### Applicability of the Singhal Model to High Void Fraction Regions

Two assumptions for deriving the Singhal model are related to the low void fraction flow conditions, such as, the flow is homogenous and the generalized Rayleigh-Plesset equation can be utilized to describe the bubble growth process. However, the model also contains two empirical constants,  $C_e$  and  $C_c$ , to adjust the vapor generation and condensation rates.

$$R_e = C_e \frac{V_{ch}}{\sigma} (1-f) \rho_l \rho_v \sqrt{\frac{2}{3} \frac{(P_v - P)}{\rho_l}} \quad \text{Eq. C16}$$

$$R_c = C_c \frac{V_{ch}}{\sigma} f \rho_l \rho_v \sqrt{\frac{2}{3} \frac{(P - P_v)}{\rho_l}} \quad \text{Eq. C17}$$

These empirical constants have been decided by comparing the CFD results with various cavitation flows, including sharp-edged orifice flows and hydrofoil flows. The following validation calculations conducted by several researchers show that the Singhal model can give reasonable predictions for pressure variation and cavitation number for high-speed flow cavitation on hydrofoils and submerged cylindrical bodies. These validation calculation results contain high void fraction (up to 1.0) regions near the wall, which demonstrates that the Singhal model can be applied to a high void fraction that occurs in a small region and achieve good agreement with experimental results.

Watanabe et. al.(Ref.9) performed RANS simulations of flow around two different conventional propellers at non-cavitating and cavitating operating conditions by applying the Singhal model. Predicted values of the propeller thrust coefficients and torque coefficients in uniform flow under large angle of attack conditions are in a good agreement with the measured data. The simulation predicts that high vapor void fraction regions occur on the backside of the propeller blade. The predicted cavity shape on the blade is in good agreement with the observed cavity shapes in the experiment (Fig. 16 in Reference 9).

Huang et. al.(Ref.17) utilizes the Singhal model combined with a linear viscous turbulent method to simulate steady cavitation flow over NACA66 2-D hydrofoils. The predicted pressure distribution on the hydrofoil surface fits well with the measured data. High void fraction regions appear near the wall (Fig. 7 and Fig. 8 in Reference 17). General characteristics of the predicted cavity region fit well with experimental observations. For example, the predicted cavity length grows with the increase of the angle of attack, and with the decrease of the cavitation numbers.

Dular et. al.(Ref.18) performed an experimental and numerical study of developed cavitating flow around two hydrofoils. The PIV (Particle Image Velocimetry) and LIF (Laser Induced Fluorescence) techniques were adopted in the experiment to measure the velocity and void ratio fields around the hydrofoils. The Singhal model was applied to predict the vapor generation process. Comparisons between the numerical and experimental results show good agreement, including the distribution and size of vapor structures and velocity



fields. The distribution of pressure on the hydrofoil surface has been correctly predicted using the Singhal model.

Appendix-D

Consideration for Boundary Condition in Small Flow Injection

For small flow injection, flow rate boundary conditions are used on the water surfaces in the tank and the standpipe in order to stabilize the calculations. Therefore, the resulting pressure on the water surface obtained by analysis is not constant and has a slight difference from the measured pressure. To determine that this difference is not significant, an analysis was performed for which the water surface at the small flow inlet is specified as a pressure boundary condition. This pressure boundary condition result is consistent with the flow rate boundary condition result. It should be noted that the water surface in the standpipe is specified as a flow rate boundary condition for both analyses. Table D-1 shows the calculation conditions used in the CFD analysis, and Table D-2 shows the calculation results. Flow rate coefficients and flow structures of both the flow rate boundary condition and pressure boundary condition are consistent. Thus, difference in the applied boundary condition (flow rate or pressure) is negligible and the validity for using the flow rate boundary condition is confirmed.

Table D-1 Calculation Conditions of CFD

Table D-2 Calculation Results of CFD

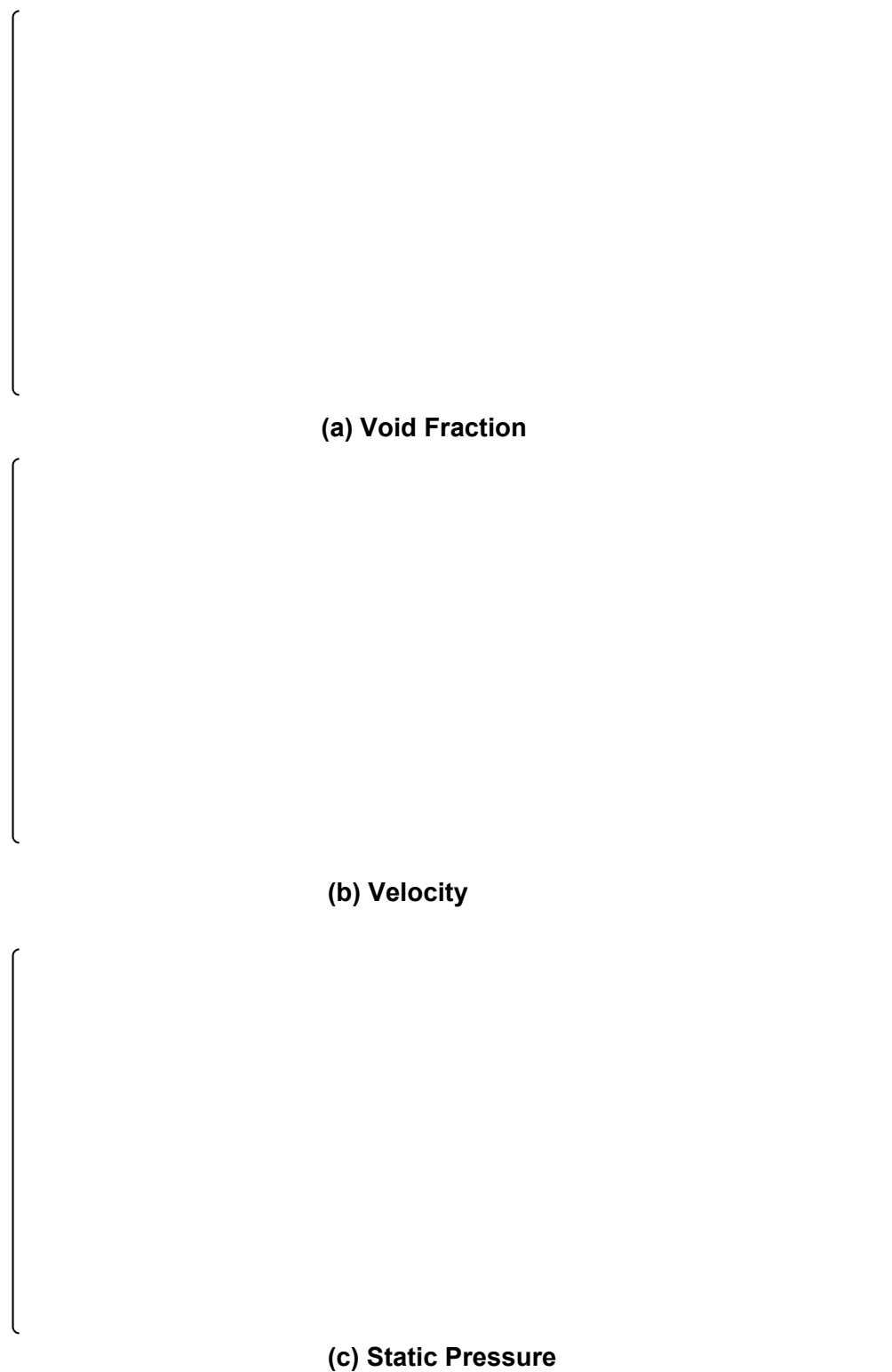


**Figure D-1 Comparison of Inlet Boundary Conditions for Small Flow Injection**

**Appendix-E****Flow Structure for Large Flow**

The body of this report includes flow structure plots of static pressure, velocity vector, and void fraction for the limiting CFD cases of interest. This appendix includes flow structure plots for the remaining CFD cases analyzed, for the large flow condition.



Figure E-1(a) Flow Structure in Vortex Chamber (Case 3 Large Flow 20 sec)





Figure E-1(b) Flow Structure in Flow Damper (Case 3 Large Flow 20 sec)



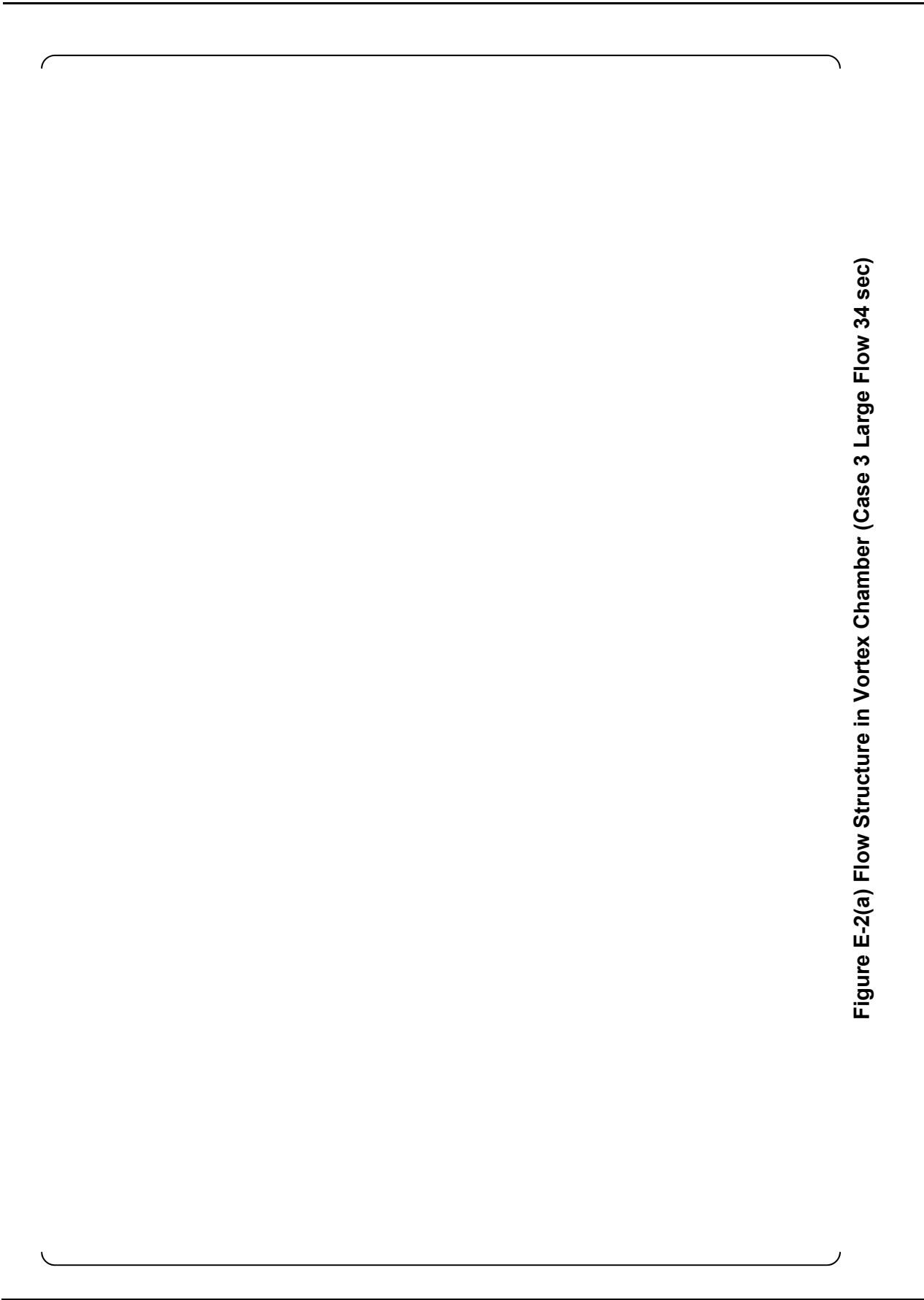


Figure E-2(a) Flow Structure in Vortex Chamber (Case 3 Large Flow 34 sec)

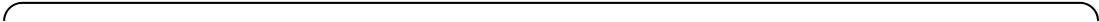


Figure E-2(b) Flow Structure in Flow Damper (Case 3 Large Flow 34 sec)







Figure E-3(a) Flow Structure in Vortex Chamber (Case 6 Large Flow 5 sec)



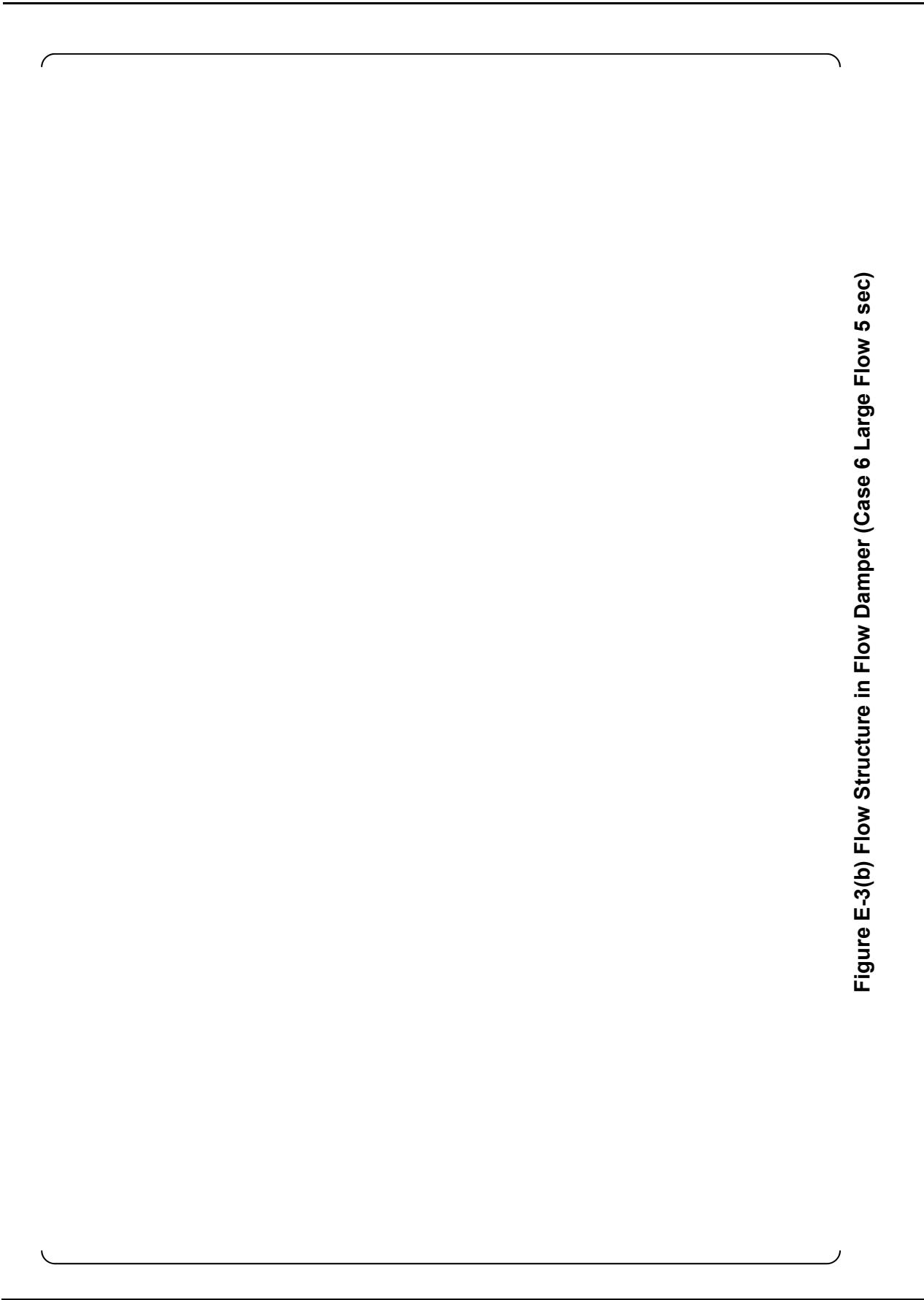


Figure E-3(b) Flow Structure in Flow Damper (Case 6 Large Flow 5 sec)

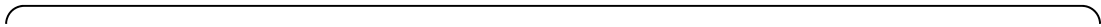


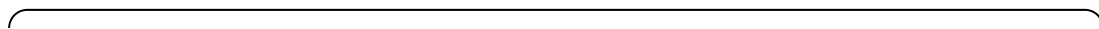
Figure E-4(a) Flow Structure in Vortex Chamber (Case 6 Large Flow 11 sec)





Figure E-4(b) Flow Structure in Flow Damper (Case 6 Large Flow 11 sec)





**Figure E-5(a) Flow Structure in Vortex Chamber (Case 6 Large Flow 20 sec)**



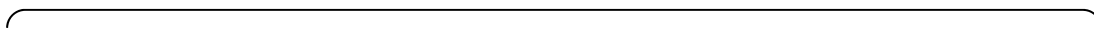


**Figure E-5(b) Flow Structure in Flow Damper (Case 6 Large Flow 20 sec)**



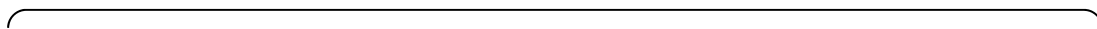


**Figure E-6(a) Flow Structure in Vortex Chamber (Case 6 Large Flow 50 sec)**



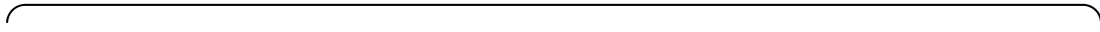
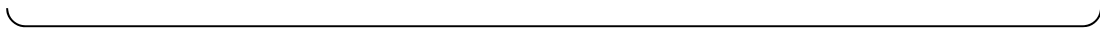


**Figure E-6(b) Flow Structure in Flow Damper (Case 6 Large Flow 50 sec)**





**Appendix-F****Flow Structure for Small Flow**

The body of this report includes flow structure plots of static pressure, velocity vector, void fraction, reverse flow region and location of maximum value of difference of absolute pressure and vapor pressure for the limiting CFD cases of interest. This appendix includes flow structure plots for the remaining CFD cases analyzed for the small flow condition.

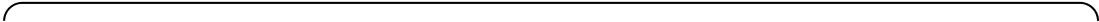


Figure F-1(a) Flow Structure in Vortex Chamber (Case 3 Small Flow 100 sec)



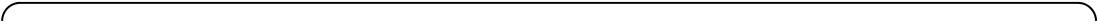


Figure F-1(b) Flow Structure in Flow Damper (Case 3 Small Flow 100 sec)



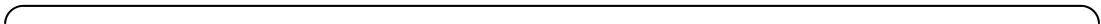


Figure F-2(a) Flow Structure in Vortex Chamber (Case 3 Small Flow 125 sec)

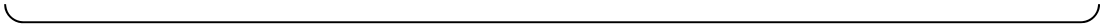
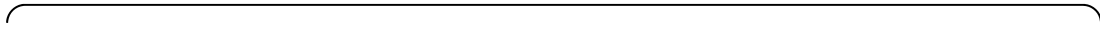




Figure F-2(b) Flow Structure in Flow Damper (Case 3 Small Flow 125 sec)





**Figure F-3(a) Flow Structure in Vortex Chamber (Case 6 Small Flow 82 sec)**



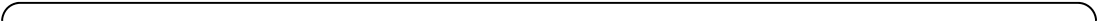
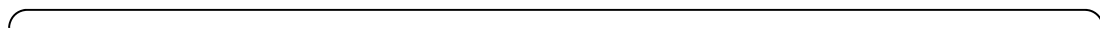


Figure F-3(b) Flow Structure in Flow Damper (Case 6 Small Flow 82 sec)





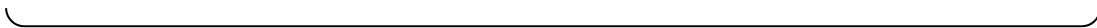
**Figure F-4(a) Flow Structure in Vortex Chamber (Case 6 Small Flow 200 sec)**







**Figure F-4(b) Flow Structure in Flow Damper (Case 6 Small Flow 200 sec)**



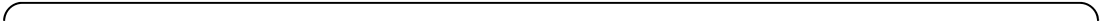
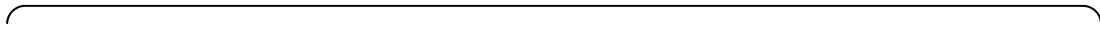


Figure F-5(a) Flow Structure in Vortex Chamber (Case 6 Small Flow 290 sec)





**Figure F-5(b) Flow Structure in Flow Damper (Case 6 Small Flow 290 sec)**



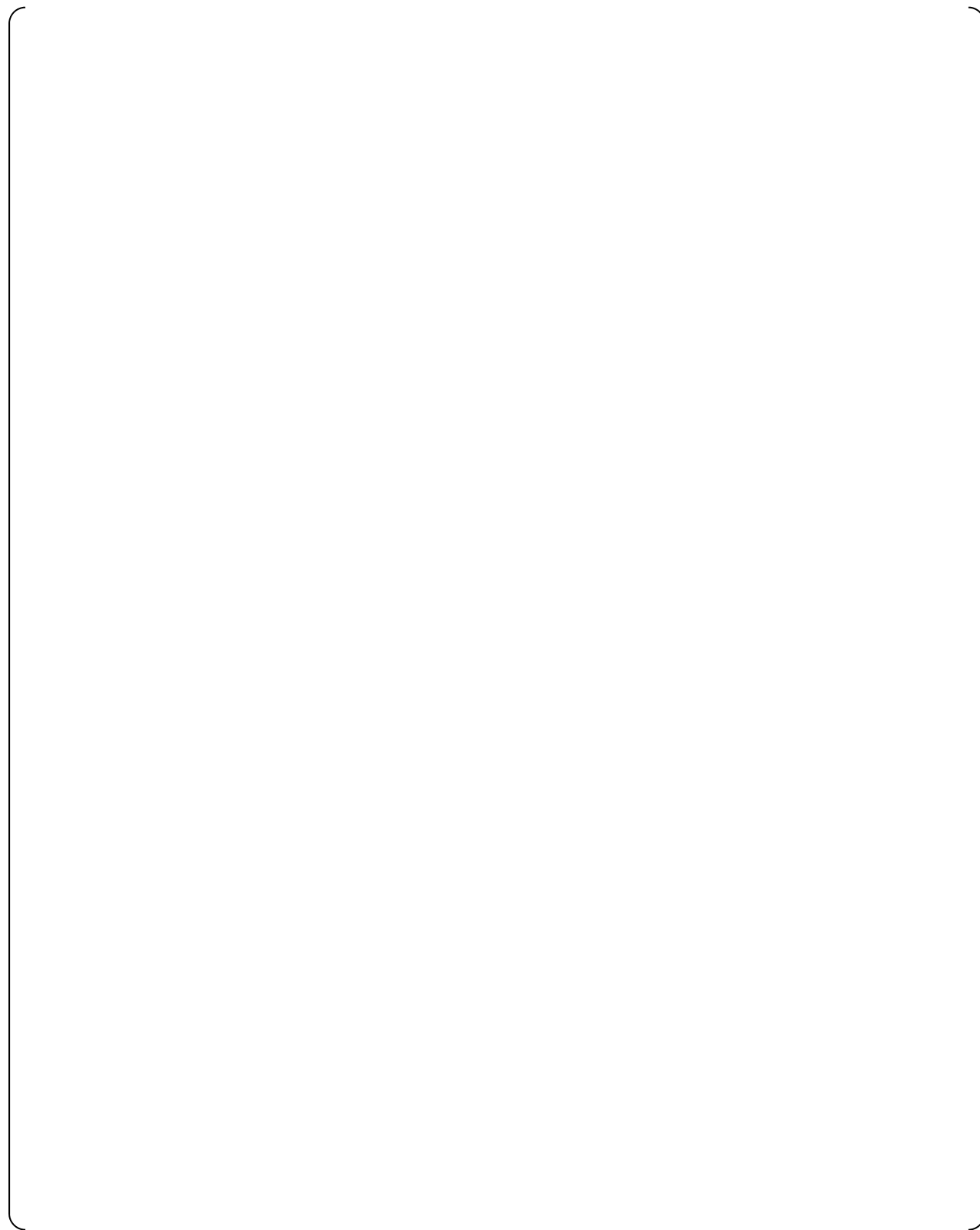


**Figure F-6(a) Reverse Flow Region (1/2 Scale, Case 3 Small Flow)**

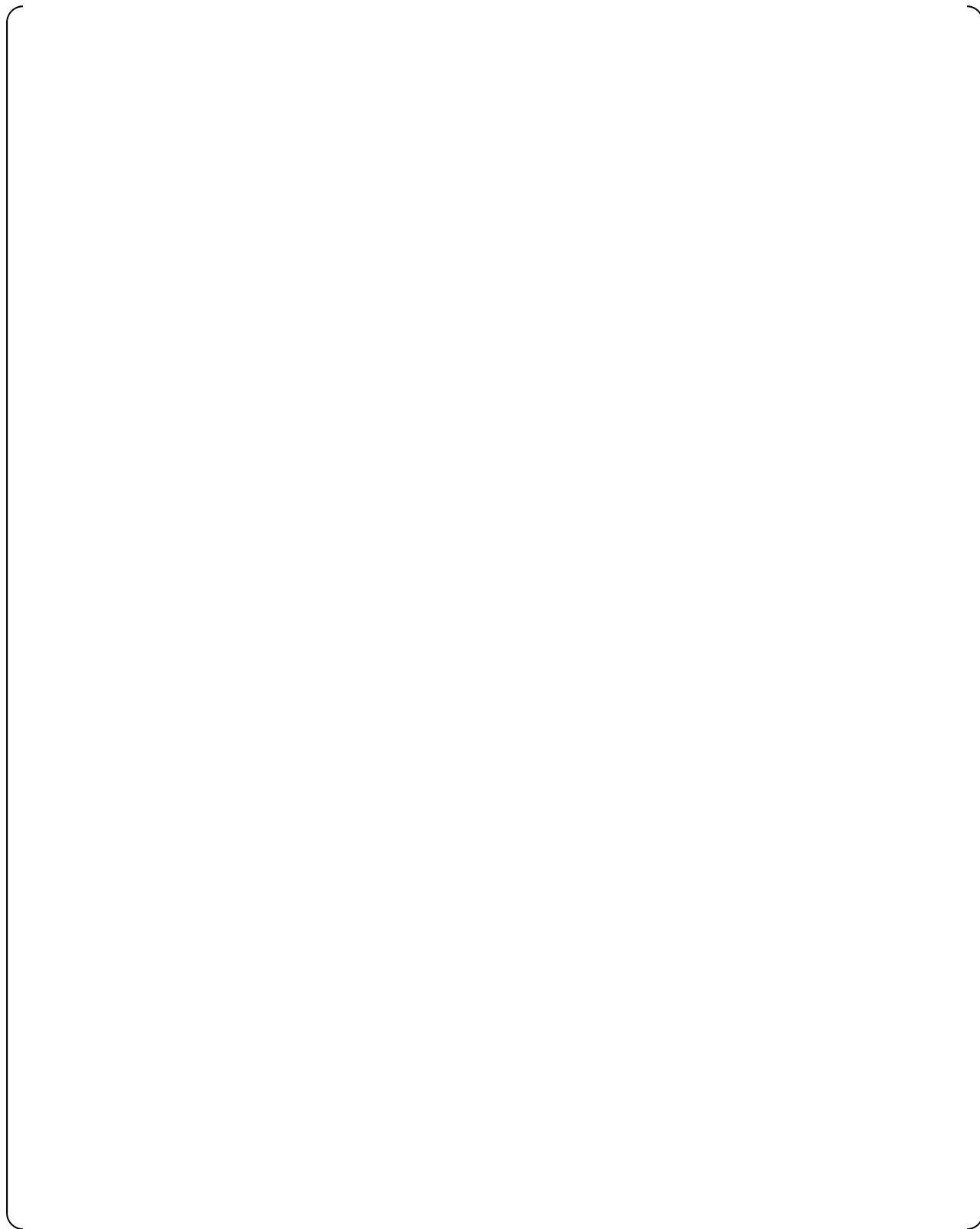


**Figure F-6(b) Reverse Flow Region (1/2 Scale, Case 6 Small Flow)**

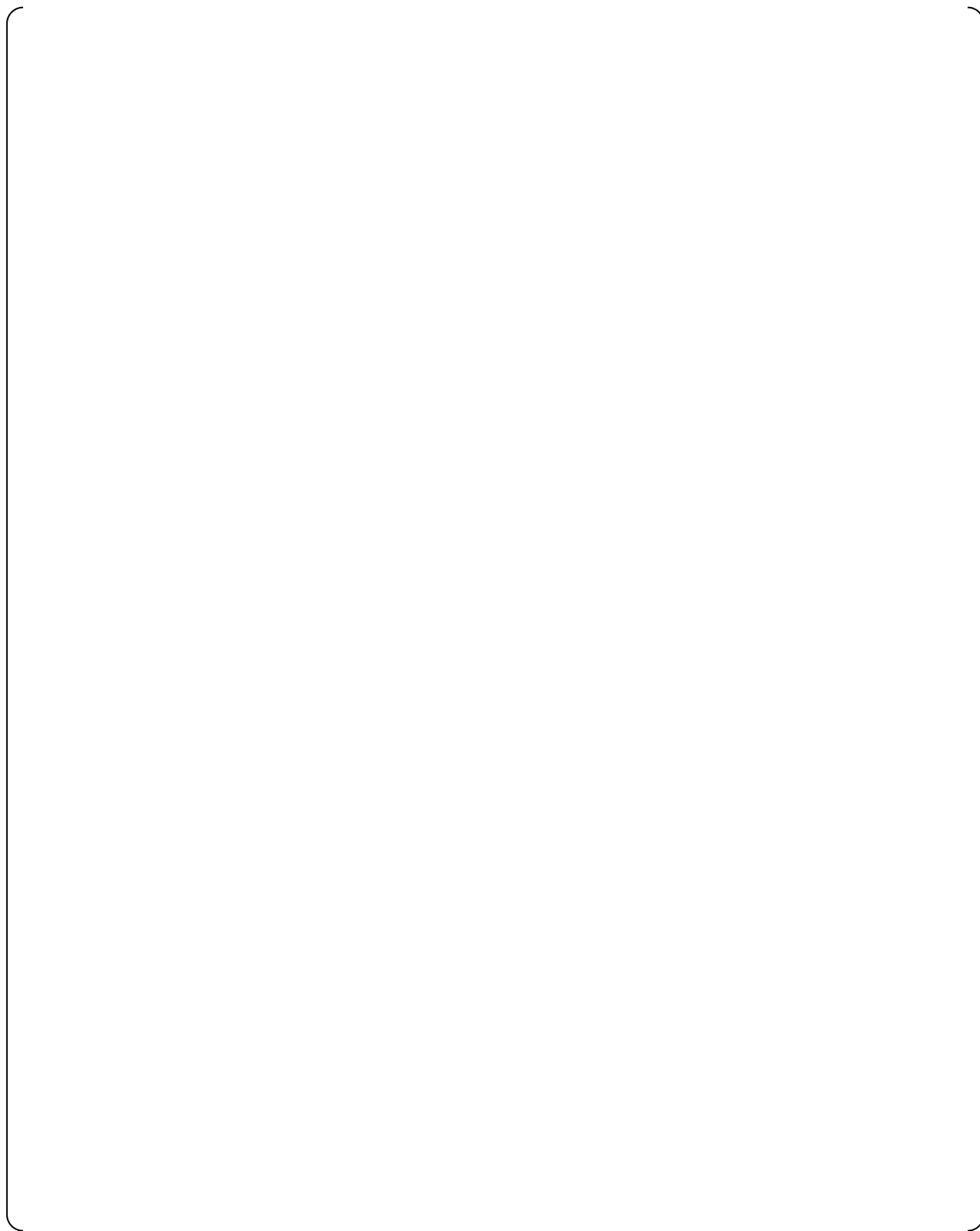


**Figure F-6(c) Reverse Flow Region (1/1 Scale, Case 3 Small Flow)**

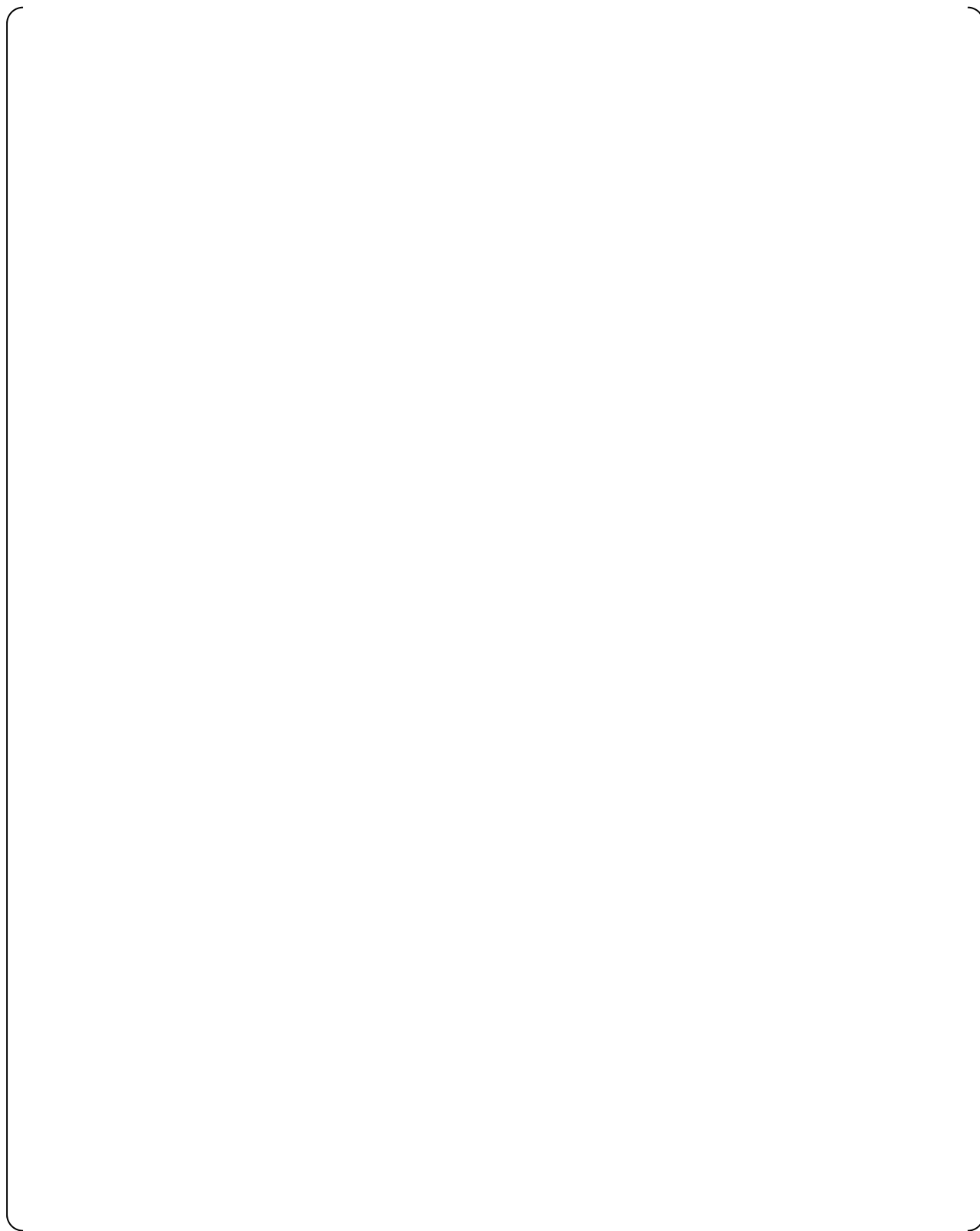


**Figure F-6(d) Reverse Flow Region (1/1 Scale, Case 6 Small Flow)**



**Figure F-7(a) Location of maximum value of Difference between Absolute Pressure and Critical Pressure of Cavitation (1/2 scale, Small Flow)**





**Figure F-7 (b) Location of maximum value of Difference between Absolute Pressure and Critical Pressure of Cavitation (1/1 scale, Small Flow)**

**Appendix-G****Y+ Profile**

Y+ of large flow injection is less than 300 at throat and diffuser where flow resistance is dominated. Thus it is confirmed that the effect of the boundary layer can be adequately evaluated under the current grid (See Figure G-1).

Y+ of small flow injection is less than 100 at the vortex chamber except around the exit where the swirl flow causes large flow resistance. This means that the effect of the boundary layer can be adequately evaluated under the current grid (See Figure G-2).

In small flow injection, Y+ of 1/1 scale model is larger than the value of the 1/2 scale model at the wall of outlet nozzle. This is caused by the difference of the cell thicknesses near the wall in both models. However the influence on flow resistance is negligible because the shear stresses are almost the same in both scale models (See Figure G-3).



**Figure G-1 Y+ Distribution of Large Flow**

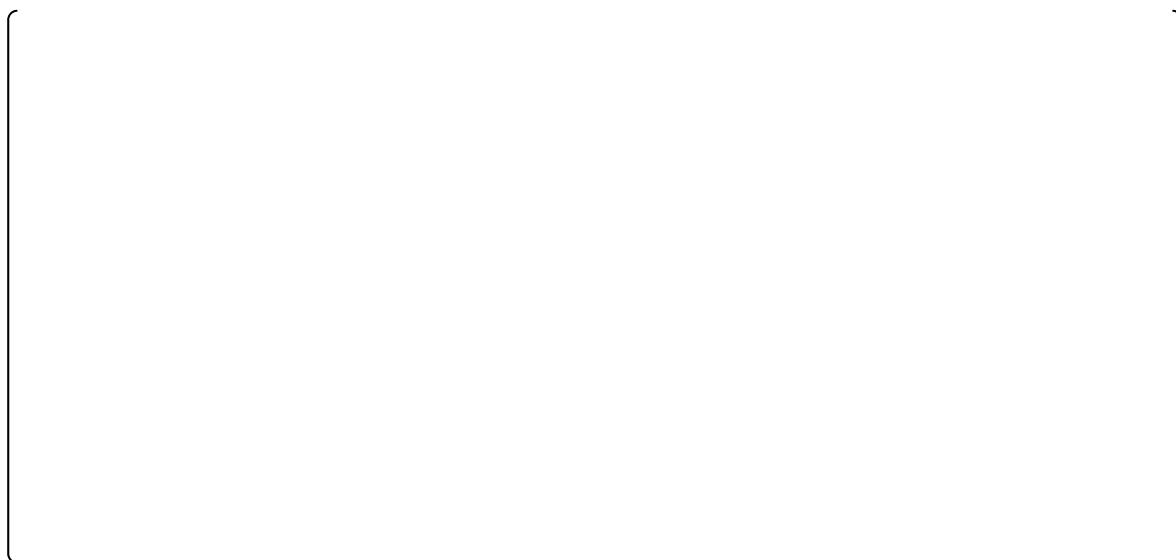


**Figure G-2 Y+ Distribution of Small Flow**



**Figure G-3 Shear Stress Distribution of Small Flow**

## Appendix-H

### Validity Evaluation of Tolerance Interval

The computational method is verified by the numerical value described in ASME PTC 19.1-2005

**Table H-1 Factors for Calculating the Two-Sided 90% and 95% Probability Intervals for a Normal Distribution (Ref.15))**

Number of Given Observations	Factors for Tolerance Interval to Contain at Least 90% and 95% of the Population	
	$C_{T,90}(n)$	$C_{T,95}(n)$
n		
4	5.37	6.37
5	4.28	5.08
6	3.71	4.41
7	3.37	4.01
8	3.14	3.73
9	2.97	3.53
10	2.84	3.38
11	2.74	3.26
12	2.66	3.16
15	2.48	2.95
20	2.31	2.75
25	2.21	2.63
30	2.14	2.55
40	2.05	2.45
60	1.96	2.33
$\infty$	1.64	1.96

$C_{T,90}(n)$  and  $C_{T,95}(n)$  are related as follows as a result of examining the numerical values above.

$$C_{T,90}(n) = C_{T,95}(n)/1.96 \times 1.645$$

$$(\text{Example. } 3.37 = C_{T,90}(7) = C_{T,95}(7)/1.96 \times 1.645 = 4.01/1.96 \times 1.645)$$

1.96 : Corresponds to 95% confidence interval in normal distribution.

1.645 : Corresponds to 90% confidence interval in normal distribution.

$C_{T,90}(n)$  and  $C_{T,95}(n)/1.96 \times 1.645$  are equated. That is, the technique described in the report is appropriate to derive a 95% confidence interval from a limited sample.

## **Appendix-I**

### **Effect of Cavitation on Small Flow Hydraulic Performance**





**Figure I-1(a) Flow Structure in Vortex Chamber (at mid-height)**



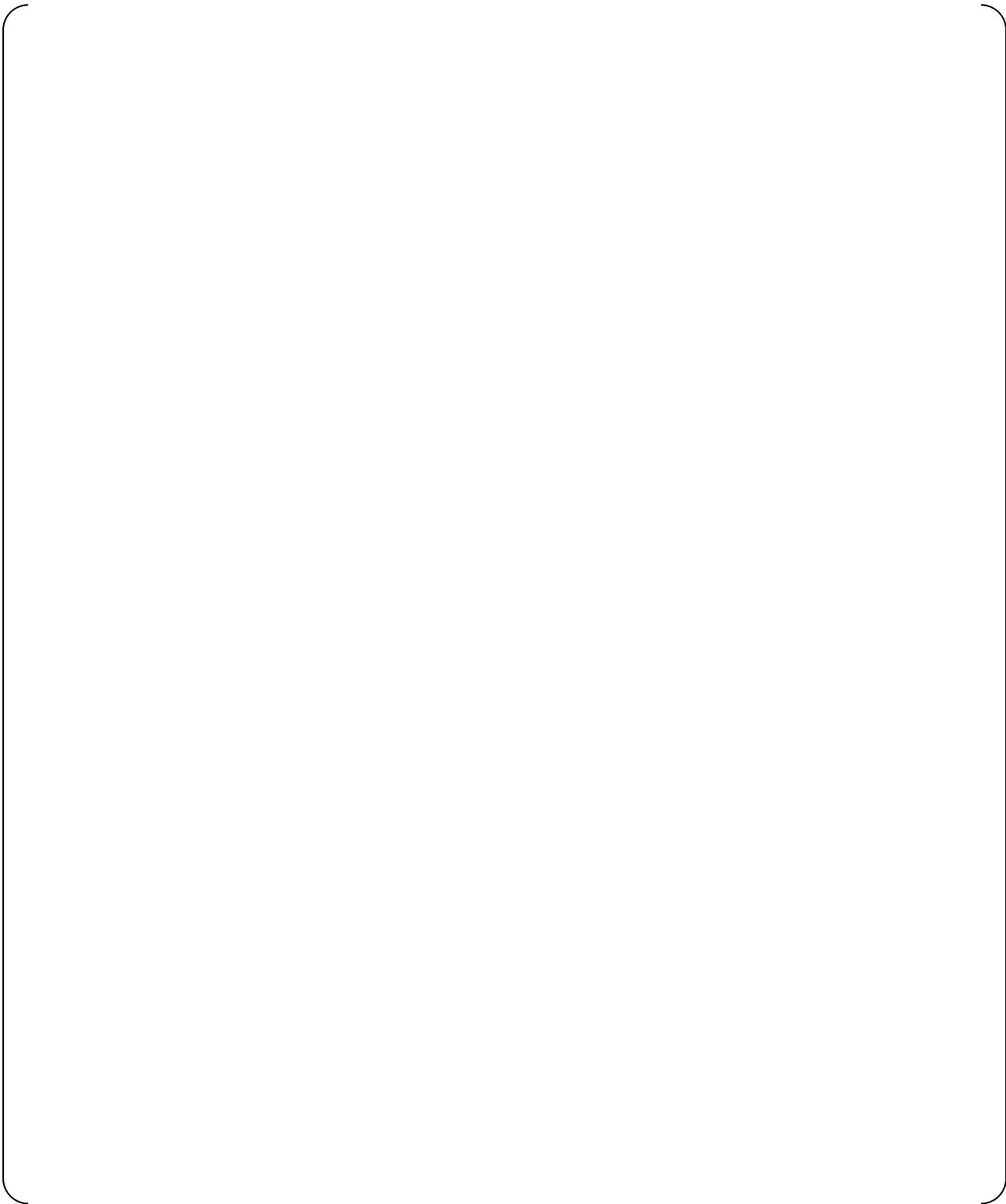
**Figure I-1(b) Flow Structure in Vortex Chamber and Outlet Nozzle**



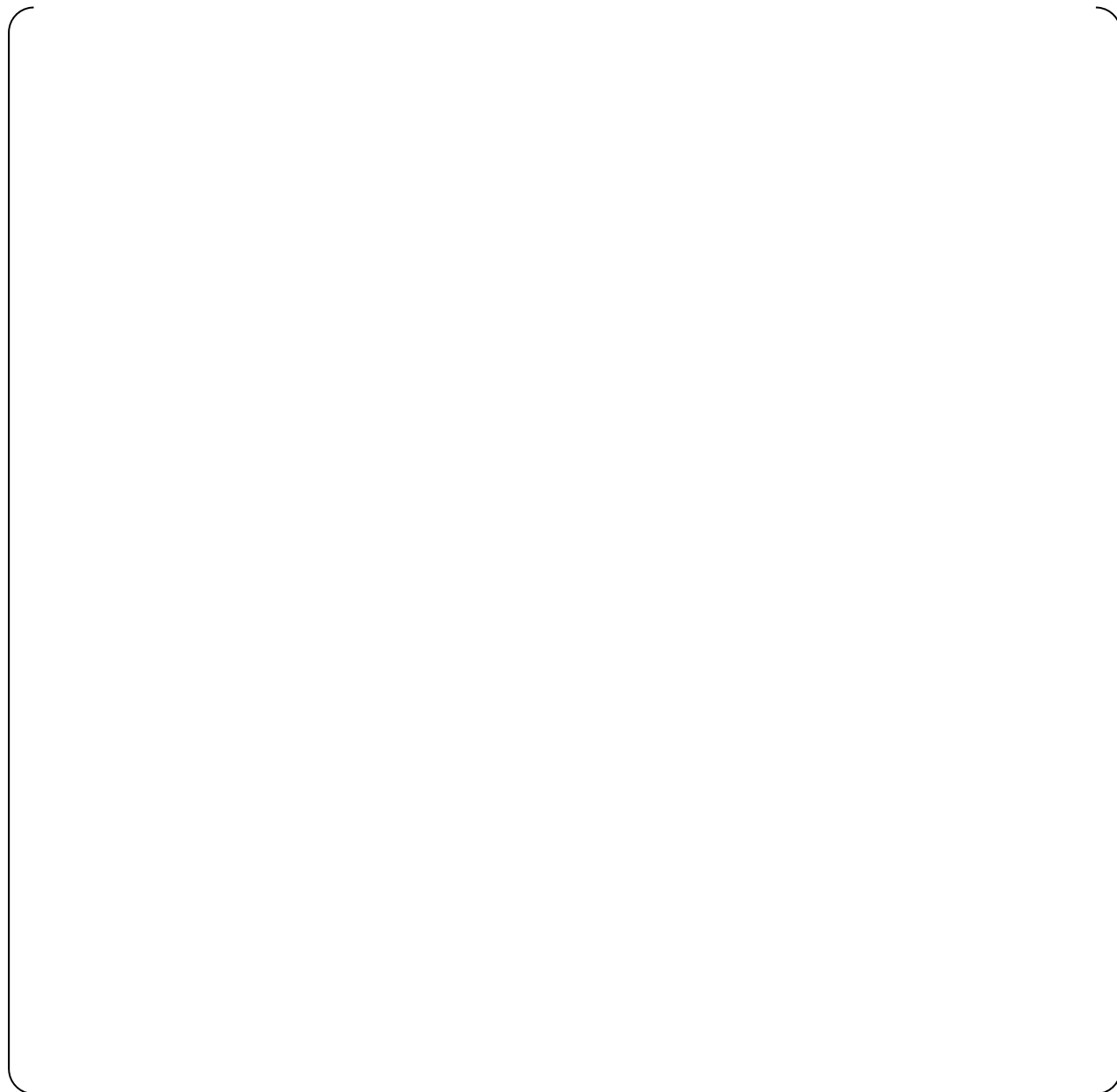
Figure I-1(c) Critical Pressure of Cavitation and Void Fraction in vortex Chamber and Outlet Nozzle



**Figure I-2 Velocity Distributions and Cavitation Pressure Margin at Throat**



**Table I-2 Calculation Results (1/2 Scale)****Table I-3 Calculation Results (1/1 Scale)**



## Appendix- J

### Details of Comparison Error for Large Flow

Figure J-1 shows comparison error between test data and CFD results for large flow. Almost all CFD results are within the range of instrument uncertainty of test data. Therefore, model tuning is not necessary for the large flow evaluation.

In Figure J-1, one point of the seven points is beyond the  $2\sigma$  limits of the test result. The probability that one point in seven points is beyond the limits of  $2\sigma$  of test result can be calculated by the following expressions.

The probability that the CFD result is within the limits of  $2\sigma$  of test result : [                      ]

The probability that the CFD result is beyond the limits of  $2\sigma$  of test result : [            ]

The probability that one point in seven points is beyond the limits of  $2\sigma$  of test results

[ ]

[ ]

The probability that one point in seven points is beyond the limits of  $2\sigma$  is about [     ].  
The conclusion is that, due to the limited number of sample points, this outlier is determined not to be statistically significant.



**Figure J-1 Overlapping between Test Results and  
Calculation Results for Flow Rate Coefficient  
(Large Flow Condition)**



## Appendix- K

**Asymptotic Behavior of Solution Results**

This appendix discusses the asymptotic behavior of the solution results and proposes a quantitative evaluation methodology for grid convergence of the 'normal mesh' and 'fine mesh', and illustrates asymptotic behavior using this methodology.

**(1) Basic Idea and Results**

In ASME V&V20 Section 2-3.3.3, the test criteria of the Grid convergence or asymptotic behavior for "Code Verification" is described and provides a quantitative examination methodology based on the theoretical expectation that the discretization error (i.e. the difference between the discrete solution and the exact (continuum) solution) should be proportional to the  $h^p$ , where  $h$  is a representative grid size and  $p$  is a observed order of numerical convergence. Basically this methodology cannot be used directly for "Solution Verification" because the exact solutions are not known for most practical problems.

Roache (in papers separate from ASME V&V 20) proposes the use of error relative to the extrapolated solution for practical cases where the exact solution is not known. In this case, the additional grid-dependency of the coarser grid should be addressed. That is:

$$\begin{aligned} E_1 &= (f_1 - f_{ex}), & E_2 &= (f_2 - f_{ex}) \\ r_{12} &= h_2/h_1, & r_{23} &= h_3/h_2 \\ C_1 &= (f_1 - f_{ex})/h_1^p, & C_2 &= (f_2 - f_{ex})/h_2^p \end{aligned}$$

Which simplifies to:

$$C(\text{ratio}) = C_1/C_2 = E_1 * r_{12}^p / E_2 \quad \text{Eq. K1-1}$$

or using relative errors,  $E_{12}$ ,  $E_{23}$ .

$$= \{ f_1 * E_{12} / (r_{12}^p - 1) * r_{12}^p \} / \{ f_2 * E_{23} / (r_{23}^p - 1) \} \quad \text{Eq. K1-2}$$

$$\text{Where, } E_{12} = (f_1 - f_2)/f_1, \quad E_{23} = (f_2 - f_3)/f_2$$

(Or, per Roache, Eq. 5.10.5.2, p. 130:  $GCI_{23} = r^p \times GCI_{12}$  (Ref.20))

If  $r_{12}$  and  $r_{23}$  are equal, then Equation K1-2 can be simplified as follows:

$$\begin{aligned} C(\text{ratio})_{r=\text{const.}} &= (f_1 * E_{12} * r_{12}^p) / (f_2 * E_{23}) \\ &= (f_1 - f_2) * r_{12}^p / (f_2 - f_3) \end{aligned} \quad \text{Eq. K1-3}$$

Using Equation K1-3, achievement of the asymptotic region can be demonstrated with information from three grid solutions, but only when "r = const."

To consider the influence of the difference between  $r_{12}$  and  $r_{23}$  in the cases where "r" is not constant, Equation K1-1 can be re-written as follows:

$$C(\text{ratio}) = (E_1 * r_{12}^p) / E_2$$

$$\begin{aligned}
&= \{ (f_1 - f_2) / (r_{12}^p - 1) * r_{12}^p \} / \{ (f_2 - f_3) / (r_{23}^p - 1) \} \\
&= \{ (f_1 - f_2) / (f_2 - f_3) * r_{12}^p \} / \{ (r_{12}^p - 1) / (r_{23}^p - 1) \} \\
&= C(\text{ratio})_{,r=\text{const.}} / Fc
\end{aligned}$$

Eq. K1-4

In this form,  $Fc$  can be recognized as the correction factor which corrects  $C(\text{ratio})_{,r=\text{const.}}$  to consider the influence of the difference between  $r_{12}$  and  $r_{23}$ .

$$Fc = (r_{12}^p - 1) / (r_{23}^p - 1) \quad \text{Eq. K1-5}$$

If it is assumed that all three solutions are in the asymptotic region (i.e.  $C(\text{ratio})=1$ ), then  $C(\text{ratio})_{,r=\text{const.}}$  becomes equal to “ $Fc$ ” and depends on  $r_{12}$  and  $r_{23}$ . That is, if all three solutions are within the asymptotic region but with different refinement ratios (i.e.  $r_{12}$  not equal to  $r_{23}$ ), then the criteria for the asymptotic region should be that the corrected  $C(\text{ratio})_{,r=\text{const.}}$  value is equal to  $Fc$  rather than unity.

Furthermore,  $Fc$  will vary depending on  $r_{12}$  and  $r_{23}$ . This relationship can be seen from the plot of  $C(\text{ratio})_{,r=\text{const.}}$  vs.  $R(\text{ratio}) (= r_{12}/r_{23})$  shown in Figure K1-1. Note that if  $R(\text{ratio})=1$ , then  $C(\text{ratio})_{,r=\text{const.}}$  would always give unity.

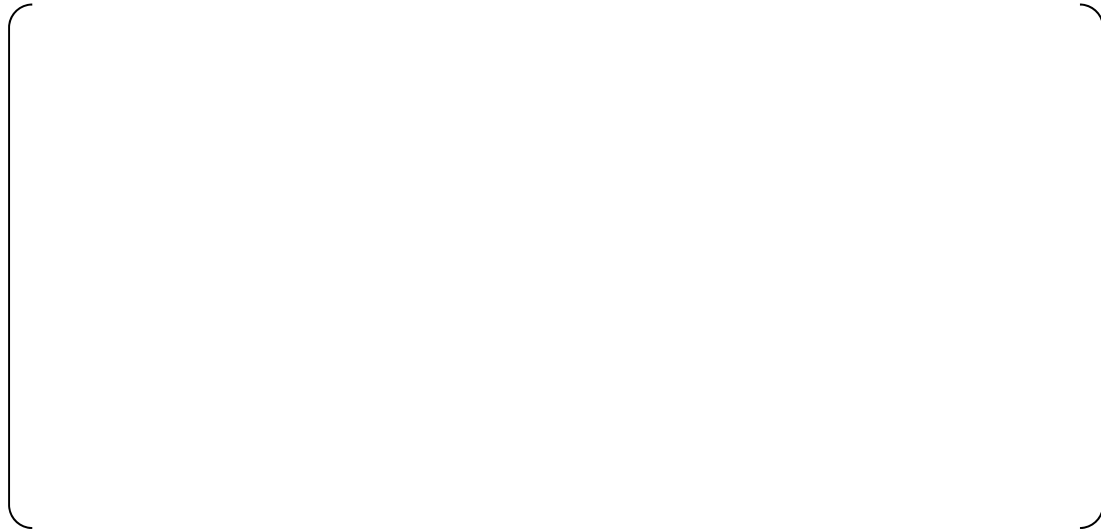


**Figure K1-1  $C(\text{ratio})_{,r=\text{const.}}$  vs.  $R(\text{ratio})$**

Here, the conditions of constraint are as follows (per the RAI 94a calculation):

$$r_{12} : 1.20 < r_{12} < 1.55$$

$$r_{23} : 1.07 < r_{23} < 1.60$$

$p$ -value is assumed 1.5 (expected value).

Using Equation K1-5, MHI calculated a more accurate  $C(\text{ratio})$  of the form “ $C(\text{ratio}) = C(\text{ratio})_{,r=\text{const.}, \text{calculated}} / C(\text{ratio})_{,r=\text{const.}, \text{expected}}$ ”. This compares the observed convergence ( $C(\text{ratio})_{,r=\text{const.}, \text{calculated}}$ ) to the corrected value ( $C(\text{ratio})_{,r=\text{const.}, \text{expected}}$ ) which would be expected for variable grid refinement with three “completely asymptotic” solutions. The derivation of this formulation is shown in the latter half of this appendix.

The results are shown in Table K1-1 and Figure K1-2. Each case shows that the C(ratio) is approximately equal to unity with  $p_{\text{assumed}} = 1.5$ . Therefore, the current solutions are within or close to the “completely asymptotic” region.

**Table K1-1 Corrected C(ratio) (  $p_{\text{assumed}} = 1.5$  )**

**Figure K1-2 Calculation Results for C(ratio)<sub>r=const.</sub> vs. R(ratio)**

(2) Calculations of C(ratio)

Abbreviations:

p = order of accuracy  
 $\phi_{\text{fine}}, \phi_{\text{medium}}, \phi_{\text{coarse}}$  = flow coefficient (Cv) for mesh (fine -1, medium -2, coarse -3)  
 $N_{\text{fine}}, N_{\text{medium}}, N_{\text{coarse}}$  = number of elements in mesh (fine -1, medium -2, coarse -3)

Equations

$$E_{12} = (\phi_{\text{fine}} - \phi_{\text{medium}}) / \phi_{\text{fine}}, \quad E_{23} = (\phi_{\text{medium}} - \phi_{\text{coarse}}) / \phi_{\text{medium}}$$
$$h = (\text{volume} / N)^{(1/3)} = \text{grid size}$$
$$r_{12} = h_{\text{medium}} / h_{\text{fine}}, \quad r_{23} = h_{\text{coarse}} / h_{\text{medium}}$$
$$C(\text{ratio}) = \{ f_1 * E_{12} / (r_{12}^p - 1) * r_{12}^p \} / \{ f_2 * E_{23} / (r_{23}^p - 1) \}$$

Table K2-1 The Solution Value and Relative Errors

Table K2-2 Calculations of C(ratio)

In order to provide a conservative evaluation, lower p-values in Table A5-1 in Appendix-A are selected.

### (3) Derivation of the Corrected C(ratio) Equation

If  $r_{12}$  and  $r_{23}$  are coincident with each other, then Equation K1-2 in body text can be simplified as follows:

$$\begin{aligned} C(\text{ratio})_{,r=\text{const.}} &= (f_1 * E_{12} * r_{12}^p) / (f_2 * E_{23}) \\ &= (f_1 - f_2) * r_{12}^p / (f_2 - f_3) \end{aligned} \quad \text{Eq. K3-1}$$

Using this formulation, achievement of the asymptotic region can be demonstrated with information from three grid solutions, but only when “ $r = \text{const.}$ ”

To consider the influence of the difference between  $r_{12}$  and  $r_{23}$  in the cases where  $r$  is not constant, Equation K3-1 can be re-written as follows:

$$\begin{aligned} C(\text{ratio}) &= (E_1 * r_{12}^p) / E_2 \\ &= \{(f_1 - f_2) / (r_{12}^p - 1) * r_{12}^p\} / \{(f_2 - f_3) / (r_{23}^p - 1)\} \\ &= \{(f_1 - f_2) / (f_2 - f_3) * r_{12}^p\} / \{(r_{12}^p - 1) / (r_{23}^p - 1)\} \\ &= C(\text{ratio})_{,r=\text{const.}} / F_c \end{aligned} \quad \text{Eq. K3-2}$$

In this form,  $F_c$  is the correction factor which corrects  $C(\text{ratio})_{,r=\text{const.}}$  to consider the influence of the difference between  $r_{12}$  and  $r_{23}$ .

$$F_c = (r_{12}^p - 1) / (r_{23}^p - 1) \quad \text{Eq. K3-3}$$

If it is assumed that all three solutions are in the asymptotic region (i.e.  $C(\text{ratio})=1$ ), then  $C(\text{ratio})_{,r=\text{const.}}$  becomes equal to “ $F_c$ ” and depends on  $r_{12}$  and  $r_{23}$ . This relationship can be seen from the plot of “ $C(\text{ratio})_{,r=\text{const.}}$  vs.  $R(\text{ratio}) (= r_{12}/r_{23})$ ” shown in Figure K3-1. Note that, if  $R(\text{ratio})=1$ , then  $C(\text{ratio})_{,r=\text{const.}}$  is always “1”.



**Figure K3-1  $C(\text{ratio})_{,r=\text{const}}$  vs.  $R(\text{ratio})$**

The conditions of constraint are as follows:

$$\begin{aligned} r_{12} : & \quad 1.20 < r_{12} < 1.55 \\ r_{23} : & \quad 1.07 < r_{23} < 1.60 \\ \text{p-value is assumed } & 1.5 \text{ (expected value)} \end{aligned}$$

When  $r_{12}$  and  $r_{23}$  are identified, one can estimate the expected  $C(\text{ratio})_{r=\text{const.}}$  with assumed p-value by Equation K3-3.

$$C(\text{ratio})_{r=\text{const.}, \text{ expected}} = (r_{12}^{p_{\text{assumed}}} - 1) / (r_{23}^{p_{\text{assumed}}} - 1) \quad \text{Eq. K3-4}$$

On the other hand,  $C(\text{ratio})_{r=\text{const.}}$  can be calculated from the known information from three solutions, i.e.  $\{f_1, f_2, f_3, r_{12}, p_{\text{observed}}\}$ , by Equation K3-1.

$$C(\text{ratio})_{r=\text{const.}, \text{ calculated}} = (f_1 - f_2) * r_{12}^{p_{\text{observed}}} / (f_2 - f_3) \quad \text{Eq. K3-5}$$

Now  $C(\text{ratio})$  can be evaluated by comparing “calculated” and “expected” values as follows:

$$\begin{aligned} C(\text{ratio}) &= C(\text{ratio})_{r=\text{const.}, \text{ calculated}} / C(\text{ratio})_{r=\text{const.}, \text{ expected}} \\ &= C(\text{ratio})_{r=\text{const.}, \text{ calculated}} / Fc_{\text{ expected}} \\ &= \{(f_1 - f_2) * r_{12}^{p_{\text{observed}}} / (f_2 - f_3)\} / \{(r_{12}^{p_{\text{assumed}}} - 1) / (r_{23}^{p_{\text{assumed}}} - 1)\} \end{aligned} \quad \text{Eq. K3-6}$$

The results are shown in Table K3-1 and Figure K3-2. Here,  $p_{\text{assumed}} = 1.5$  is used. Each case shows that  $C(\text{ratio})$  is approximately equal to unity, supporting the determination that the current solutions are within or at least close to the asymptotic region.

Results with different assumed p-values are shown in the remaining tables and figures (Tables K3-2 and K3-3 and Figures K3-3 and K3-4) for reference.

**Table K3-1 Corrected  $C(\text{ratio})$  (  $p_{\text{assumed}} = 1.5$  )**

Note: Due to the oscillatory grid convergence, CASE2 cannot be properly evaluated by this methodology. See Tables K2-1 and K2-2.



**Figure K3-2 Calculation Results for  $C(\text{ratio})_{r=\text{const.}}$  vs.  $R(\text{ratio})$  ( $p_{\text{assumed}} = 1.5$ )**

**Table K3-2 Corrected C(ratio) ( p<sub>assumed</sub> = 1.0 )**

**Figure K3-3 Calculation Results for C(ratio)<sub>r=const.</sub> vs. R(ratio) ( p<sub>assumed</sub> = 1.0 )**

**Table K3-3 Corrected C(ratio) ( p<sub>assumed</sub> = 2.58 )**

Table K3-3 Corrected C(ratio) (  $p_{\text{assumed}} = 2.58$  )

**Figure K3-4 Calculation Results for C(ratio)<sub>r=const.</sub> vs. R(ratio)( p<sub>assumed</sub> = 2.58 )**

Note: Due to the oscillatory grid convergence, CASE2 cannot be properly evaluated by this methodology. See Tables K2-1 and K2-2.



**Appendix- L****More Conservative CFD-evaluated Scale Effect**

For further comparison, an evaluation using bounding GCI values is calculated where the most conservative values from ASME V&V 20 are employed (i.e. p-value of [ ] and [ ], without a consideration of grid convergence characteristics). The results of this calculation are shown in the Table L-1.

Furthermore, more conservative scaling effects are estimated based on the bounding GCIs in Table L-1, which were calculated using conservative values at each individual calculation step, and ASME V&V 20 Section 2-4.1 Equation (2-4-14) (Ref.8).

The mesh error,  $u_{\text{mesh}}$  is defined by Equation 3.5.3-5 in the body text, where the error distribution of the GCI is assumed to be of a Gaussian distribution. In this case, a factor of 1.96 is employed to convert GCI into one standard deviation for estimating the total numerical uncertainty (from both scales) at each point on the characteristic equation.

Equation 3.5.3-5 is:

$$\left[ \frac{1.96 \cdot GCI_{1/1,i}}{GCI_{1/2,i}} \right] \quad \text{Eq.3.5.3-5}$$

According to ASME V&V 20 Section 2-4.1 Equation (2-4-1), a factor of 1.15 can be used to obtain a more conservative value for the corresponding one standard deviation. Using this conservative methodology, Equation 3.5.3-5 would be re-written as follows.

$$\left[ \frac{1.15 \cdot 1.96 \cdot GCI_{1/1,i}}{GCI_{1/2,i}} \right]$$

And the conservative values of  $GCI_{1/1,i}$  and  $GCI_{1/2,i}$  used to calculate  $u_{\text{mesh}}$  are listed as  $GCI_{\text{fine}}^{21}$  in Table L-1.

The results are shown in Table L-2 and L-3.

**Table L-1 Bounding GCIs for Further Comparison  
( $p=1$  and  $Fs=3.0$ )**

**(a) Calculation Procedure of GCI for 1/1 Scale Model CFD  
( $\phi$  = Flow Rate Coefficient  $C_v$ )**

**(b) Calculation Procedure of GCI for 1/2 Scale Model CFD  
( $\phi$  = Flow Rate Coefficient  $C_v$ )**

**Table L-2 Uncertainties using Bounding GCIs (Large Flow)**

**Table L-3 Uncertainties using Bounding GCIs (Small Flow)**

**Appendix- M****Mesh Refinement Ratio for Each Different Direction**

This appendix provides the detailed grid refinement data for all CFD cases used to evaluate the GCI. The grid refinement scheme is explained in Appendix-A.

**Table M-1 (a) Mesh Refinement Ratio for Each Different Direction  
(Large Flow, CASE03-005sec, 1/1 Scale ACC)**

Flow condition : Large Flow, CASE03-005sec

Scale : 1/1

**Table M-1 (b) Mesh Refinement Ratio for Each Different Direction  
(Large Flow, CASE03-005sec, 1/2 Scale ACC)**

Flow condition : Large Flow, CASE03-005sec

Scale : 1/2

**Table M-2 (a) Mesh Refinement Ratio for Each Different Direction  
(Large Flow, CASE03-034sec, 1/1 Scale ACC)**

Flow condition : Large Flow, CASE03-034sec

Scale : 1/1

**Table M-2 (b) Mesh Refinement Ratio for Each Different Direction  
(Large Flow, CASE03-034sec, 1/2 Scale ACC)**

Flow condition : Large Flow, CASE03-034sec

Scale : 1/2



**Table M-3 (a) Mesh Refinement Ratio for Each Different Direction  
(Large Flow, CASE06-005sec, 1/1 Scale ACC)**

Flow condition : Large Flow, CASE06-005sec  
Scale : 1/1

**Table M-3 (b) Mesh Refinement Ratio for Each Different Direction  
(Large Flow, CASE06-005sec, 1/2 Scale ACC)**

Flow condition : Large Flow, CASE06-005sec  
Scale : 1/2

**Table M-4 (a) Mesh Refinement Ratio for Each Different Direction  
(Large Flow, CASE06-050sec, 1/1 Scale ACC)**

Flow condition : Large Flow, CASE06-050sec  
Scale : 1/1

**Table M-4 (b) Mesh Refinement Ratio for Each Different Direction  
(Large Flow, CASE06-050sec, 1/2 Scale ACC)**

Flow condition : Large Flow, CASE06-050sec

Scale : 1/2

**Table M-5 (a) Mesh Refinement Ratio for Each Different Direction  
(Small Flow, CASE03-043sec, 1/1 Scale ACC)**

Flow condition : Small Flow, CASE03-043sec  
Scale : 1/1

**Table M-5 (b) Mesh Refinement Ratio for Each Different Direction  
(Small Flow, CASE03-043sec, 1/2 Scale ACC)**

Flow condition : Small Flow, CASE03-043sec  
Scale : 1/2

**Table M-6 (a) Mesh Refinement Ratio for Each Different Direction  
(Small Flow, CASE03-125sec, 1/1 Scale ACC)**

Flow condition : Small Flow, CASE03-125sec

Scale : 1/1

**Table M-6 (b) Mesh Refinement Ratio for Each Different Direction  
(Small Flow, CASE03-125sec, 1/2 Scale ACC)**

Flow condition : Small Flow, CASE03-125sec

Scale : 1/2



**Table M-7 (a) Mesh Refinement Ratio for Each Different Direction  
(Small Flow, CASE06-082sec, 1/1 Scale ACC)**

Flow condition : Small Flow, CASE06-082sec

Scale : 1/1

**Table M-7 (b) Mesh Refinement Ratio for Each Different Direction  
(Small Flow, CASE06-082sec, 1/2 Scale ACC)**

Flow condition : Small Flow, CASE06-082sec

Scale : 1/2

**Table M-8 (a) Mesh Refinement Ratio for Each Different Direction  
(Small Flow, CASE06-290sec, 1/1 Scale ACC)**

Flow condition : Small Flow, CASE06-290sec  
Scale : 1/1

**Table M-8 (b) Mesh Refinement Ratio for Each Different Direction  
(Small Flow, CASE06-290sec, 1/2 Scale ACC)**

Flow condition : Small Flow, CASE06-290sec

Scale : 1/2